

Development and implementation of adaptive mesh refinement methods for numerical simulations of metal forming and machining

Von der Fakultät Maschinenbau
der Technischen Universität Dortmund
zur Erlangung des Grades eines
Doktor-Ingenieurs
(Dr.-Ing.)
genehmigte Dissertation

von

Xin Gu

Dortmund 2008

Contents

Summary	iii
1 Recovery based error estimation and adaptivity	1
1.1 Introduction	1
1.2 Superconvergent patch recovery methods	4
1.3 Recovery method based on local extrapolation	6
1.4 Error estimation	11
1.5 Numerical tests	11
1.6 <i>A posteriori</i> error estimation	30
1.7 Optimization of mesh size map	31
1.8 Adaptivity and numerical examples	33
1.9 Conclusions	46
2 Automatic mesh refinement and coarsening	47
2.1 Introduction	47
2.2 Unstructured mesh generation	48
2.3 Hierarchical mesh generation	51
2.4 Examples	53
3 Optimization based mesh smoothing for planar meshes	57
3.1 Introduction	57
3.2 Mesh quality measures and objective function	59
3.3 Modified objective functions	68
3.4 Alternative objective function	70
3.5 Combined Laplacian and optimization based smoothing for non-conforming mesh	70
3.6 Mesh optimization algorithm	71
3.7 Examples	73
3.8 Conclusions	81
4 Adaptive remeshing for metal forming simulations	83
4.1 Introduction	83
4.2 Error estimation	85
4.3 <i>A posteriori</i> error estimation	87

4.4	Optimization of mesh size map	88
4.5	Mapping algorithm	90
4.6	Metal forming simulation	91
4.7	Adaptive remeshing for large deformation problem with damage	119
4.8	Conclusions	121
	References	137
	Acknowledgements	139
	Curriculum Vitae	141

Summary

In metal forming or cutting simulations, inelastic processes in the work piece, as well as complex building component geometries or production process boundary conditions, may result in extreme deformation of the mesh and the development of large gradients in the stress or other fields. In the context of standard finite element formulations, this often leads to a loss of robustness and efficiency in the numerical simulation, and even to its failure. One method to improve the efficiency and robustness of the numerical solution under such circumstances is to automatically remesh the deformed workpiece while required. In addition, error control is required in order to achieve optimal graded meshes and maintain discretization errors within prescribed limits. The current work is focused on the issues in adaptive remeshing, which consists of error estimation, mesh refinement and coarsening, mesh optimization and application to metal forming simulations.

The accuracy of a finite element solution is an important issue in finite element simulations. The main study in Chapter 1 is concentrated on the discretization error which is due to the finite element approximation of the solution. Based on the pioneer work on recovery based error estimation (Zienkiewicz and Zhu, 1987, 1992a,b), several modified versions of the SPR recovery technique are proposed. Subsequently, a local extrapolation technique (BF) is developed based on the best-fit point. The recovered derivatives are obtained at nodes via extrapolation from the sampling points and subsequent averaging. Afterwards, the discretization error is assessed by comparing the finite element solution and the recovered solution. Numerical tests show that the BF method provides the most accurate error estimation in these methods.

In an adaptive simulation, remeshing techniques are required to re-discretize computational domain while the old spatial discretization is not suitable for further simulation. Unstructured meshing techniques have been shown to be effective and robust in generating a new mesh to replace the old distorted mesh. However, it could have difficulties in generating local dense mesh or yield distorted elements in graded mesh due to mesh transition. In contrast, hanging-node-based hierarchical mesh refinement can easily achieve desired local dense mesh though it doesn't help the improvement of mesh quality. Therefore, in Chapter 2, we develop a combined unstructured and hanging-node-based remeshing strategy by exploiting the advantages of unstructured meshing technique and hanging-node-based mesh refinement technique. Mesh refinement and coarsening on boundary is realized by using a boundary node placement algorithm.

It is well known that a severely distorted mesh reduces the solution accuracy (Oddy et al., 1988). Mesh smoothing techniques such as Laplacian smoothing have been shown to be effective in improving geometrical mesh quality. However, when a badly shaped mesh contains invalid elements, most existing methods are not able to optimize such a mesh. In Chapter 3, an optimization based mesh smoothing scheme based on the mesh quality measure, derived from the condition number of the Jacobian matrix, is presented to optimize both invalid and

valid meshes. The corresponding optimization problem is solved with the help of the steepest descent method. The method can be used together with any type of mesh refinement approach, e.g., hanging nodes. Numerical examples using the current approach demonstrate its robustness and effectiveness.

In Chapter 4, each of the parameters including error estimator, mapping algorithm, remeshing technique and element type in adaptive metal forming simulations are discussed and evaluated. The simulations of four types of manufacturing processes such as extrusion, cutting, forging and rolling have been carried out to validate the proposed adaptive remeshing procedure. In the applications, bilinear quadrilateral elements seem to be more efficient and robust than linear triangular elements. In the adaptive simulation of metal cutting, numerical comparison shows that the mapping algorithm based on local extrapolation technique (BF) transfers state variables with the least numerical diffusion. Mesh coarsening included in the adaptive remeshing procedure is shown to be able to reduce computational costs without decreasing the solution accuracy. For large deformation problems with damage, the adaptive remeshing, including a damaged element elimination procedure, is shown to be efficient.

Zusammenfassung

In Umformungs- und Schneidsimulationen von Metall, können inelastische Prozesse im Werkstück sowie komplexe Bauteilgeometrien oder Produktionsprozessgrenzbedingungen in extremer Netzverformung und der Ausbildung großer Gradienten in Spannungs- und anderen Feldern resultieren. Im Zusammenhang mit Standard-Finite-Elemente-Formeln führt dies oft zu einem Verlust an Stabilität und Effizienz der numerischen Simulation oder sogar zu deren Versagen. Eine Methode zur Verbesserung der Effizienz und Stabilität der numerischen Lösung unter solchen Bedingungen ist es, das verformte Werkstück bei Bedarf automatisch neu zu vernetzen. Zusätzlich ist eine Fehlerkontrolle notwendig, um optimal skalierte Netze sicherzustellen und die Diskretisierungsfehler im vorgeschriebenen Rahmen zu halten. Der Schwerpunkt dieser Arbeit liegt in der Betrachtung der Belange der adaptiven Wiedervernetzung, die aus Fehleranalyse, Netzverfeinerung, Netzvergrößerung, Netzoptimierung und der Anwendung auf Metallumformungssimulationen.

Die Genauigkeit einer Finite-Elemente-Lösung ist ein wichtiger Punkt von Finite-Elemente-Simulationen. Der Schwerpunkt in Kapitel 1 liegt auf der Betrachtung des aus der Finite-Elemente-Approximation resultierenden Diskretisierungsfehlers des Lösungsansatzes. Basierend auf der Grundlagenarbeit über recovery-basierte Fehlerabschätzung (Zienkiewicz and Zhu, 1987, 1992a,b), werden einige modifizierte Versionen des SPR recovery-Verfahrens vorgeschlagen. Schlussfolgernd wird eine lokale Extrapolationstechnik (BF) basierend auf einem Idealpunkt entwickelt. Die zurückgewonnenen Ableitungen werden in Knotenpunkten durch Extrapolation aus den Testpunkten und darauf folgender Mittelung ermittelt. Hiernach wird der Diskretisierungsfehler bewertet, indem die Finite-Elemente-Lösung mit der recovery-Lösung verglichen wird. Numerische Tests zeigen, dass die BF Methode die genaueste Fehlerabschätzung dieser Methoden liefert.

In adaptiven Simulationen sollen Neuvernetzungstechniken den rechnerbasierten Bereich neu diskretisieren, da die alte spatial-Diskretisierung für weitere Simulationen nicht geeignet ist. Unstrukturierte Vernetzungstechniken haben sich als effektiv und stabil dabei erwiesen, ein neues Netz anstelle des alten verformten Netzes zu generieren. Allerdings könnte es Schwierigkeiten beim Generieren von lokal dichten Netzen oder schubverzerrten Elementen in geordneten Netzen aufgrund von Netzübergängen geben. Im Gegensatz dazu kann die hanging-node-basierte hierarchische Netzverfeinerung auf einfache Weise zum gewünschten dichten Netz führen, allerdings führt es nicht zur Verbesserung der Netzqualität. Deswegen entwickeln wir in Kapitel 2 eine kombinierte, aus unstrukturierter und hanging-node-basierter Neuvernetzung zusammengesetzte, Strategie indem wir die Vorteile des unstrukturierten Vernetzungsverfahrens und des hanging-node-basierten Netzverfeinerungsverfahrens ausnutzen. Netzverfeinerung und -vergrößerung in Grenzbereichen wird durch einen Grenzpunktsetalgorithmus realisiert.

Es ist bekannt, dass schwer deformierte Netze die Lösungsgenauigkeit reduzieren (Oddy et al., 1988). Netzglättungsverfahren wie die Laplace-Glättung haben sich als effektiv dabei

erwiesen, die geometrische Netzqualität zu verbessern. Enthält ein schlecht geformtes Netz ungültige Elemente, so sind die meisten existierenden Methoden nicht fähig, so ein Netz zu optimieren. In Kapitel 3 wird ein optimierungsbasiertes Netzglättungsmodell, basierend auf dem Netzqualitätsmaß, welches von der Konditionszahl der Jacobimatrix abgeleitet ist, präsentiert, welches sowohl ungültige als auch gültige Netze optimiert. Das zusammenhängende Optimierungsproblem wird mit Hilfe der Sattelpunktsnäherung gelöst. Diese Methode kann zusammen mit jeder Ansatzart der Netzverfeinerung, z. B. den hanging-nodes, genutzt werden. Numerische Beispiele, die diese Herangehensweise nutzen, zeigen deren Stabilität und Effektivität.

In Kapitel 4 wird jeder der Bestandteile diskutiert und ausgewertet, einschließlich des Fehler-schätzers, des Vernetzungsalgorithmus, des Neuvernetzungsverfahrens und der Elementtypen in adaptiven Metallumformungssimulationen. Die Simulationen von vier Arten von Herstellungsprozessen, nämlich Strangpressen, Schneiden, Schmieden und Walzen wurden durchgeführt, um das vorgeschlagene adaptive Neuvernetzungsverfahren zu validieren. In den Anwendungen scheint das bilinear-quadratische Element effizienter und stabiler als das linear-dreieitige. In der adaptiven Schneidsimulation zeigt der numerische Vergleich, dass der auf dem lokalen Extrapolationsverfahren (BF) basierte Vernetzungsalgorithmus Zustandsvariablen mit der kleinsten numerischen Abweichung überträgt. Es wird gezeigt, dass die Netzvergrößerung, die in der adaptiven Neuvernetzungsmethode beinhaltet ist, in der Lage ist, Rechenaufwand zu reduzieren ohne die Ergebnisgenauigkeit zu senken. Für Probleme großer Verformung mit Schäden erweist sich die adaptive Neuvernetzung, unter Einbeziehung einer Prozedur zur Eliminierung geschädigter Elemente, als effizient.

Chapter 1

Recovery based error estimation and adaptivity

Abstract – The discretization error in a finite element solution is investigated in the current work. Several modified versions of the famous SPR recovery technique are proposed. Subsequently, a local extrapolation technique is investigated based on the best-fit point. The recovered derivatives are obtained at nodes via extrapolation from the sampling points and subsequent averaging. Numerical tests demonstrate that the resulting recovery method is more accurate than the original and the presented modified super-convergent patch recovery methods (SPR). Finally, a-posteriori error estimators for plasticity problems and adaptive strategies are introduced and demonstrated by numerical examples.

Keywords: error estimation, recovery method, best fit point, adaptivity.

1.1 Introduction

Nowadays, the finite element method has been widely used in engineering applications. In the context of the finite element method, a deformable body is discretized by a mesh which is defined by a finite number of nodes and elements. Physical phenomena, including material behavior, contact condition etc., are approximated with mathematical models. The solution is approximated and interpolated by the element shape functions. Thus, the accuracy of the finite element solution is highly dependent on the mesh size, the shape functions and the mathematical model such as the material model. Naturally, a question arises: How to assess the accuracy of a finite element solution?

Basically, there are two types of errors. Recently, the modelling error due to the use of various mathematical models of physical phenomena has been investigated by Oden et al. (2001). The main study in this chapter is focused on the discretization error which is due to the finite element approximation of the solution. For this purpose, two types of error estimators are available. A priori error estimators provide the information on the asymptotic behavior of the discretization error but it is not designed to give an actual error estimation for a given mesh (*e.g.*, Graetsch and Bathe, 2005; Hugger, 2001). In contrast, a posteriori error estimators assess the actual error of the solution, based on the finite element solution (*e.g.*, Verfürth, 1999). Thus, a posteriori error estimation has been widely used in mathematics and engineering. Here, the error in an element which is induced by the element itself is indicated as local error. In contrast, a so-called pollution error is due to the error in other neighboring elements. The pollution error was reported by Babuska et al. (1997a, 1994a, 1995) and further investigated by Huerta and Diez (2000); Mukherjee and Krishnamoorthy (1998a).

The first paper on error estimation was presented by Babuska and Rheinboldt (1978). Since then, a great deal of work on error estimation has been carried out by many researchers. In

general, they can be classified into two main categories: residual based error estimators and recovery based error estimators.

The residual based error estimation is computed by using the residuals of the finite element solution, which fail to satisfy the mathematical model, explicitly or implicitly. The explicit residual error is expressed directly with the residuals of the finite element solution (*e.g.*, Cecot, 2007a); on the other hand, the implicit residual error estimation is determined by solving local problems. The explicit residual error estimators have been shown to be inaccurate in estimating errors, and can only be used for guiding the adaptive analysis procedures (Babuska et al., 1994c). The implicit residual error estimators are more accurate, but take more computational cost. The requirement of solving local problems is even more complicated, when applied to nonlinear problems. The pioneer work on residual based error estimation was proposed by Babuska and Rheinboldt (1978), which estimates errors by considering local residuals of the finite element solution. On that basis, a number of residual based error estimators have been developed (*e.g.*, Ainsworth et al., 2007; Ainsworth and Oden, 1993, 1997; Dey et al., 2006; Estep et al., 2002; Hugger, 2001). For nonlinear plasticity problems, an implicit residual based error estimator using local patch sub-meshes was proposed by Diez et al. (1998); Huerta and Diez (2000); Huerta et al. (2002); Rodriguez-Ferran and Huerta (2000).

Compared to the residual based error estimation, the recovery based error estimation is the most popular technique, as it is easy to implement in an existing finite element code and dramatically robust. The basic idea of the type of error estimation is to compare the finite element solution and the recovered solution which is obtained by using recovery techniques in a post-processing procedure. The pioneer work on the recovery technique and error estimation was carried out by Zienkiewicz and Zhu (1987), which uses simple nodal averaging to improve the finite element solution. Subsequently, Zienkiewicz and Zhu (1992a,b,c) proposed the most famous Z^2 superconvergent patch recovery technique (SPR), which is being widely used until now.

The original SPR method is based on a least-squares fit of derivatives at the optimal sampling points (*e.g.*, Babuska et al., 1996; Barlow, 1976, 1989; Levine, 1985; Lin and Zhang, 2004; Mackinnon and Carey, 1989; Oh and Batra, 1999; Prathap, 1996) over a “node patch” (see Figure 4.1). Such a patch represents the union of the elements surrounding the assembly node. The continuous and more accurate stresses over the whole domain are obtained by first recovering nodal stresses and then interpolating these with standard shape functions. The technique shows a significant improvement of performance compared to other recovery techniques (*e.g.*, Hinton and Campbell, 1974; Oden and Brauchli, 1971; Oden and Reddy, 1973; Zienkiewicz and Zhu, 1987) and the recovered solution was demonstrated to be superconvergent or even ultraconvergent (*e.g.*, Babuska et al., 1997c; Li and Zhang, 1999; Wiberg, 1997; Wiberg and Abdulwahab, 1997; Zhang and Harold Dean Victory, 1996; Zhang and Zhu, 1998, 1995; Zhu and Zienkiewicz, 1997; Zienkiewicz and Taylor, 1997; Zienkiewicz and Zhu, 1995; Zienkiewicz et al., 1993). Babuska et al. (1994b,c) designed a robust “patch test” and proved the SPR method was better than the element-residual error estimator.

Although good, the SPR method has been extended and improved by many authors. Mukherjee and Krishnamoorthy (1998b); Wiberg et al. (1995) and Gu et al. (2004) proposed a weighted

patch scheme. Blacker and Belytschko (1994) introduced a conjoint interpolant which improves the accuracy of recovered solution compared to the standard nodal interpolation. Blacker and Belytschko (1994); Boroomand et al. (2004); Boroomand and Mossaiby (2005a,b); Boroomand and Zienkiewicz (1997a,b, 1999); Kvamsdal and Okstad (1998); Lee et al. (1997); Okstad et al. (1999); Park et al. (1999); Rodenas et al. (2006); Wiberg and Abdulwahab (1993); Wiberg et al. (1994); Zienkiewicz et al. (1999) incorporated the equilibrium and boundary condition with patch recovery. Li and Wiberg (1994); Mukherjee and Krishnamoorthy (1998b); Wiberg et al. (1995) proposed a different configuration of elements, which is called an “element patch” (see Figure 4.1) defined as the union of the elements surrounding an element under consideration. However, a drawback of the element patch is that the recovered stress field is discontinuous over the element boundaries. One part of the current work is to introduce a procedure to avoid a discontinuous recovered stress field by using additional nodes. Based on the least square method, some Hessian recovery techniques were developed and analyzed by Vallet et al.; Yazdani et al. (1997). Maisano et al. (2006); Wiberg and Li (1994) reported a recovery technique which fits a polynomial to the displacements at nodes instead of the gradients at sampling points. The type of error estimator was then further improved by using the patch with surrounding nodes (Naga and Zhang, 2004; Zhang and Naga, 2004, 2005), here, the idea is related to the meshless method. A recovery technique based on complementary energy was developed by Benedetti et al. (2006); Ubertaini (2004). Based on the SPR technique, Picasso (2003) introduced an anisotropic error estimator for anisotropic unstructured meshes.

In addition to the improvement of superconvergent patch recovery technique, recovery based error estimators have been widely applied to various problems: the plasticity problem (Araujo et al., 2000; Boroomand and Zienkiewicz, 1999; Cecot, 2007a; Khoei et al., 2007; Li and Bettess, 1997), axisymmetrical problem (Yazdani et al., 1998), acoustics problem (Bouliard et al., 1996; Dey et al., 2006), shell analysis (Li et al., 1997), shape optimization problem (Bugeda and Onate, 1993; Bugeda et al., 2007; Fuenmayor et al., 1997), eigenfrequency analysis (Hager and Wiberg, 1999), dynamics problem (Wiberg and Li, 1999), crack propagation problem (Khoei et al., 2008) and metal forming problem (Boussetta et al., 2006; Park and Yang, 2006).

While using the superconvergent patch recovery techniques, one needs to minimize objective functions by solving linear systems. However, the matrix in the linear system could be ill-conditioning or rank deficiency. In this case, additional procedures such as normalization of the coordinates (Wiberg and Abdulwahab, 1993), LU decomposition with partial pivoting (Labbe and Garon, 1995) and rotation of the coordinate system (Yue and Jr, 2006) have to be involved to overcome these problems, which lead to higher computation cost. However, from the engineering point of view, a good technique should be effective, robust and as simple as possible. Therefore, in the current work, we developed a best-fit point based extrapolation technique. The original idea was proposed by Levine (1985), who demonstrated that the average stress value is superconvergent at the midpoint of a common edge between neighboring elements in structured triangular meshes. Here, we investigate the position of such optimal sampling points in unstructured meshes using the best-fit approach (*e.g.*, Liew and Rajendran, 2002; Rajendran and Liew, 2003). On this basis, a recovery method based on the best-fit points is developed. In particular, the recovered derivatives are obtained at the nodes via extrapolation from the sampling best-fit points and subsequent averaging.

This chapter is organized as follows. In §1.2, we review the SPR method and propose our modifications. The position of the best-fit point in neighboring elements is then investigated and applied in our recovery method in §1.3. Next, we introduce the error estimation and effectivity index used in this work. In §1.5, numerical tests are given to compare the performance of these recovery methods discussed in this paper. In §1.6, we introduce the error estimators for plasticity problems and the adaptive strategy. The strategy for optimization of mesh size map is introduced in §1.7. Some numerical examples on adaptivity are given in §1.8. Finally, some conclusions are presented in §1.9.

1.2 Superconvergent patch recovery methods

The original SPR method (ZZ) was proposed by Zienkiewicz and Zhu (1992b). In this method, a node patch (see Figure 4.1) is defined for the original SPR method by the union of elements surrounding the node in question. Let σ^* represent any component of the recovered element

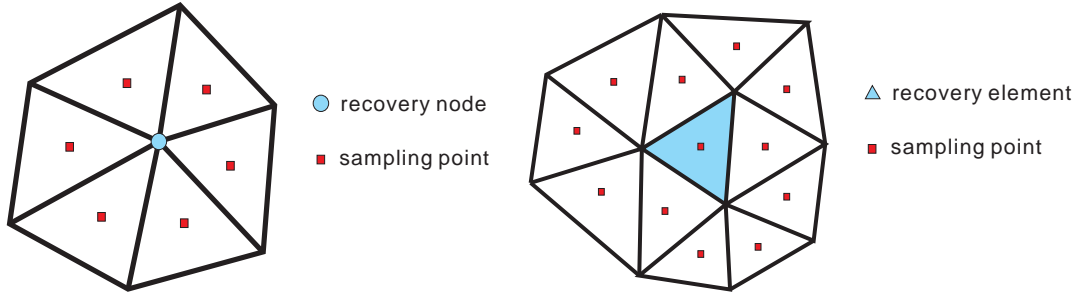


Figure 1.1: Different approaches to obtain a field of recovered values. The node patch recovery (left) provides a continuous field containing the recovered values inside the nodes, whereas the corresponding field, provided by the element patch recovery (right) is discontinuous across elemental boundaries (see text for further details).

stress field. This is related to the set $\mathbf{s}_m = (s_1, s_2, \dots)$ of corresponding nodal values at the mesh nodes via the usual ansatz

$$\sigma^* = \mathbf{h}_m \cdot \mathbf{s}_m^* \quad (1.1)$$

in terms of the array $\mathbf{h}_m^* = (h_1, h_2, \dots)$ of element shape functions. The set \mathbf{s}_m is obtained by assuming that σ^* is given by an order p polynomial expansion over a node patch, *i.e.*,

$$\sigma^* \equiv \sigma_p^* = \mathbf{p} \cdot \mathbf{a}, \quad (1.2)$$

where \mathbf{p} is an array consisting of the terms of an order p polynomial and \mathbf{a} is a set of unknown parameters. In the case of a three-node triangular element, for example, we have

$$\mathbf{p} = (1, x, y) \quad (1.3)$$

and

$$\mathbf{a} = (a_1, a_2, a_3). \quad (1.4)$$

Then

$$\sigma_p^* = a_1 + a_2x + a_3y \quad (1.5)$$

follows. The unknown parameters \mathbf{a} are determined by a least square fit to a set of sample points at which the stress component σ_h obtained from the finite-element solution is known to be superconvergent or at least highly accurate. The least-squares fit is based on minimizing the objective function

$$f(\mathbf{a}) = \sum_{i=1}^n |\sigma_h(x_i, y_i) - \sigma_p^*(x_i, y_i)|^2, \quad (1.6)$$

where n is the number of sampling points and $(x_1, y_1), (x_2, y_2), \dots$ are the coordinates of these points. Extremization of $f(\mathbf{a})$ yields the linear system

$$\mathbf{A}\mathbf{a} = \mathbf{b}, \quad (1.7)$$

with

$$\mathbf{A} = \sum_{i=1}^n \mathbf{p}(x_i, y_i) \otimes \mathbf{p}(x_i, y_i) \quad (1.8)$$

and

$$\mathbf{b} = \sum_{i=1}^n \sigma_h(x_i, y_i) \mathbf{p}(x_i, y_i). \quad (1.9)$$

Consider next the SPR method as based on the element patch and polynomial expansion. Wiberg et al. (1995) proposed an element patch (see Figure 4.1) defined by the union of the elements surrounding the element in question. On this basis, they investigated 2D problems by using a polynomial of order p . Since in this case there are at least seven elements in an interior element patch (see Figure 1.2), one can use a polynomial of order $p + 1$ for σ^* . In this case, we have

$$\mathbf{p} = (1, x, y, x^2, xy, y^2) \quad (1.10)$$

and

$$\mathbf{a} = (a_1, a_2, a_3, a_4, a_5, a_6), \quad (1.11)$$

yielding

$$\sigma^* \equiv \sigma_{p+1}^* = a_1 + a_2x + a_3y + a_4x^2 + a_5xy + a_6y^2. \quad (1.12)$$

Having seven values for σ_h in this case, one can determine the six components of \mathbf{a} .

In the SPR method based on an element patch and a polynomial of order $p + 1$, the recovered stress field is obtained directly by using the SPR solution, which is discontinuous over element boundaries. In order to provide a continuous field of order $p + 1$, we introduce additional nodes in the element and treat it from the post-processing point of view as a six-node triangular element (see Figure 1.3).

Since the average stress values in neighboring elements at the midpoints of their common edges are superconvergent, these midpoints represent a logical choice for the additional nodes. On this basis, the recovered stress field may be obtained by a simple averaging of the overlapping patch solutions for the mesh nodes. This yields the form

$$\sigma^* = \mathbf{h}_m \cdot \mathbf{s}_m^* + \mathbf{h}_p \cdot \mathbf{s}_p^* \quad (1.13)$$

for the final field over the entire domain via interpolation of the values at mesh nodes as in equation (4.1) and at additional nodes associated with the patch as based on the interpolation functions \mathbf{h}_p and interpolation values \mathbf{s}_p^* at the additional nodes.

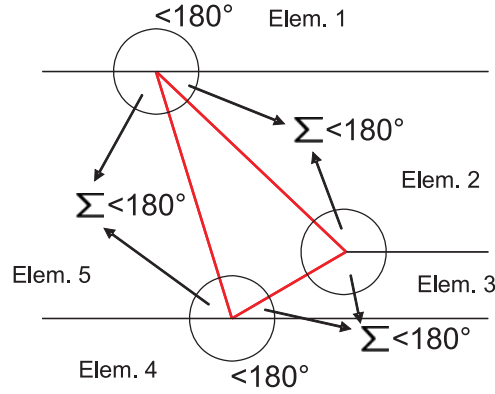


Figure 1.2: The sum of exterior angles of one triangular element is 900° and each interior angle must be less than 180° , therefore one interior triangle must have at least six surrounding. Five elements are only possible with one angle having 0° . Note the shape of the interior element being arbitrary.

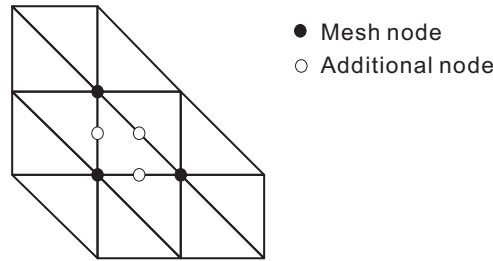


Figure 1.3: Element patch with additional nodes.

1.3 Recovery method based on local extrapolation

The average derivative at the midpoint of the common edge of neighboring elements was shown to be superconvergent by Levine (1985) and further investigated by Lakhany et al. (2000); Lakhany and Whiteman (1999). Motivated in this section by the extrapolation technique discussed by Zienkiewicz and Zhu (1992b), we discuss how to obtain the recovered derivatives over an element by interpolating and extrapolating the superconvergent values from the midpoints. With three points at hand, we can perform, at least, linear extrapolation. The typical element patch used for this is shown in Figure 1.4. Note that this differs from the element patch used in SPR method.

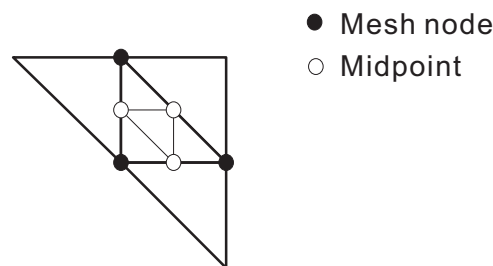


Figure 1.4: Element patch used for the midpoint method.

Using this patch, we can again, recover the values elementwise or nodewise. In the first method (MP), the recovered derivatives are obtained directly using interpolation and extrapolation. In this case, the recovery procedure consists of the following steps:

1. average the derivatives at the midpoint of common element edges,
2. interpolate and extrapolate these three values in the range of the element directly.

The drawback of this method is that the recovered solution is discontinuous on element boundaries. To deal with this, one can modify the recovery procedure as follows (named as MPN method):

1. average the derivatives at the midpoints of element edges,
2. extrapolate these three superconvergent values to the nodes,
3. calculate the average value of the overlapping recovered solutions at the nodes and 4) interpolate the solution field using these nodal values.

Alternately, in order to obtain a solution field of order $p + 1$, step 4) can be replaced by interpolating the solution field with the values at the nodes and the midpoints, which is denoted as MPAN method.

Consider next the positioning of the superconvergent points. Since the existing method of superconvergence is restricted to structured meshes, the position of these points in the case of unstructured meshes needs to be considered anew. This was done for example by Liew and Rajendran (2002) and Rajendran and Liew (2003) in their extension of the best-fit approach to 2D problems. In the current work, the best-fit approach is extended to investigate the position of the optimal points in two neighboring elements for the unstructured case. To this end, we first review the best-fit procedure proposed by Liew and Rajendran (2002); Prathap (1996); Rajendran and Liew (2003).

The best-fit approach is based on the weak form of momentum balance.

$$\int_v \delta \bar{\boldsymbol{\epsilon}} \cdot \boldsymbol{\sigma} \, dv - \int_v \delta \bar{\boldsymbol{u}} \cdot (\rho \boldsymbol{a} - \rho \boldsymbol{b}) \, dv - \int_A \delta \bar{\boldsymbol{u}} \cdot \boldsymbol{t} \, da = 0. \quad (1.14)$$

Slight rearranging leads to

$$\int_v \delta \bar{\boldsymbol{\epsilon}} \cdot \bar{\boldsymbol{\sigma}} \, dv - \int_v \delta \bar{\boldsymbol{u}} \cdot (\rho \boldsymbol{a} - \rho \boldsymbol{b}) \, dv - \int_A \delta \bar{\boldsymbol{u}} \cdot \boldsymbol{t} \, da = \int_v \delta \bar{\boldsymbol{\epsilon}} \cdot (\bar{\boldsymbol{\sigma}} - \boldsymbol{\sigma}) \, dv. \quad (1.15)$$

Here, $\boldsymbol{\sigma}$ represents the exact stress field, $\bar{\boldsymbol{\sigma}}$, $\delta \bar{\boldsymbol{u}}$, and $\delta \bar{\boldsymbol{\epsilon}}$ the corresponding finite element quantities. In this form, the left side of the expression represents the FE-formulation which, in combination with the weak form of momentum balance, enforces the orthonormality condition

$$\int_v \delta \bar{\boldsymbol{\epsilon}} \cdot (\bar{\boldsymbol{\sigma}} - \boldsymbol{\sigma}) \, dv = 0 \quad (1.16)$$

to determine the position of the optimal point. Here, $\boldsymbol{\sigma}$ is the array of Voigt components of the exact stress field, $\bar{\boldsymbol{\sigma}}$ its numerical approximation, and $\bar{\boldsymbol{\epsilon}}$ the array of corresponding strain field components. In the simple linear elastic case, (1.16) becomes

$$\int_v \delta \bar{\boldsymbol{\epsilon}}, \mathbf{C}(\bar{\boldsymbol{\epsilon}} - \boldsymbol{\epsilon}) dv = 0, \quad (1.17)$$

where \mathbf{C} is the Voigt matrix representation of the linear elasticity tensor. To get the best-fit points in one element, Rajendran and Liew (2003) restricted (1.17) to just one element. In this case,

$$\bar{\boldsymbol{\epsilon}} = \mathbf{B}\bar{\mathbf{u}} \quad (1.18)$$

holds for the finite element strain field in terms of the nodal displacements \mathbf{u} and standard \mathbf{B} -matrix \mathbf{B} . The exact solution is unknown, thus, the exact displacement field is represented by a polynomial which is one order higher than the order of the standard shape function. Thus, the strain field is represented by

$$\boldsymbol{\epsilon} = \mathbf{P}\mathbf{d}. \quad (1.19)$$

Here, \mathbf{P} is a matrix whose components depend on polynomials of the position coordinates, in particular for linear triangular element, which is expressed as

$$\mathbf{P} = (1, x, y), \quad (1.20)$$

and \mathbf{d} is a set of parameters analogous to \mathbf{a} above for the stress field, which is represented by

$$\mathbf{d} = (d_1, d_2, d_3). \quad (1.21)$$

Using (1.18) and (1.19), (1.17) becomes

$$\int_{v^{(e)}} (\mathbf{B}\delta\bar{\mathbf{u}}) \cdot \mathbf{C}(\mathbf{B}\bar{\mathbf{u}} - \mathbf{P}(\mathbf{x})\mathbf{d}) dv = \delta\bar{\mathbf{u}} \cdot \int_{v^{(e)}} \mathbf{B}^T \mathbf{C} \mathbf{B} \bar{\mathbf{u}} - \mathbf{B}^T \mathbf{C} \mathbf{P}(\mathbf{x}) \mathbf{d} dv^{(e)} = 0 \quad (1.22)$$

and as $\delta\bar{\mathbf{u}}$ is arbitrary

$$\int_{v^{(e)}} \mathbf{B}^T \mathbf{C} \mathbf{B} \bar{\mathbf{u}} - \mathbf{B}^T \mathbf{C} \mathbf{P}(\mathbf{x}) \mathbf{d} dv^{(e)} = 0. \quad (1.23)$$

The latter result can be written as the linear system

$$\mathbf{K}\bar{\mathbf{u}} = \mathbf{M}\mathbf{d}, \quad (1.24)$$

where

$$\mathbf{K} = \int_{v^{(e)}} \mathbf{B}^T \mathbf{C} \mathbf{B} dv^{(e)} \quad (1.25)$$

and

$$\mathbf{M} = \int_{v^{(e)}} \mathbf{B}^T \mathbf{C} \mathbf{P} dv^{(e)}. \quad (1.26)$$

The result (1.24) is solved for $\bar{\mathbf{u}}$ in terms of \mathbf{d} . The corresponding error in the stress, \mathbf{e}_σ , is expressed as

$$\mathbf{e}_\sigma = \mathbf{C}(\mathbf{B}\bar{\mathbf{u}} - \mathbf{P}\mathbf{d}) . \quad (1.27)$$

Setting this error to zero, one can solve the equation to obtain the position of the optimal points.

Next, consider the extension of the best-fit approach to two neighboring linear triangular elements (see Figure 1.5) for determination of the optimal point in neighboring elements. The

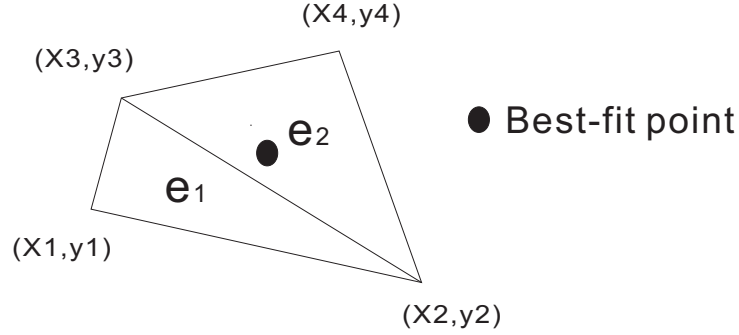


Figure 1.5: The position of the best-fit point.

exact displacement field in two neighboring elements is assumed to be a quadratic polynomial taking the form

$$\begin{aligned} u &= a_1 + a_2x + a_3y + a_4x^2 + a_5xy + a_6y^2 , \\ v &= a_7 + a_8x + a_9y + a_{10}x^2 + a_{11}xy + a_{12}y^2 . \end{aligned} \quad (1.28)$$

Now, enforcing the relation (1.17) to be valid in each element, we have

$$\int_{v^{(e_1)}} \mathbf{B}^T \mathbf{C} \mathbf{B} \, dv^{(e_1)} \bar{\mathbf{u}}^1 = \int_{v^{(e_1)}} \mathbf{B}^T \mathbf{C} \mathbf{P} \, dv^{(e_1)} \mathbf{d} \quad (1.29)$$

and

$$\int_{v^{(e_2)}} \mathbf{B}^T \mathbf{C} \mathbf{B} \, dv^{(e_2)} \bar{\mathbf{u}}^2 = \int_{v^{(e_2)}} \mathbf{B}^T \mathbf{C} \mathbf{P} \, dv^{(e_2)} \mathbf{d} . \quad (1.30)$$

To determine the optimal position of average derivatives of neighboring elements, the equation

$$\bar{\mathbf{e}}_\sigma = \mathbf{C}\{(\bar{\boldsymbol{\epsilon}}^1 + \bar{\boldsymbol{\epsilon}}^2)/2 - \mathbf{P}\mathbf{d}\} = \mathbf{0} \quad (1.31)$$

should be satisfied.

In case of linear triangular elements, \mathbf{B} and \mathbf{C} are constant in the range of the element. Thus, (1.29) and (1.30) become

$$\bar{\boldsymbol{\epsilon}}^1 V^{(e_1)} = \int_{v^{(e_1)}} \mathbf{P} \, dv^{(e_1)} \mathbf{d} \quad (1.32)$$

and

$$\bar{\boldsymbol{\epsilon}}^2 V^{(e_2)} = \int_{v^{(e_2)}} \mathbf{P} \, dv^{(e_2)} \mathbf{d} . \quad (1.33)$$

In combination with (1.31), this yields

$$\mathbf{0} = \left(\frac{\int_{v^{(e_1)}} \mathbf{P} \, dv^{(e_1)} \mathbf{d}}{V^{(e_1)}} + \frac{\int_{v^{(e_2)}} \mathbf{P} \, dv^{(e_2)} \mathbf{d}}{V^{(e_2)}} \right) / 2 - \mathbf{P}\mathbf{d} , \quad (1.34)$$

$$\begin{pmatrix} 1 \\ x \\ y \end{pmatrix} = \begin{pmatrix} 1 \\ \frac{1}{2} \left(\frac{\int_{v(e_1)} x dV}{V(e_1)} + \frac{\int_{v(e_2)} x dV}{V(e_2)} \right) \\ \frac{1}{2} \left(\frac{\int_{v(e_1)} y dV}{V(e_1)} + \frac{\int_{v(e_2)} y dV}{V(e_2)} \right) \end{pmatrix}. \tag{1.35}$$

The position of the optimal sampling point for the average value of two neighboring elements is the average position of the corresponding centers. Using the notation for a two-element-patch as shown in Fig. 1.5 we have in particular

$$\begin{pmatrix} x_s \\ y_s \end{pmatrix} = \begin{pmatrix} \frac{x_1}{6} + \frac{x_2}{3} + \frac{x_3}{3} + \frac{x_4}{6} \\ \frac{y_1}{6} + \frac{y_2}{3} + \frac{y_3}{3} + \frac{y_4}{6} \end{pmatrix} \tag{1.36}$$

for the corresponding sample point.

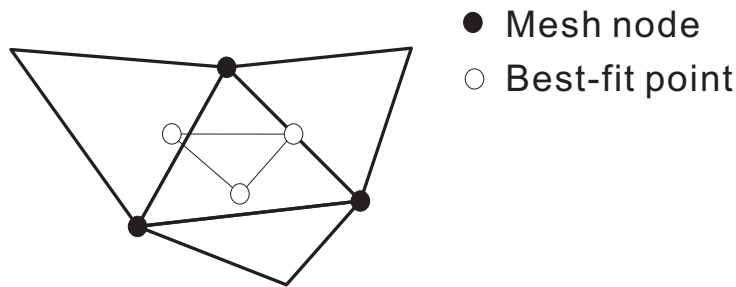


Figure 1.6: Element patch for best-fit point method.

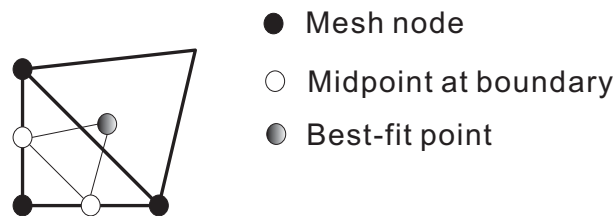


Figure 1.7: Boundary element patch.

Consider next the recovery procedure. Similar to the midpoint method, this procedure can be summarized as follows:

1. average the derivatives of neighbouring elements at the best-fit points,
2. extrapolate the average values to the nodes,
3. calculate the average value of the overlapping recovered solutions at nodes,
4. interpolate the average values at nodes with shape function. For practical purpose, the element derivative value is used for the midpoint value at a boundary element edge (see Figure 1.7).

1.4 Error estimation

The FE solution, in terms of the stresses σ^h , differs from the corresponding exact values σ . The point-wise errors are defined by the difference

$$\mathbf{e}_\sigma = \sigma - \sigma^h. \quad (1.37)$$

Since σ is unknown, a recovered solution σ^* can be obtained by some suitable recovery process in place of the exact solution σ . The error is then estimated as

$$\mathbf{e}_\sigma \approx \mathbf{e}_\sigma^* = \sigma^* - \sigma^h. \quad (1.38)$$

An integral measure which is the so-called L_2 -norm (e.g., Wiberg and Li, 1994) is used in this paper. Thus, the errors in L_2 -norm are

$$\|\mathbf{e}\| \approx \|\bar{\mathbf{e}}\| = \left(\int_{\Omega} \mathbf{e}_\sigma^* \cdot \mathbf{e}_\sigma^* \right)^{1/2}. \quad (1.39)$$

On the whole domain, Ω , the error can be obtained by summing element contributions, i.e.

$$\|\mathbf{e}\| = \left(\sum_{i=1}^n \|\mathbf{e}\|_i^2 \right)^{1/2}, \quad (1.40)$$

where $\|\mathbf{e}\|_i$ represents the contribution from element i and is obtained by integrating over the elemental sub-domain, Ω_i .

1.5 Numerical tests

To evaluate the performance of different recovery methods, we present five numerical tests. The methods, used for the numerical tests are given in Table 1.1. In what follows, the performance

Abbreviation	Method
ZZ	Original SPR method
EP1	SPR method with element patch and $p = 1$ polynomial
EP2	SPR method with element patch and $p = 2$ polynomial
EPAN2	SPR method with additional nodes (§1.2).
MP, MPN and MPAN	Midpoint methods from §1.3.
BF	Best-fit-point method from §1.3.

Table 1.1: Recovery methods compared with each other and discussed in the text.

of the error estimator is evaluated by the corresponding element and global effectivity indices

$$\theta_e = \frac{\|\bar{\mathbf{e}}\|_e}{\|\mathbf{e}\|_e} \quad (1.41)$$

and

$$\theta = \frac{\|\bar{\mathbf{e}}\|}{\|\mathbf{e}\|} \quad (1.42)$$

(e.g., Zienkiewicz and Zhu, 1987).

The first three examples to be discussed in what follows are all based on the Poisson equation

$$-\Delta u = f \quad (1.43)$$

and are to be solved on a unit square domain $\Omega = (0, 1) \times (0, 1)$. In the first example, let $u = 0$ be the boundary condition on $\partial\Omega$ and choose f so that

$$u(x, y) = \sin(\pi x) \sin(\pi y) \quad (1.44)$$

represents the exact solution.

The problem is now solved numerically on a sequence of unstructured meshes (see Figure 1.8).

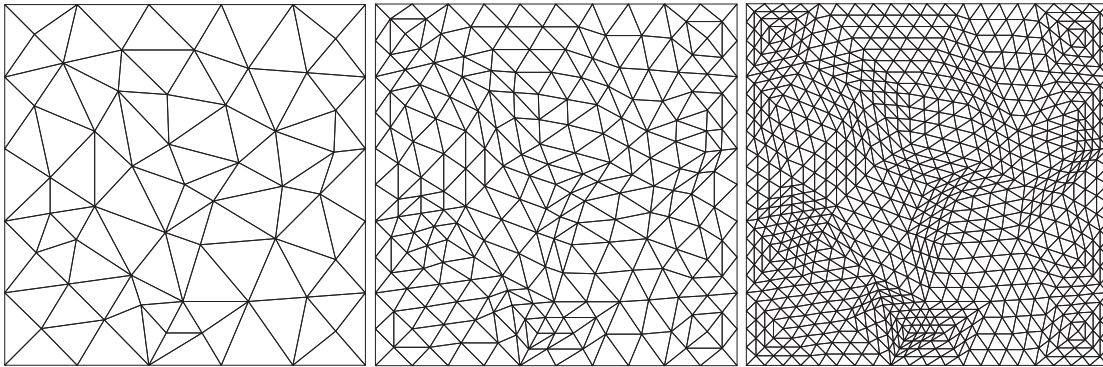


Figure 1.8: Sequence of unstructured meshes for the numerical tests 1-3.

Figure 1.9 shows the convergence of global error and global effectivity index of the derivative $u_{,x}$. Due to the symmetry of the solution, the results for $u_{,y}$ are analogous to those for $u_{,x}$ and are not presented here. It can be observed from Figure 1.9(a) that the global error of the recovered solution $u_{,x}^*$, calculated by the BF method, is the smallest of all methods, considered here. Figure 1.9(b) shows the global effectivity index of the BF method close to 1, even for the coarse mesh. It can also be observed that the EPAN2 method is more effective than the EP1 and EP2 methods. The deviation of the element effectivity index from the optimal value (“1”) for $u_{,x}$ is illustrated in Figure 1.10. The global effectivity index represents the performance of the global error estimator. In addition, the element effectivity index is also very important for local error estimation.

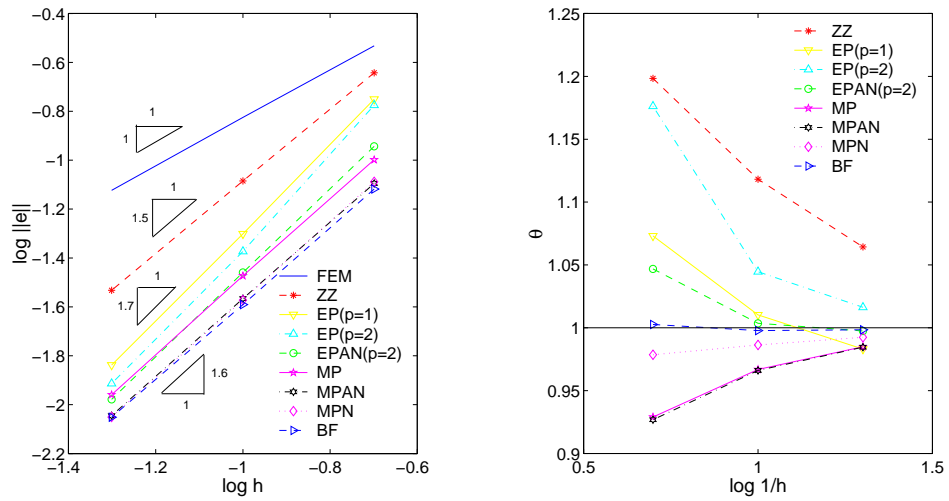


Figure 1.9: Results for the first example based on equation (1.44). a) rate of convergence of global L_2 -error in $u_{,x}$; b) global effectivity index with respect to $u_{,x}$.

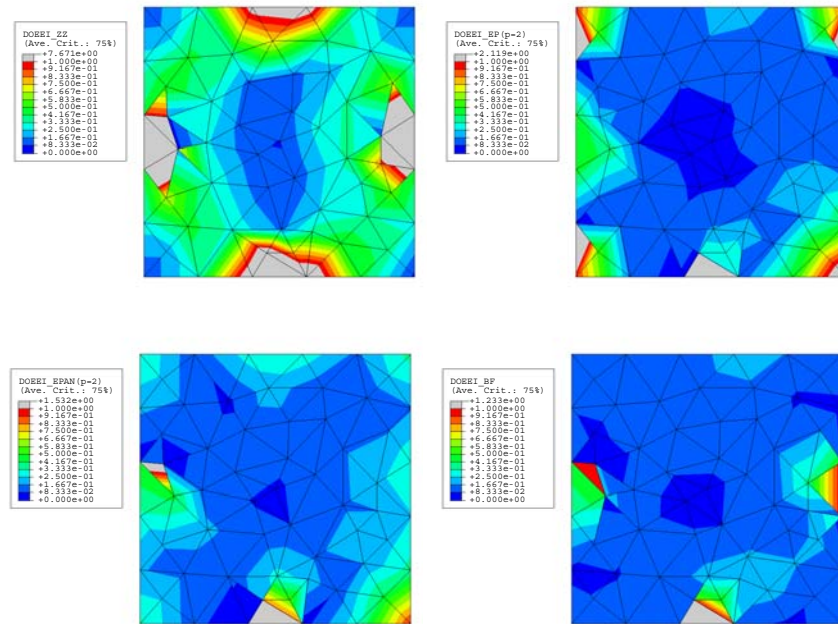


Figure 1.10: Deviation of element effectivity index from the optimal value (“1”) with respect to $u_{,x}$ for the first example based on equation (1.44). ZZ (above, left), EP2 (above, right), EPAN2 (below, left), BF (below, right).

In the second example, consider again the PDE (1.43) defined over a unit square $\Omega = (0, 1) \times (0, 1)$. The source f and boundary conditions on u are now chosen so that the exact solution is

$$u(x, y) = (x^3 + y^2) \sin(xy) . \tag{1.45}$$

The rate of convergence of the global error is presented in Figure 1.11(a) with respect to $u_{,x}$ and in Figure 1.12(a) with respect to $u_{,y}$. Comparing the MP and BF methods, it is seen that the recovered solution provided by the BF method is closer to the exact solution. This is because the midpoint is not the optimal point in an unstructured mesh.

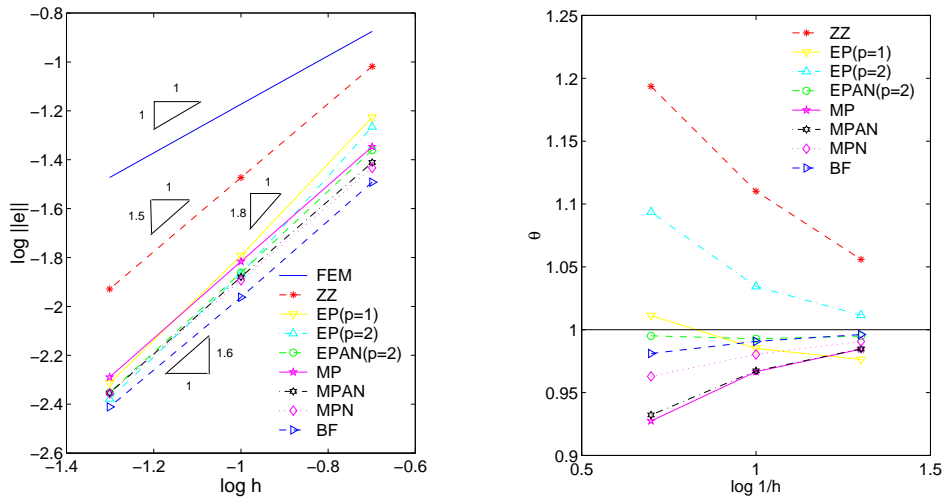


Figure 1.11: Results for the second example based on equation (1.45). a) rate of convergence of global L_2 -error with respect to $u_{,x}$; b) global effectivity index with respect to $u_{,x}$.

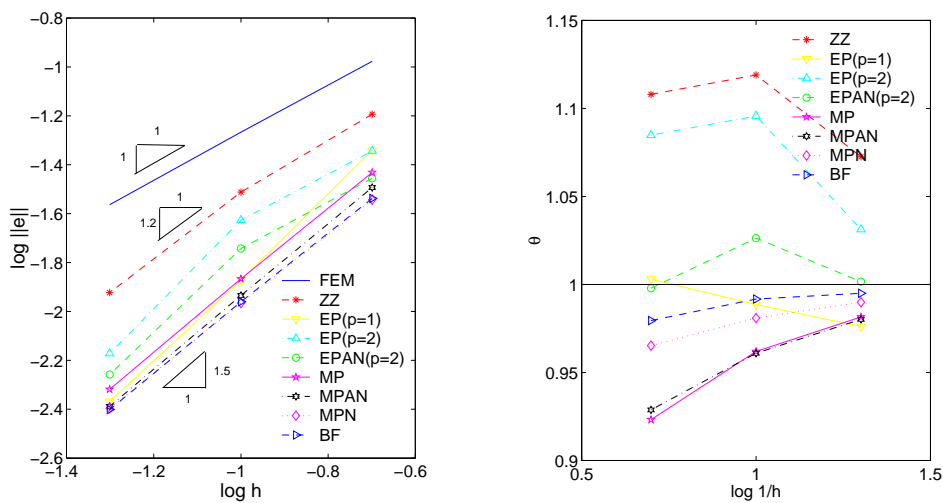


Figure 1.12: Results for the second example based on equation (1.45). a) rate of convergence of global L_2 -error with respect to $u_{,y}$; b) global effectivity index with respect to $u_{,y}$.

From Figure 1.11(b) and Figure 1.12(b), it is observed that the ZZ method overestimates the error and the MP method underestimates it. This is in contrast to the BF method, which performs well. The deviation of the element effectivity index of $u_{,x}$ and $u_{,y}$ are illustrated in Figures 1.13 and 1.14, respectively. In the case of the BF method, we note that the effectivity index of most elements are close to 1. In contrast, in the case of the ZZ method, the deviation of element effectivity index is greater, especially near the boundary. Due to lacking neighboring elements on the other side of the boundary, the performance of the ZZ recovery technique on a boundary patch is worse than that on an interior patch (Babuska et al., 1997c).

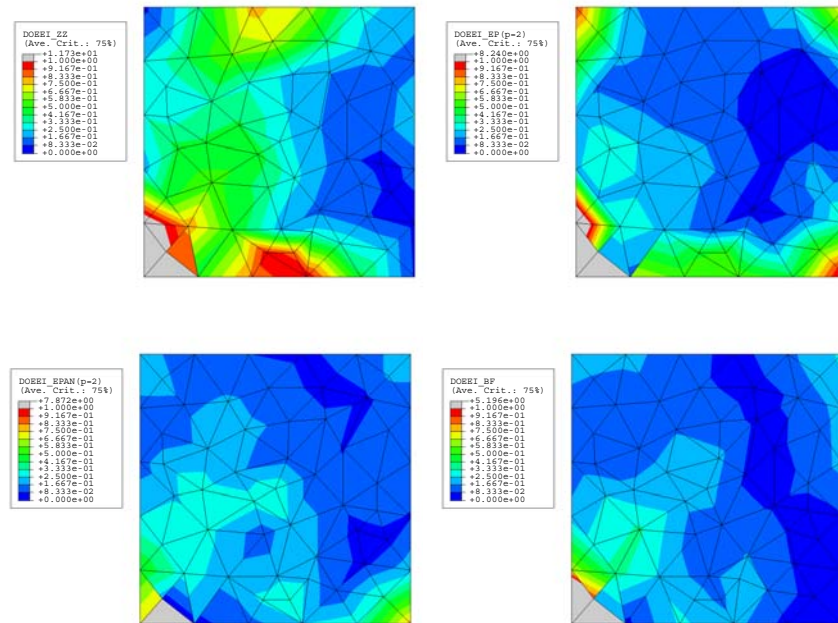


Figure 1.13: Deviation of element effectivity index from the optimal value (“1”) with respect to $u_{,x}$ for the first example based on equation (1.45). ZZ (above, left), EP2 (above, right), EPAN2 (below, left), BF (below, right).

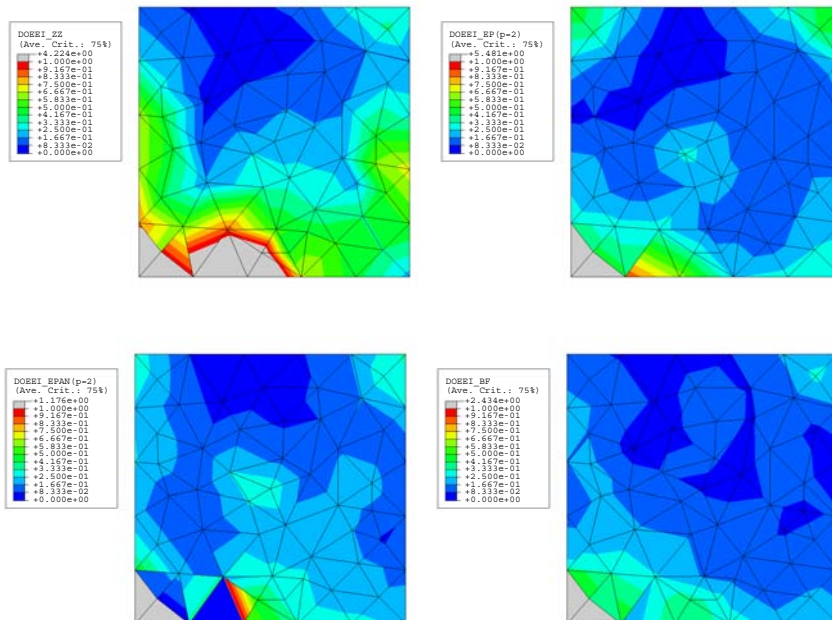


Figure 1.14: Deviation of element effectivity index from the optimal value (“1”) with respect to $u_{,y}$ for the first example based on equation (1.45). ZZ (above, left), EP2 (above, right), EPAN2 (below, left), BF (below, right).

The third example is based again on Equation (1.43) defined over $\Omega = (0, 1) \times (0, 1)$. The boundary condition on u and f are chosen so that

$$u(x, y) = x(1 - x)y(1 - y) \tan^{-1}(20((x + y)/\sqrt{2} - 0.8)) \tag{1.46}$$

represents the exact solution. Figure 1.15 shows the distribution of the exact stress field, the FEM stress field and the recovered stress field. The latter are calculated using the ZZ and BF methods. The distribution of exact and estimated error is presented in Figure 1.16. The maximum and minimum error are also given in Figure 1.16, as can be observed, the BF method provides more accurate error estimation.

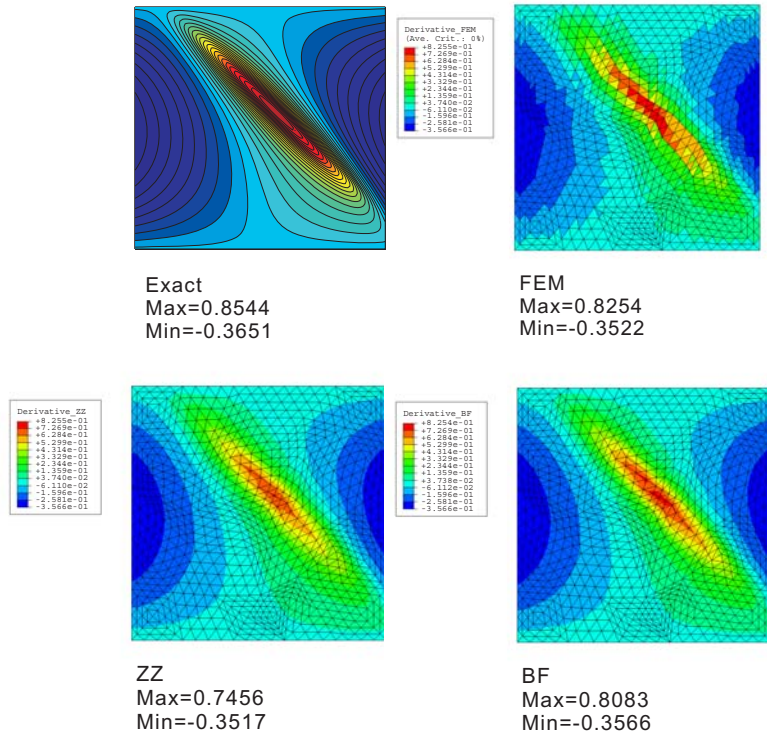


Figure 1.15: Distribution of exact and recovered values for $u_{,x}$ from the third example as based on equation (1.46).

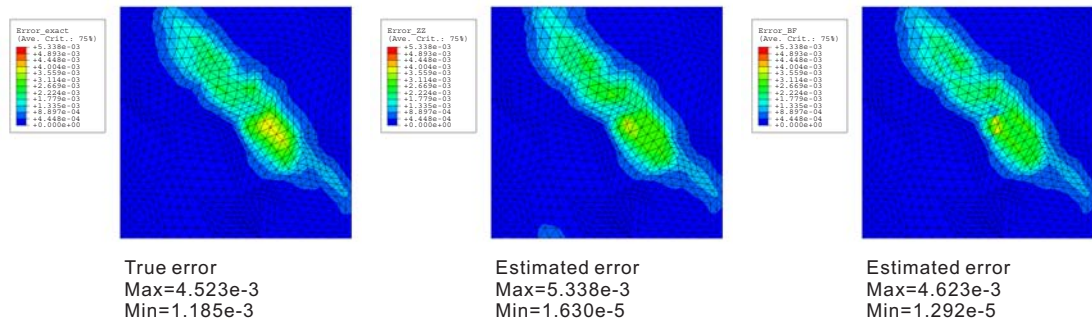


Figure 1.16: Distribution of exact and estimated element-based L_2 -error (ZZ, middle; BF, right) with respect to $u_{,x}$ from the third example as based on equation (1.46).

The fourth example to be considered in this section is a linear elastic problem in the plane, used by Rajendran and Liew (2003). This assembling involves a rectangular plate with a uniformly distributed pinching load as shown in Figure 1.17. The numerical values for l , c , a and

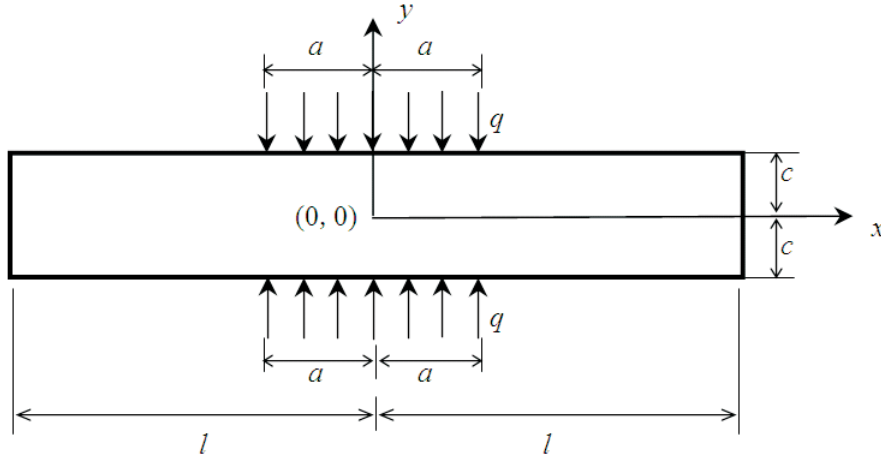


Figure 1.17: Example 4: a rectangular plate with a uniformly distributed pinching load, as used by Rajendran and Liew (2003).

q are set to 5 m, 2 m, 2 m and 1 Pa, respectively. Plane stress condition are assumed with elastic isotropic behavior based on a value for Young's modulus of 200 GPa and for Poisson's ratio of 0.3. The exact solution for σ_{yy} is given by

$$\sigma_{yy} = -\frac{qa}{l} - \frac{4q}{\pi} \sum_{m=1}^{\infty} f(m, a, c) \cos(m\pi x/l), \quad (1.47)$$

with

$$f(m, a, c) = \frac{\sin(m\pi a/l)}{m} \frac{(m\pi c/l) \cosh(m\pi c/l) + \sinh(m\pi c/l)}{\sinh(2m\pi c/l) + 2(m\pi c/l)}. \quad (1.48)$$

The recovered stress σ_{yy}^* is examined at the node with coordinates of $(0, 0)$ by comparing the recovered value and the exact solution, where the exact solution has the value of $\sigma_{yy} = -1.022411$. Three meshes (see Figure 1.18) are used in the analysis. The convergence of recovered solutions are plotted in Figure 1.19. As can be observed, the BF method provides more accurate recovered value at $(0, 0)$ for all these three meshes, which proves that the BF method is better suited for local stress recovery.

Since structured meshes are being used, the best-fit point and the midpoint coincide with each other. In this case, the BF method is identical with the MPN method.

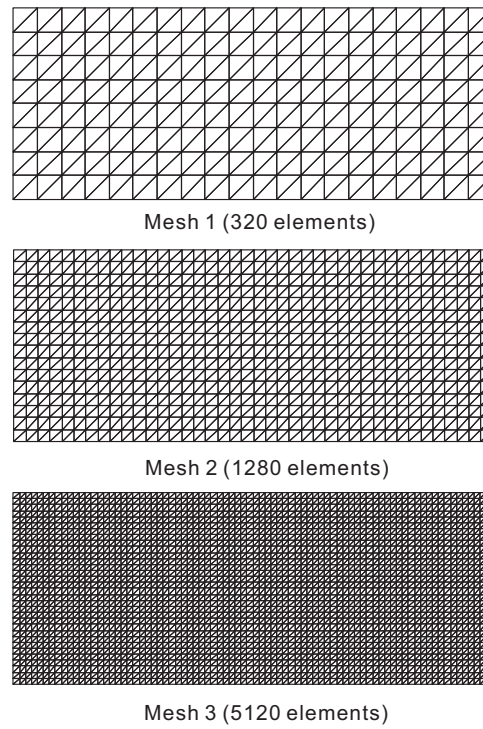
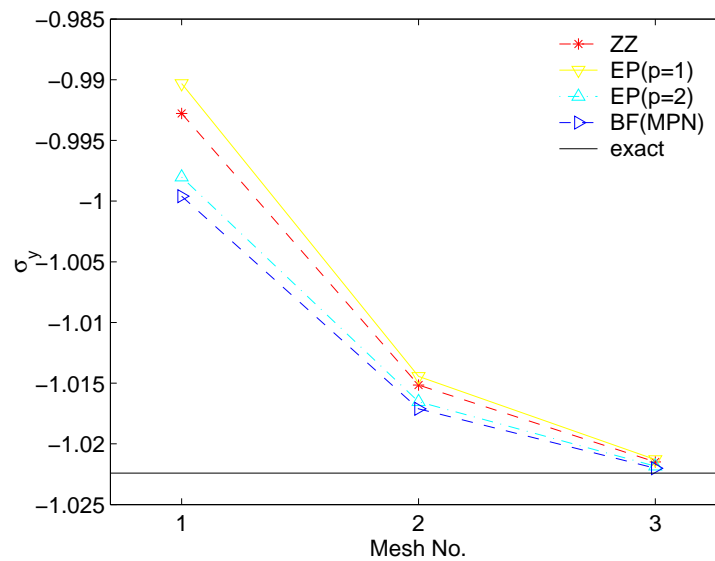


Figure 1.18: Sequence of structured meshes for the fourth example.

Figure 1.19: Convergence of σ_{yy} at $(0, 0)$ in the fourth example as based on equation (1.48).

In the fifth example, an annular circular plate with an internal pressure is considered (see Figure 1.20). The parameters a , b and P are set to 1 m, 3 m and 100 Pa, respectively. Young's modulus and Poisson's ratio are set to 200 GPa and 0.3, respectively.

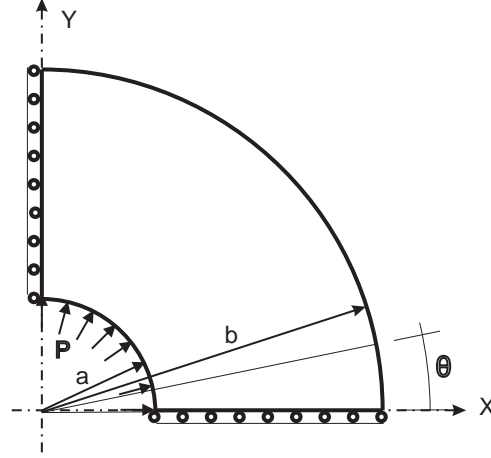


Figure 1.20: Example 5: annular circular plate subjected to internal pressure.

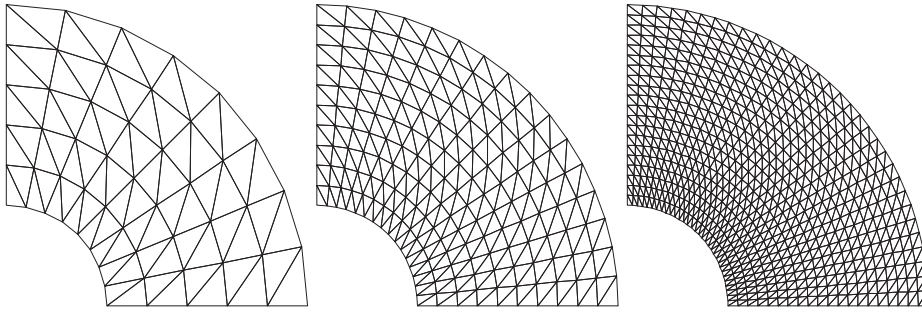


Figure 1.21: Sequence of meshes for the fifth example.

The exact stresses under the plane stress condition are given in both, polar coordinates:

$$\begin{aligned}\sigma_r &= \frac{a^2 P}{b^2 - a^2} \left(1 - \frac{b^2}{r^2} \right) \\ \sigma_\theta &= \frac{a^2 P}{b^2 - a^2} \left(1 + \frac{b^2}{r^2} \right)\end{aligned}\quad (1.49)$$

and Cartesian coordinates:

$$\begin{aligned}\sigma_x &= \frac{\sigma_r + \sigma_\theta}{2} + \frac{\sigma_r - \sigma_\theta}{2} \cos(2\theta) \\ \sigma_y &= \frac{\sigma_r + \sigma_\theta}{2} - \frac{\sigma_r - \sigma_\theta}{2} \cos(2\theta) \\ \tau_{xy} &= \frac{\sigma_r - \sigma_\theta}{2} \sin(2\theta)\end{aligned}\quad (1.50)$$

Using a sequence of meshes (see Figure 1.21) for the fifth example, the global L_2 errors in σ_x , σ_y and τ_{xy} are illustrated in Figure 1.22. Figure 1.23 shows the global effectivity index. As can be observed in Figure 1.22, the error in the ZZ recovered solution is even greater than the error in the original finite element solution when the mesh is coarse. This phenomenon was also observed by Babuska et al. (1997b). Furthermore, in the case of τ_{xy} , the global effectivity index of the ZZ method doesn't converge. In contrast, the BF method shows a good performance.

The local point-wise error and effectivity index at (1.55563, 1.55563) are shown in Figures 1.24 and 1.25, which show the convergence rate of recovered solution is higher than that of the finite element solution. In addition, the BF method shows a better local effectivity index.

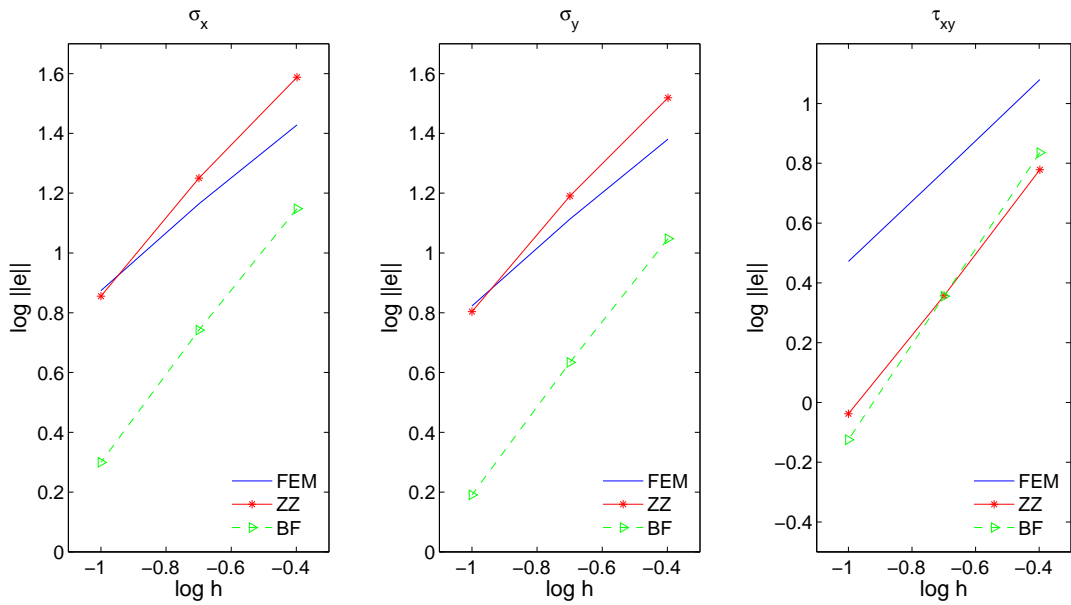


Figure 1.22: Rate of convergence for the fifth example. a) global L_2 -error in σ_x ; b) global L_2 -error in σ_y ; c) global L_2 -error in τ_{xy} .

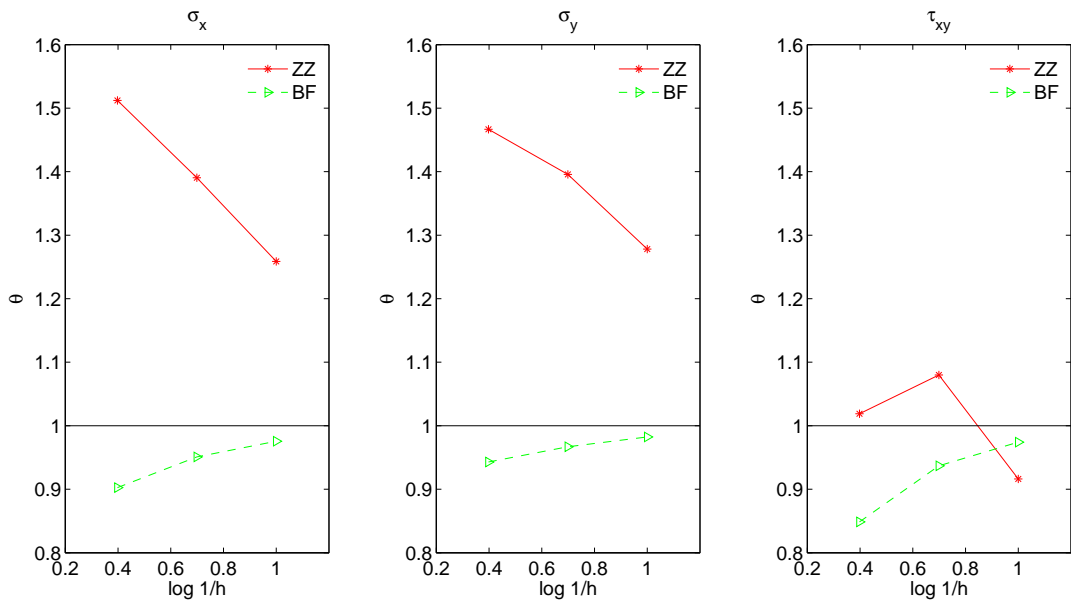


Figure 1.23: Global effectivity index for the fifth example. a) σ_x ; b) σ_y ; c) τ_{xy} .

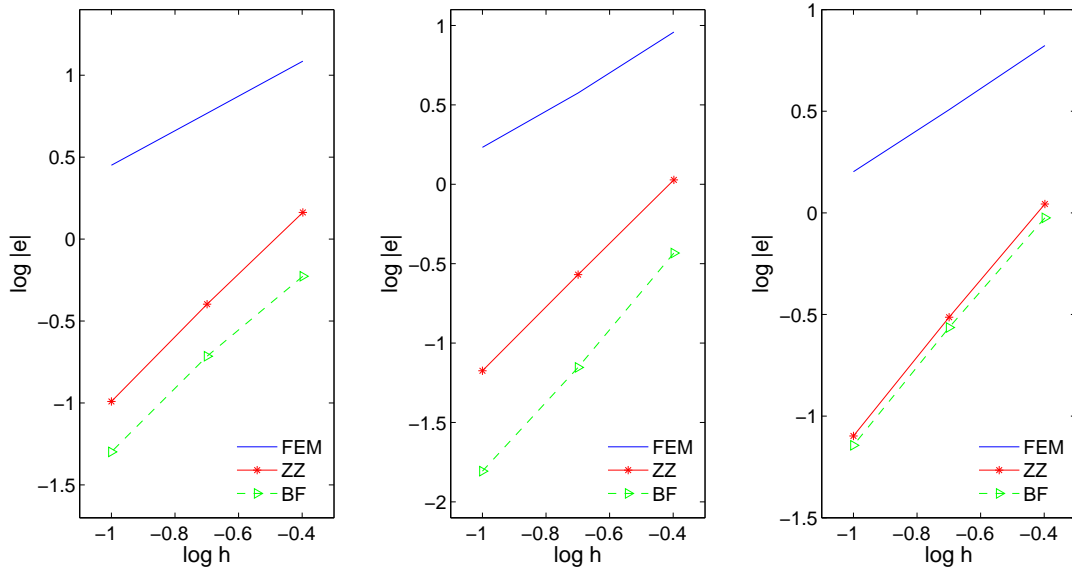


Figure 1.24: Rate of convergence for the fifth example. a) local pointwise error in σ_x at $(1.55563, 1.55563)$; b) local pointwise error in σ_y at $(1.55563, 1.55563)$; c) local pointwise error in τ_{xy} at $(1.55563, 1.55563)$.

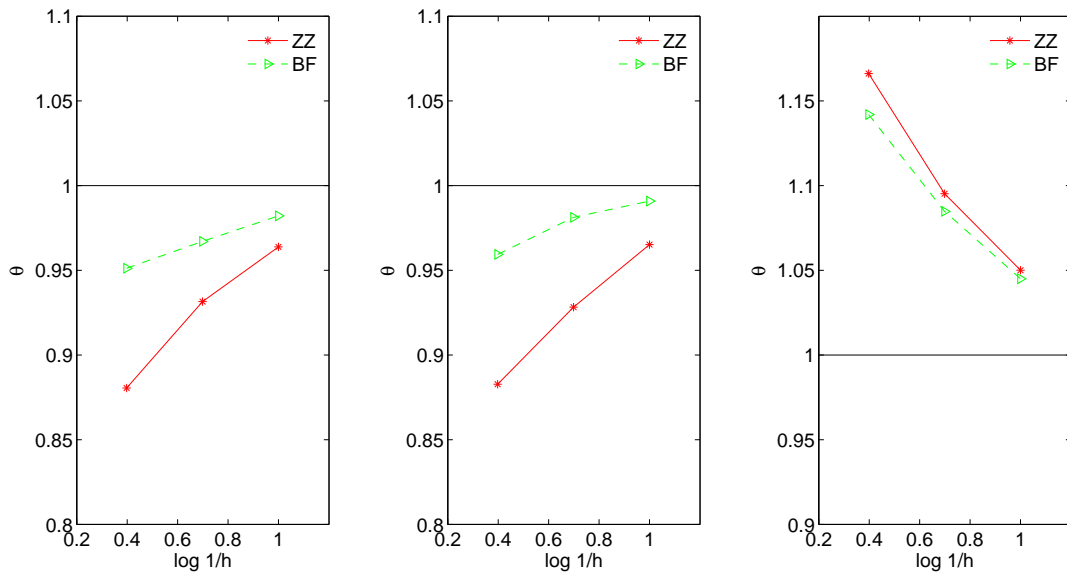


Figure 1.25: Local effectivity index at $(1.55563, 1.55563)$ for the fifth example. a) σ_x ; b) σ_y ; c) τ_{xy} .

To compare the recovered values, the recovered values are computed at the six arcs (lines 1-6 at $r = 1.0, 1.4, 1.8, 2.2, 2.6$ and 3.0 , respectively). Figures 1.26-1.28 show the recovered values of σ_x, σ_y and τ_{xy} along the lines 1-6, respectively. It is seen that the BF method provides more accurate recovered stresses, especially on the boundary.

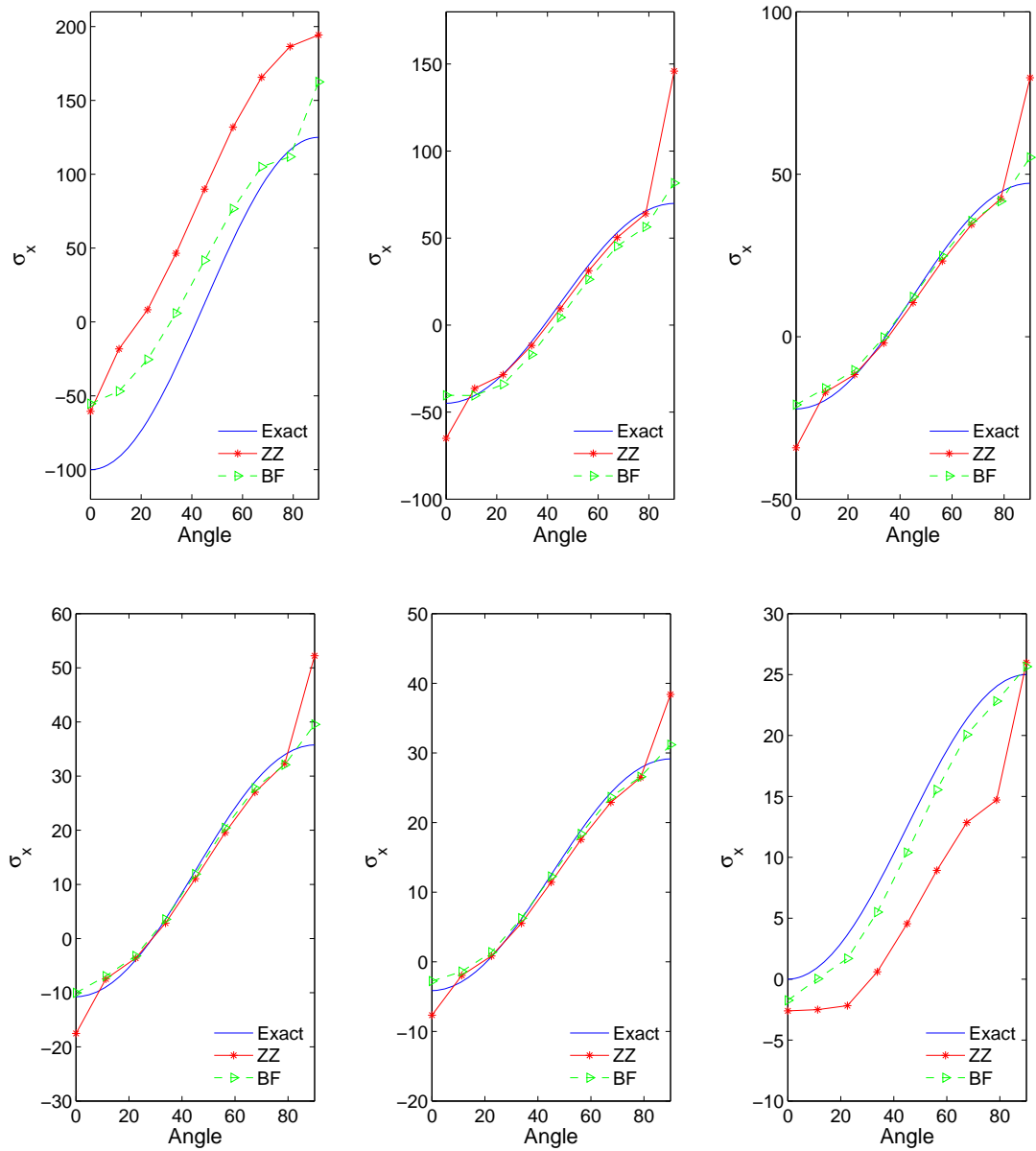


Figure 1.26: Recovered stress σ_x for the fifth example. a) Line 1; b) line 2; c) line 3; d) line 4; e) line 5; f) line6.

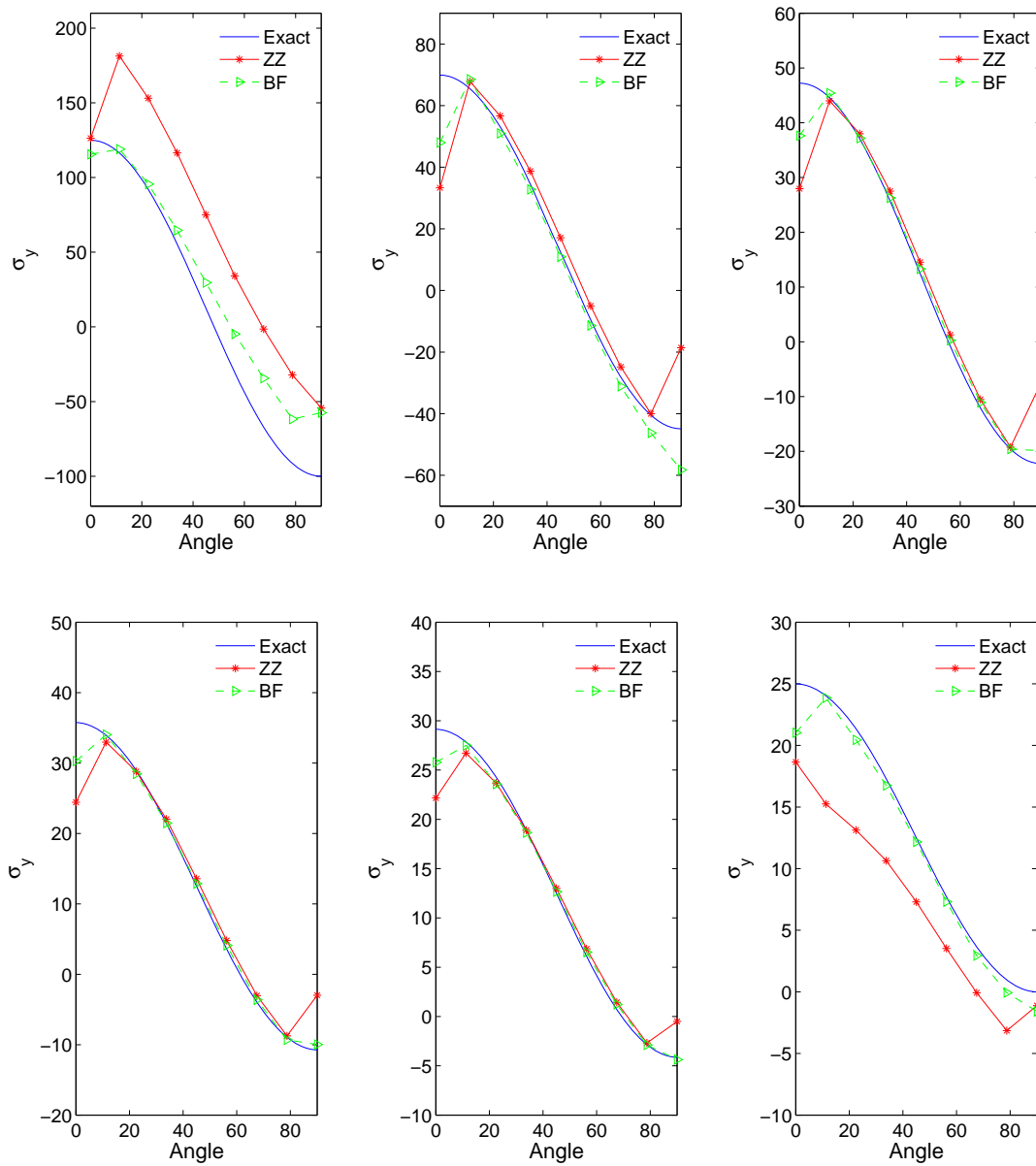


Figure 1.27: Recovered stress σ_y for the fifth example. a) Line 1; b) line 2; c) line 3; d) line 4; e) line 5; f) line 6.

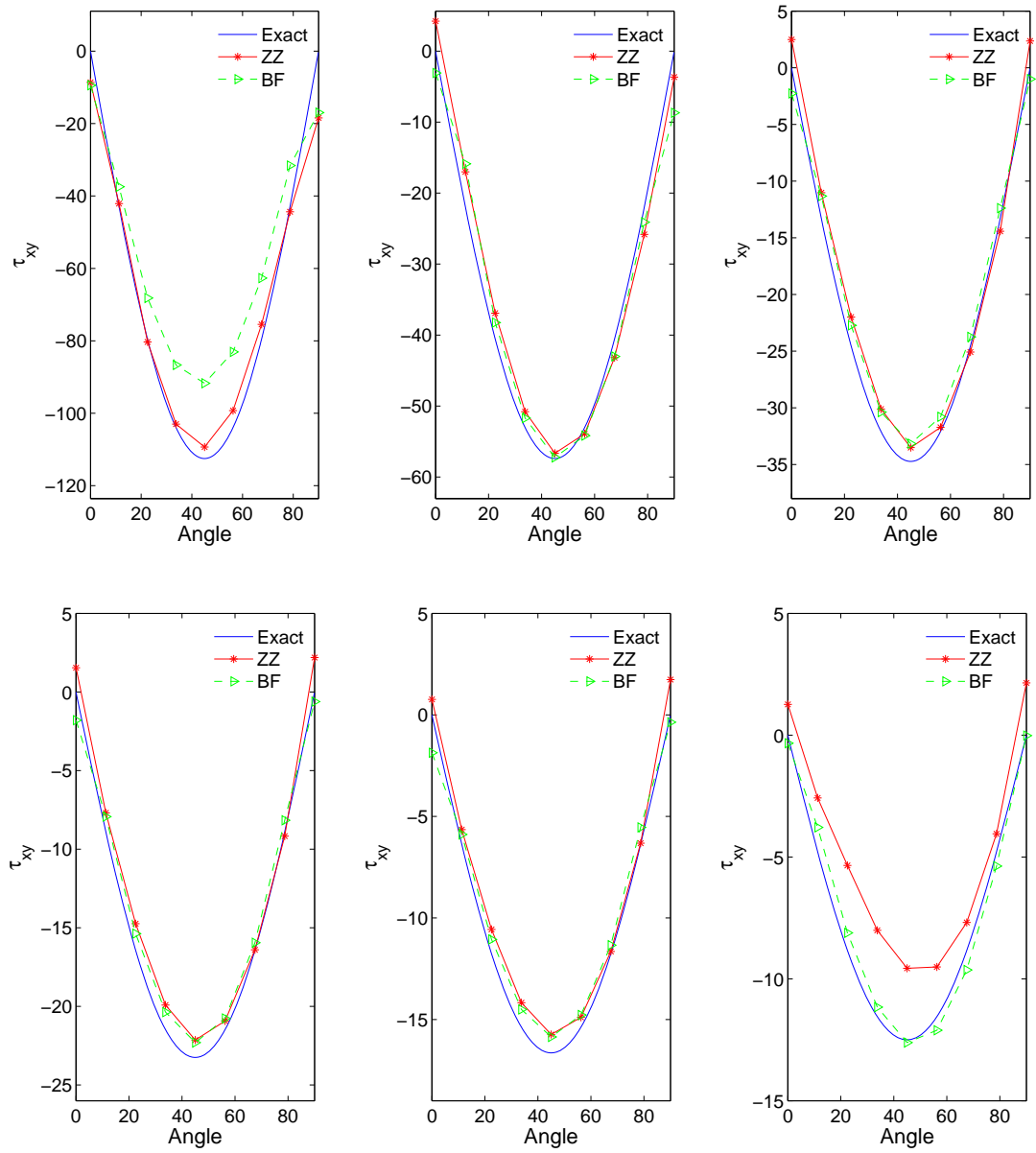


Figure 1.28: Recovered stress τ_{xy} for the fifth example. a) Line 1; b) line 2; c) line 3; d) line 4; e) line 5; f) line 6.

Figure 1.29 shows the distribution of the exact and estimated element-wise error on the second mesh in Figure 1.21. By comparing the maximum value, we note that the estimated error calculated by the BF method is closer to the exact error. The deviation of the element-wise effectivity index is shown in Figure 1.30, in which we can see that the deviation of the ZZ method is bigger than the deviation of the BF method.

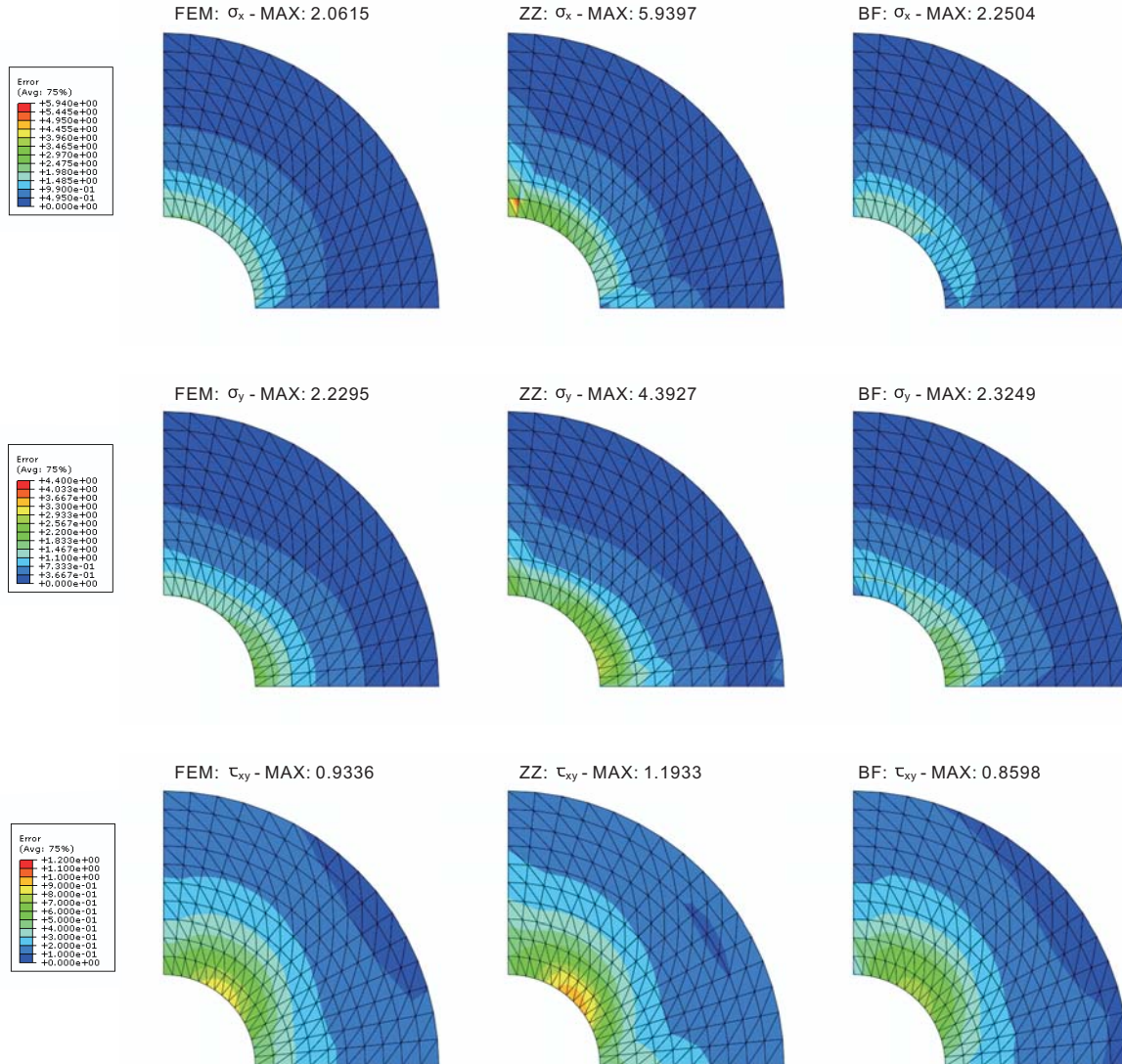


Figure 1.29: Distribution of the exact and estimated elementwise error on mesh 2, example 5.

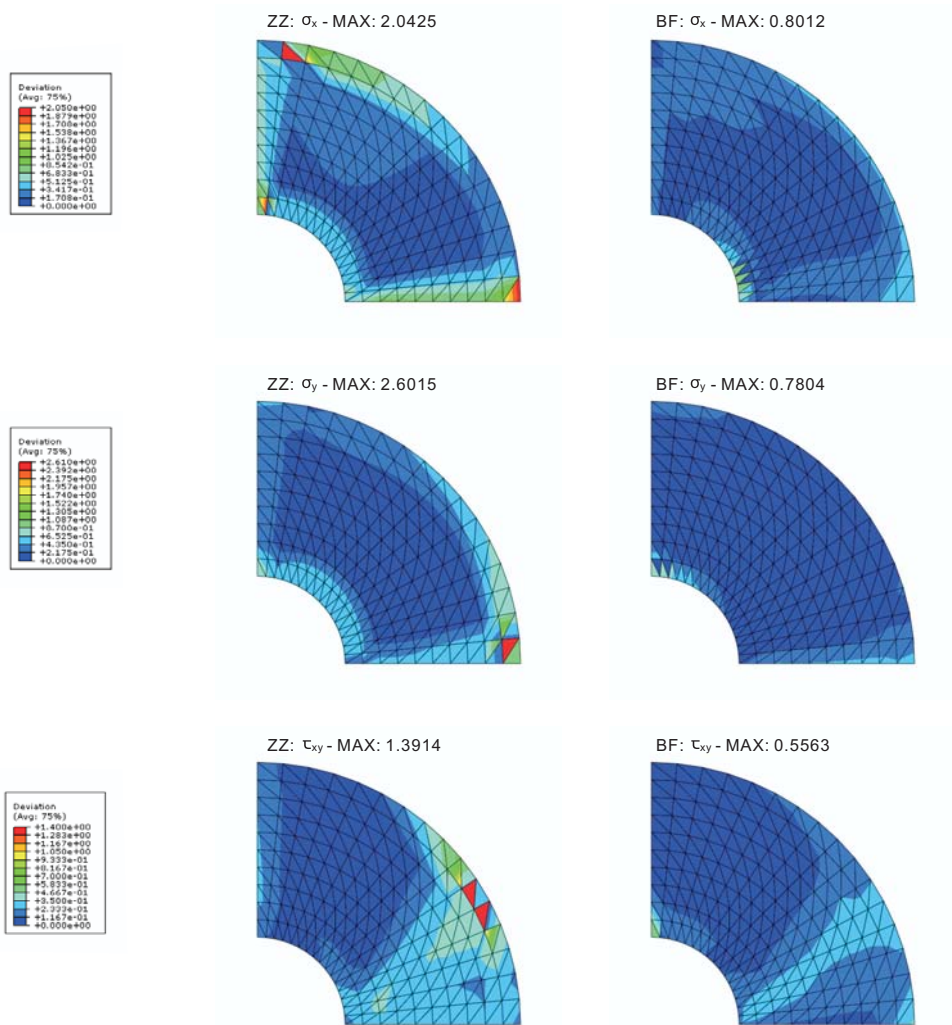


Figure 1.30: Deviation of the elementwise effectivity index on mesh 2, example 5.

Figure 1.31 shows the distribution of the element-wise error in the finite element and recovered solutions. Comparing the maximum error, we note that the BF method decreases the maximum error in the recovered solution while the ZZ method increases the maximum error in the recovered solution of σ_x and σ_y . Figure 1.32 gives the distribution of the exact and estimated point-wise error, which shows the presented recovery methods are effective for both element-wise and point-wise error estimation.

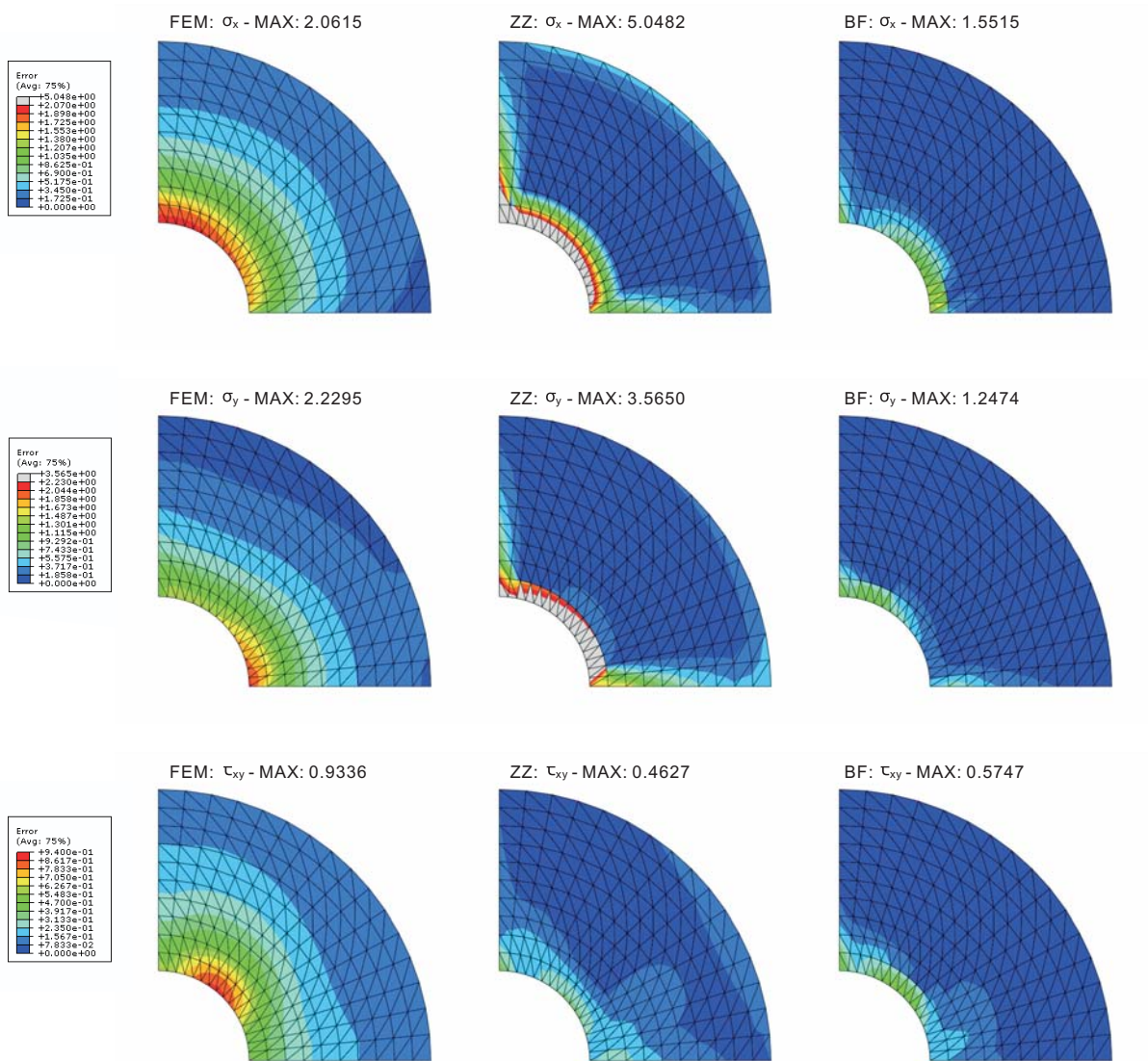


Figure 1.31: Distribution of the elementwise error in the finite element and recovered solutions on mesh 2, example 5.

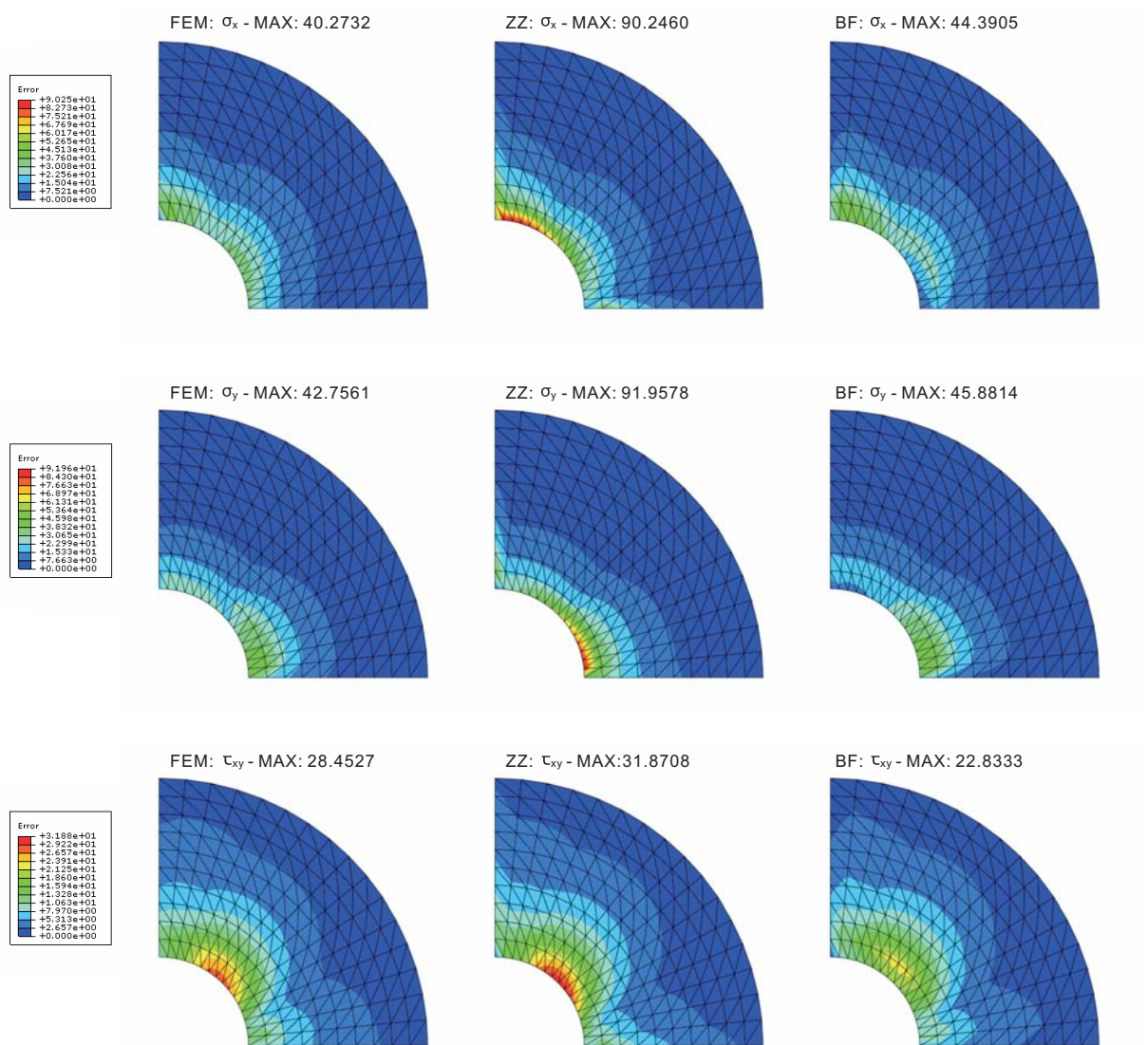


Figure 1.32: Distribution of the exact and estimated pointwise error on mesh 2, example 5.

The results of the five examples just discussed can be summarized in the following observations.

- The ZZ method tends to overestimate the global error, the recovery methods based on local extrapolation (MP, MPN, MPAN, BF) tend to underestimate the error.
- The EPAN2 method is better than the EP1 and EP2 methods.
- For structured mesh, the best-fit point and the midpoint coincide with each other. Actually, the BF method is the extension of the MPN method for unstructured mesh.
- Since the average value of neighboring elements is not optimal at midpoint but best-fit point in unstructured mesh, the performance of the BF method is better than that of the MP, MPN and MPAN methods for unstructured mesh.
- Generally, the BF method provides the most accurate error estimation in these methods which are evaluated in this paper.

1.6 *A posteriori* error estimation

In the category of recovery based error estimation, the discretization error of the finite element solution is evaluated by comparing the finite element solution and the recovered solution. In the past 20 years several recovery based error estimators have been proposed (*e.g.*, Gallimard et al., 1996; Lee and Bathe, 1994; Li and Bettess, 1997; Peric et al., 1994; Zienkiewicz et al., 1988; Zienkiewicz and Zhu, 1987, 1992a,b). For linear elasticity problems, one can simply use the derivatives of displacement or stresses to evaluate the discretization error (Lee and Bathe, 1994; Zienkiewicz and Zhu, 1992a,b, *e.g.*). In the case of nonlinear plasticity problems, it is much more sophisticated since the error estimation for plasticity problems is highly problem dependent (Li and Bettess, 1997). Here, it is recommended to design various error estimators for various simulation purposes. In the following, we will review possible quantities to be used in context of error estimation.

1.6.1 *Stress (EESS)*

The error estimator based on effective stress is designed to evaluate the error mainly for linear elasticity problems. The error $\|e\|$ is defined in L_2 -norm by

$$\|e\|_{\Omega} = \left(\int_{\Omega} (\sigma_e^* - \sigma_e^h)^2 d\Omega \right)^{1/2} \quad (1.51)$$

with σ^* , the recovered effective stress and σ^h , the finite element solution.

1.6.2 *The incremental energy (EIE)*

The error estimator based on the incremental energy was proposed by Boroomand and Zienkiewicz (1999). This error estimator is based on the increment of recovered stresses and recovered strains. The incremental energy norm is defined as

$$\|e\|_{\Omega} = \left(\int_{\Omega} |(\sigma^* - \sigma^h)(\Delta\varepsilon^* - \Delta\varepsilon^h)| d\Omega \right)^{1/2}, \quad (1.52)$$

where σ and σ^h are the recovered stresses and the finite element approximation of stresses, respectively. $\Delta\varepsilon$ and $\Delta\varepsilon^h$ are the recovered incremental strains and the finite element approximation of strains, respectively. In the n^{th} increment the above norm may be written as

$$\|e\|_{\Omega} = \left(\int_{\Omega} |(\sigma_n^* - \sigma_n^h)(\Delta\varepsilon_n^* - \Delta\varepsilon_n^h)| d\Omega \right)^{1/2}, \quad (1.53)$$

where

$$\begin{aligned} \Delta\varepsilon_n^* &= \varepsilon_n^* - \varepsilon_{n-1}^* \\ \Delta\varepsilon_n^h &= \varepsilon_n^h - \varepsilon_{n-1}^h \end{aligned} \quad (1.54)$$

Peric et al. (1994) proposed a similar error estimator with the plastic strain increment instead of the strain.

1.6.3 The incremental strain error (EIS)

Similar to the error estimator based on energy norm, we can use an error estimator which emphasizes the discretization error in strain rate. The error in the n^{th} incremental step is expressed as follows:

$$\|e\|_{\Omega} = \left(\int_{\Omega} (\Delta\varepsilon_n^* - \Delta\varepsilon_n^h)^2 d\Omega \right)^{1/2}, \quad (1.55)$$

where $\Delta\varepsilon_n^h$ is the finite element approximation of strain increment in the n^{th} incremental step, $\Delta\varepsilon_n^*$ is the recovered solution of $\Delta\varepsilon_n^h$.

1.6.4 The equivalent plastic strain error (EEPS)

In the applications to strain localization problems, we note that the strain rate based error estimators show high efficiency in catching shear band when the shear band is being formulated. However, once the strain rate lowers down, consequent mesh coarsening causes the loss of the solutions in the formulated shear band. Therefore, a total strain based error estimator needs to be considered for this special situation. Here, an error estimator based on effective plastic strain is given by

$$\|e\|_{\Omega} = \left(\int_{\Omega} (\varepsilon_{ep}^* - \varepsilon_{ep}^h)^2 d\Omega \right)^{1/2}, \quad (1.56)$$

where ε_{ep}^h is the finite element approximation of effective plastic strain and ε_{ep}^* is the recovered solution of ε_{ep}^h .

1.7 Optimization of mesh size map

After the assessment of discretization error in a finite element solution, the next step in an adaptive remeshing strategy is to generate an optimized new mesh size map based on the estimated

error. The aim of optimization of mesh size map is to achieve a prescribed solution accuracy with the least elements.

Let η be the global relative error in a finite element solution, which is defined as

$$\eta = \frac{\|e\|}{\|u_h\|}, \quad (1.57)$$

where $\|u_h\|$ is computed with the finite element solution. Then, the local relative error in the element i is expressed as

$$\eta_i = \frac{\|e\|_i}{\|u_h\|}, \quad (1.58)$$

where $\|e\|_i$ is the elemental error in the element i .

To describe the local mesh size optimization strategy, we inherit the idea about the local remeshing indicator ξ , which was proposed by Bugada (2002) and rewrite the indicator in the following form

$$\xi_i = \frac{\eta_i}{\eta_{p_i}}, \quad (1.59)$$

where η_{p_i} is the prescribed relative error in element i . Note that the current element size fits the expected element size if $\xi_i = 1$, refinement is required if $\xi_i > 1$, and coarsening is required if $\xi_i < 1$. Given a global prescribed error, one needs a criterion to determine the distribution of the prescribed error in the mesh. Several remeshing strategies have been proposed in the past 20 years (*e.g.*, Boroomand and Zienkiewicz, 1999; Bugada, 2002; Bugada and Onate, 1993; Diez et al., 2000; Diez and Huerta, 1999; Li and Bettess, 1995; Li et al., 1995; Zienkiewicz and Zhu, 1987). Generally, those strategies can be classified into two categories: 1) uniform elemental error distribution (*e.g.*, Boroomand and Zienkiewicz, 1999; Fuenmayor and Oliver, 1996; Li and Bettess, 1995; Li et al., 1995; Zienkiewicz and Zhu, 1987); 2) uniform error density distribution (*e.g.*, Bugada, 2002; Bugada and Onate, 1993).

The most popular optimization algorithm of the mesh size map is to enforce the error to be equally distributed between all elements (Zienkiewicz and Zhu, 1987). Let n be the total number of elements and η_{p_i} be the elemental prescribed relative error. Combining equations (4.15) and (4.16) in (1.40), the global prescribed relative error is then computed by

$$\eta_p = \left(\sum_{i=1}^n \eta_{p_i}^2 \right)^{1/2}. \quad (1.60)$$

Enforcing η_{p_i} to be uniformly distributed on each element, we have

$$\eta_{p_i} = \frac{\eta_p}{\sqrt{n}}. \quad (1.61)$$

Considering again equation (4.17), the local remeshing indicator ξ_i can be rewritten as

$$\xi_i = \frac{\eta_i \sqrt{n}}{\eta_p}. \quad (1.62)$$

According to the convergence rate of the discretization error, the ratio of the old local element size to the new local element size is computed by (Zienkiewicz and Zhu, 1987)

$$\frac{h_i^{old}}{h_i^{new}} = (\xi_i)^{1/p} = \left(\frac{\eta_i \sqrt{n}}{\eta_p} \right)^{1/p} \quad (1.63)$$

with p being the polynomial degree of the element interpolating functions. Hence, we obtain the new element size which is expressed as

$$h_i^{new} = h_i^{old} \left(\frac{\eta_p}{\eta_i \sqrt{n}} \right)^{1/p}. \quad (1.64)$$

1.8 Adaptivity and numerical examples

1.8.1 Annular circular plate with a internal pressure

Since there exists an analytical solution for the fifth example, it is used again to evaluate the adaptivity strategies based on the ZZ and BF error estimators. Here, the exact relative error is expressed by

$$\eta = \frac{\|e\|}{\|u\|}, \quad (1.65)$$

where $\|e\|$ is the exact error and $\|u\|$ is the exact solution. The estimated relative error η_{ZZ} and η_{BF} is evaluated by

$$\bar{\eta} = \frac{\|\bar{e}\|}{\|u_h\|}. \quad (1.66)$$

Here, we made use of the error in stresses (EESS). The initial and adapted meshes, using the BF method are given in Figure 1.33. Table 1.2 summarizes the results of the analysis for each of the adapted mesh. Figure 1.34 shows the relative error in the uniformly refined and adapted meshes. Compared to the uniformly refined mesh, less elements are required in the adapted mesh, to obtain the same accuracy.

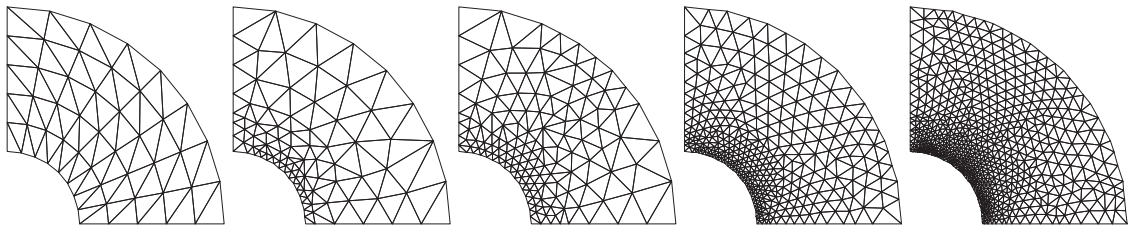


Figure 1.33: Sequence of initial and adapted meshes for the fifth example.

Mesh	Nodes	Elements	η_{BF}	η_{ZZ}	η_{ex}
1	54	80	28.43	45.17	30.71
2	94	150	16.67	20.10	16.99
3	146	247	11.95	14.31	12.23
4	370	663	7.91	8.58	8.09
5	753	1391	5.16	5.56	5.57

Table 1.2: Results of adapted meshes for the fifth example.

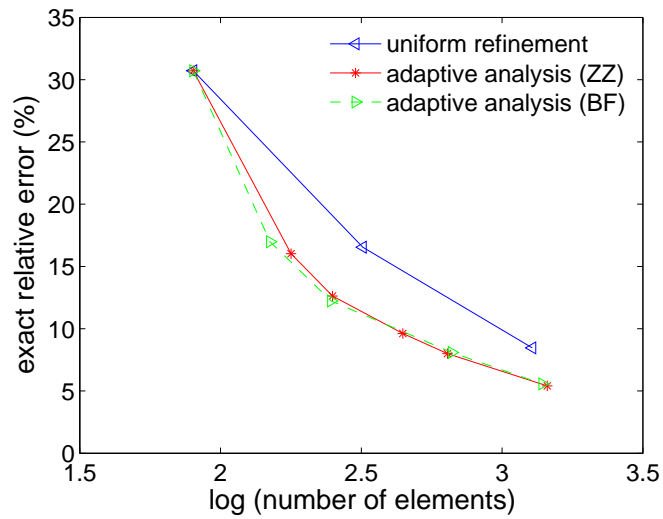


Figure 1.34: Convergence of relative error in uniformly refined and adapted meshes.

1.8.2 Bracket

The sixth example is a classical bending problem of a cantilever beam structure under plane stress conditions (see Figure 1.35). The material property of the beam is assumed to be ideal plasticity. Ten equal displacement steps are prescribed to achieve the maximum displacement of $u = 0.1$ mm along the end side.

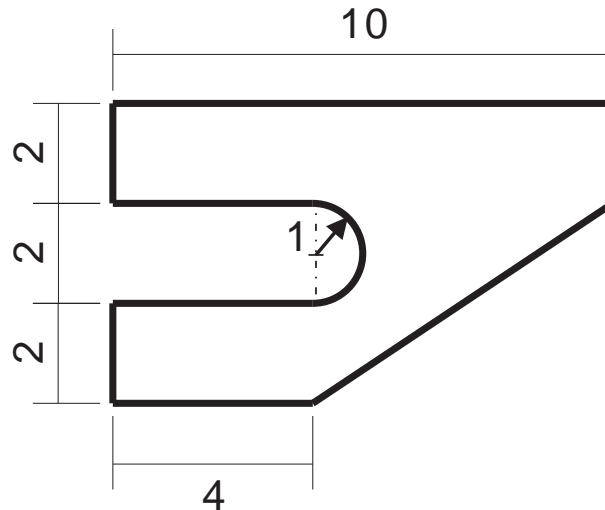


Figure 1.35: The geometry of the bracket.

Error estimators EESS and EIE are used to perform adaptive finite element analysis. The von Mises stress and equivalent plastic strain contours are shown in Figure 1.36. Initial mesh and adapted meshes are shown in Figure 1.37. It can be observed that the adaptive mesh refinement based on the EESS error estimator fails to refine the mesh where the gradient of incremental strain is relatively high. The total number of elements during the adaptive finite element analysis is shown in Figure 1.38. In the case of adaptive finite element analysis with EESS, it is seen that the number of elements increases when the displacement is less than 0.02 mm, then decreases after the displacement exceeds 0.02 mm. This phenomenon is due to the ideal plasticity material behavior, and the distribution of the stress field tends to become smooth when the material undergoes plastic deformation. Figure 1.39 shows the error histories of adaptive analysis based on the EESS and EIE error estimators, which prove the effectiveness of the adaptive remeshing strategy for error control. The load-displacement curves for the initial and adapted meshes are shown in Figure 1.40.

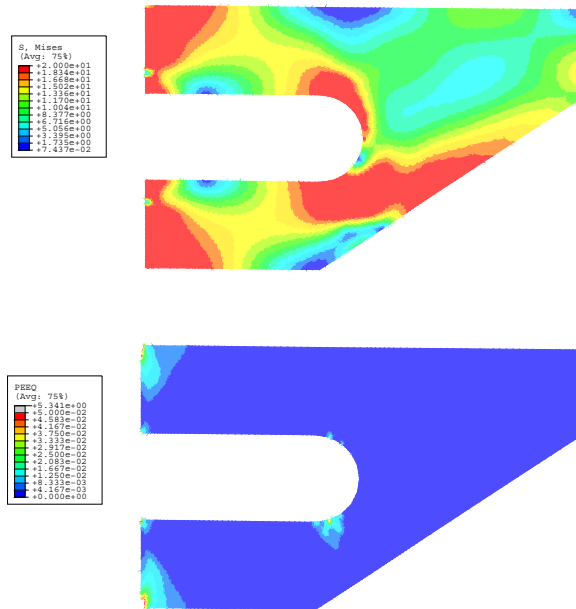


Figure 1.36: Bracket: the von Mises stress and equivalent plastic strain contours at displacement of 0.1mm.

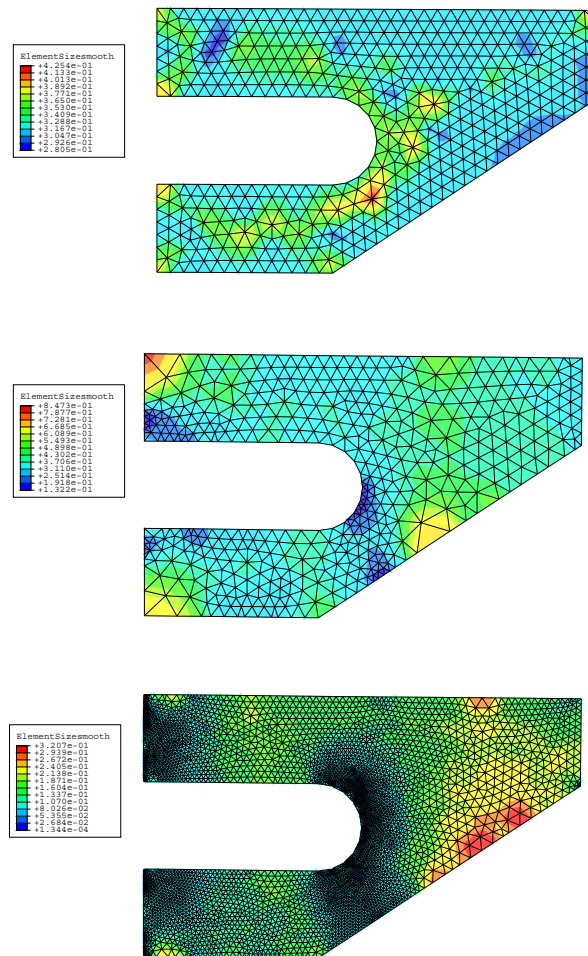


Figure 1.37: Adaptive mesh refinement for bracket. Upper: initial mesh; Middle: adapted mesh at displacement $d = 0.1$ mm based on the EESS error estimator; Lower: adapted mesh at displacement of 0.1 mm based on the EIE error estimator. Due to the ideal plasticity material behavior, the distribution of the stress field tends to become smooth when the material undergoes plastic deformation. This leads to mesh coarsening for EESS at later stages of deformation.

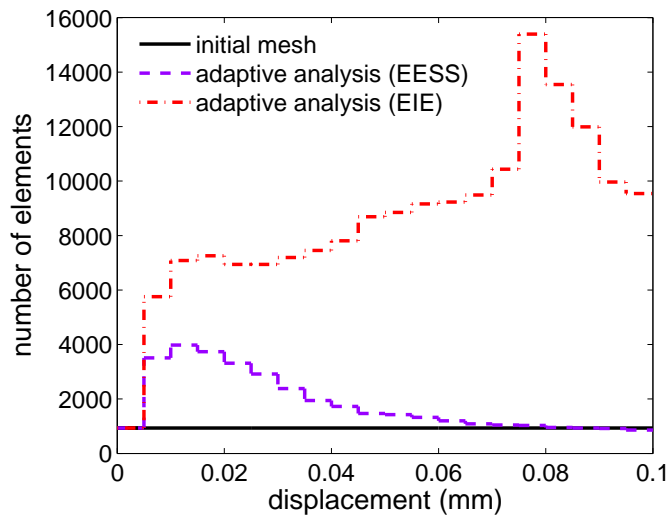


Figure 1.38: Bracket: number of elements during the adaptive analysis.

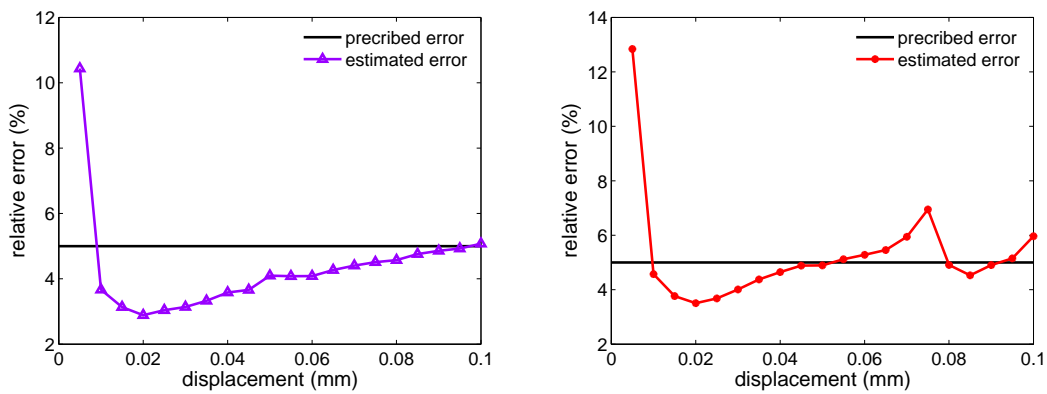


Figure 1.39: Bracket: error histories during incremental steps. Left: adaptive analysis based on the EESS error estimator; Right: adaptive analysis based on the EIE error estimator.

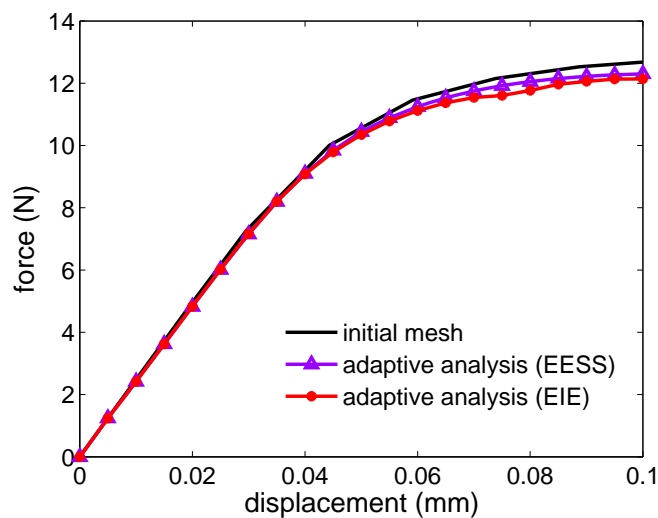


Figure 1.40: Bracket: load versus displacement for initial and adapted meshes.

1.8.3 Plate with hole

A plate with a hole subjected to uniaxial tension is considered as the seventh example. Due to the symmetry, the problem is analyzed by using one quarter of the plate. The plate is constrained at the lower edge in the y direction and the left edge in the x direction. A uniform vertical displacement is imposed at the upper edge. The material property is assumed to be ideal plasticity. Figure 1.41 shows the geometry of the plate and the boundary conditions.

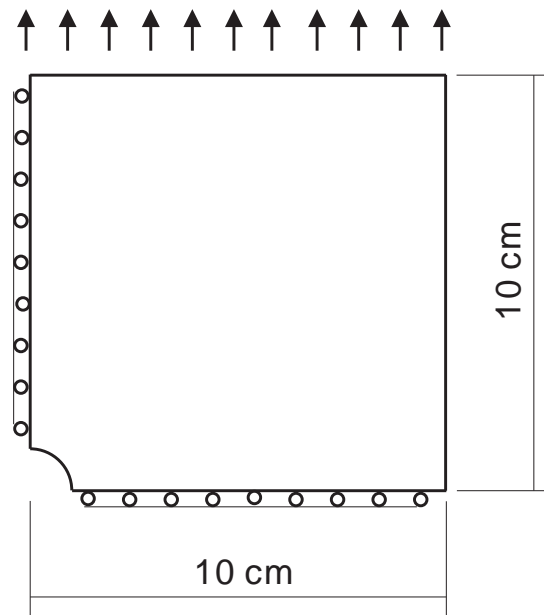


Figure 1.41: The geometry and boundary conditions of the plate with hole

Adaptive meshes at different stages of displacement using the error estimators EEPS, EIS and EIE in combination with the BF recovery technique are shown in Figure 1.42-1.44. Figure 1.45 shows the distribution of effective plastic strain in the initial and adapted meshes. As can be observed, the EEPS error estimator fails to capture the interior of the localization zone, since the maximum error can be found only at the boundary of such localization zones. The total number of elements during the adaptive finite element analysis are shown in Figure 1.46. Figure 1.48 shows the error histories of adaptive analysis based on the error estimator EEPS, EIS and EIE. The load-displacement curves for the initial and adapted meshes are shown in Figure 1.47.

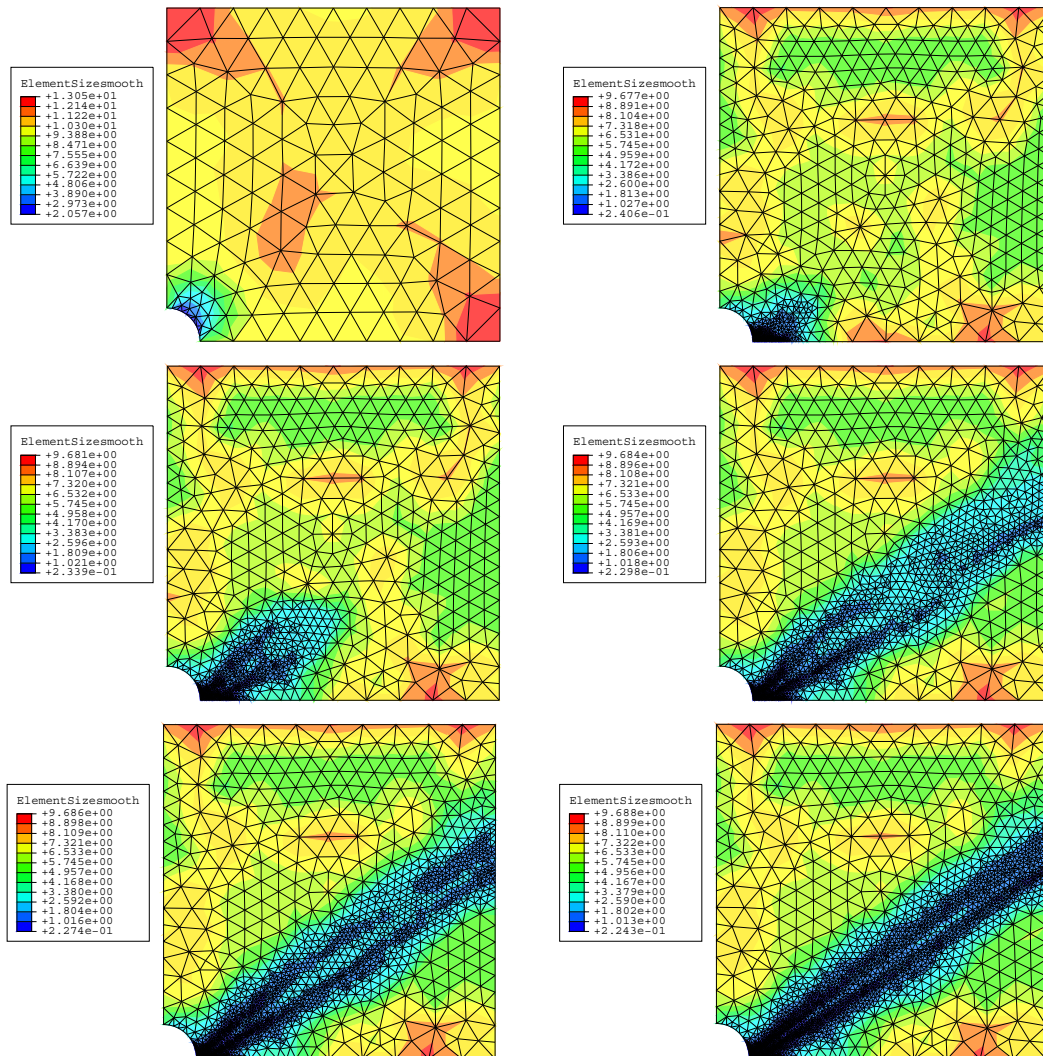


Figure 1.42: Plate with hole: adapted meshes at displacement of 0.05, 0.45, 0.50, 0.55, 0.60 and 1.0 mm using the EEPS error estimator. Note the lower mesh density in the interior of the localization zone. Here, the field is smoother than at the boundary of the zone. This leads to a lower corresponding error.

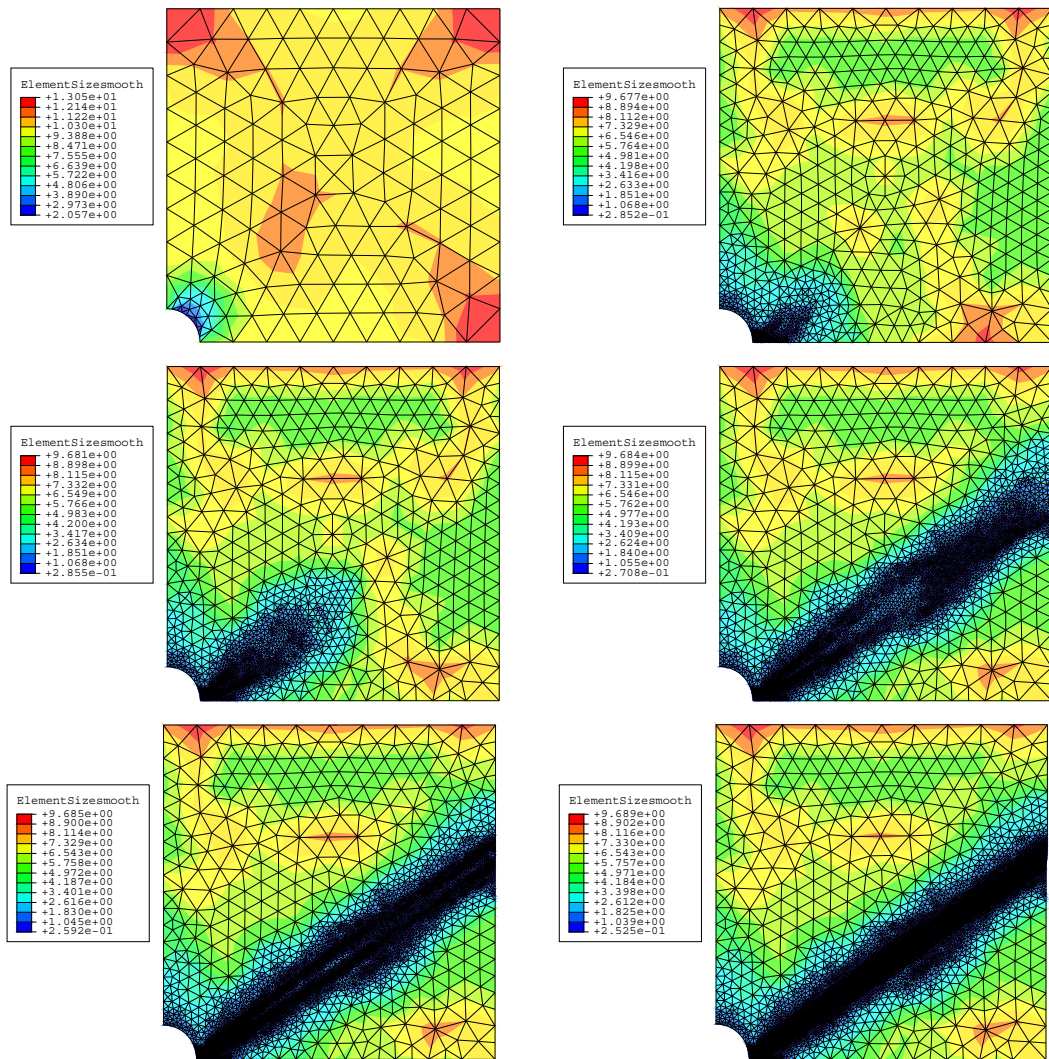


Figure 1.43: Plate with hole: adapted meshes at displacement of 0.05, 0.45, 0.50, 0.55, 0.60 and 1.0 mm using the EIS error estimator.

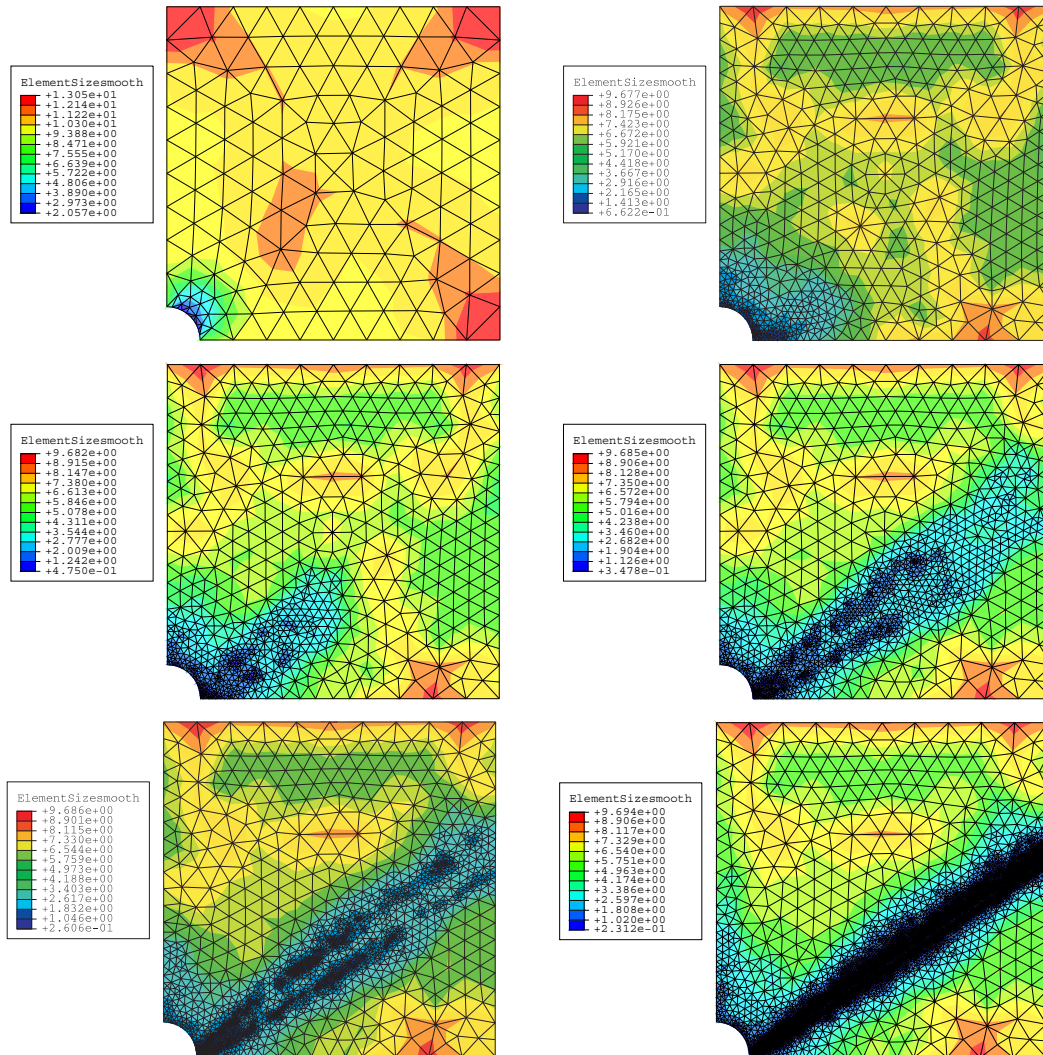


Figure 1.44: Plate with hole: adapted meshes at displacement of 0.05, 0.45, 0.50, 0.55, 0.60 and 1.0 mm using the EIE error estimator.

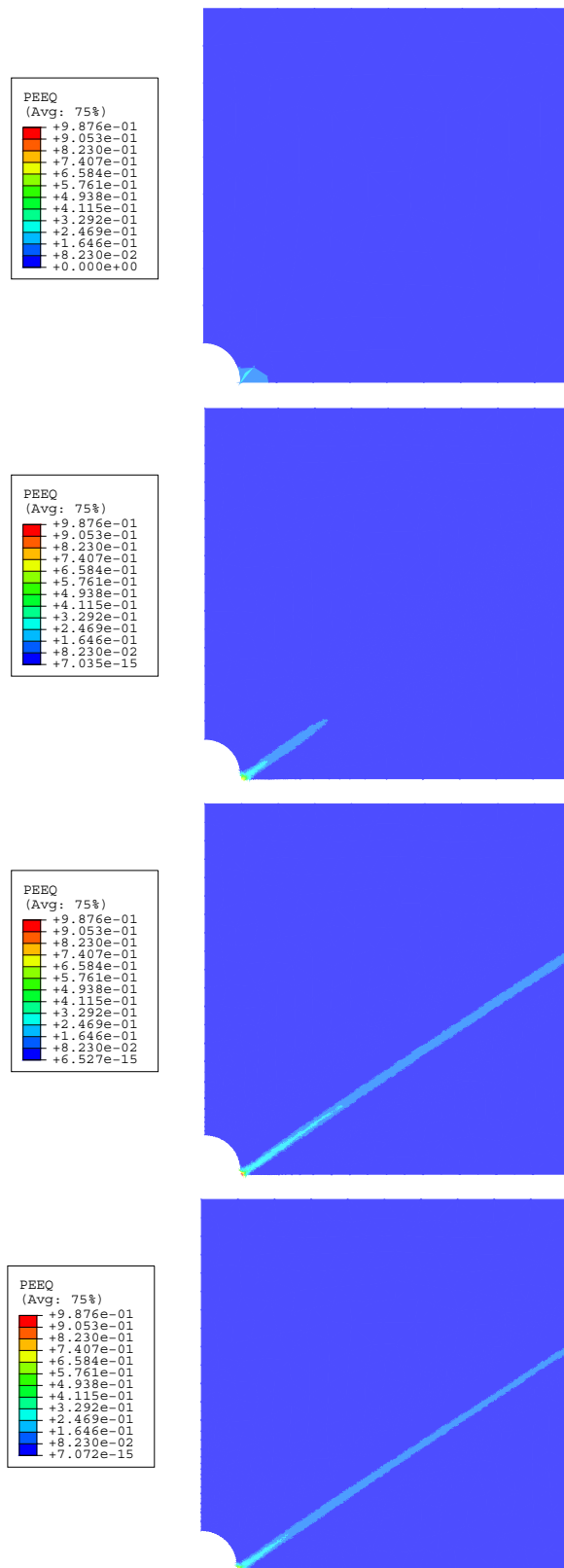


Figure 1.45: Distribution of PEEQ in the initial and adapted meshes at displacement of 1.0 mm. a) Initial mesh; b) Adapted mesh (EEPS); c) Adapted mesh (EIS); d) Adapted mesh (EIE).

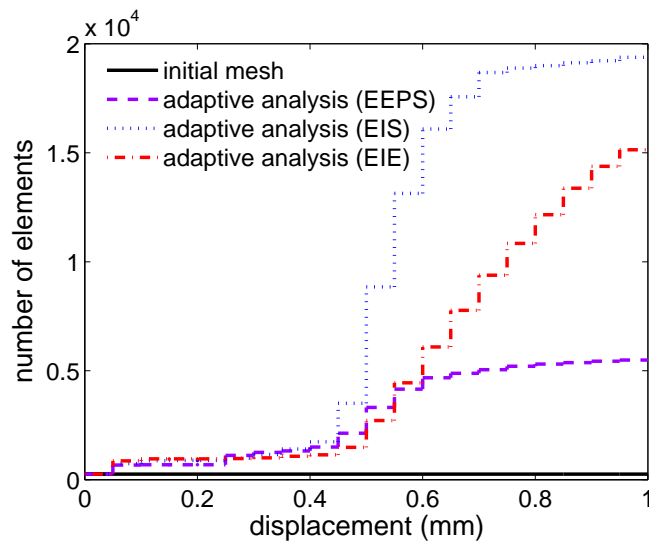


Figure 1.46: Plate with hole: number of elements during the adaptive analysis.

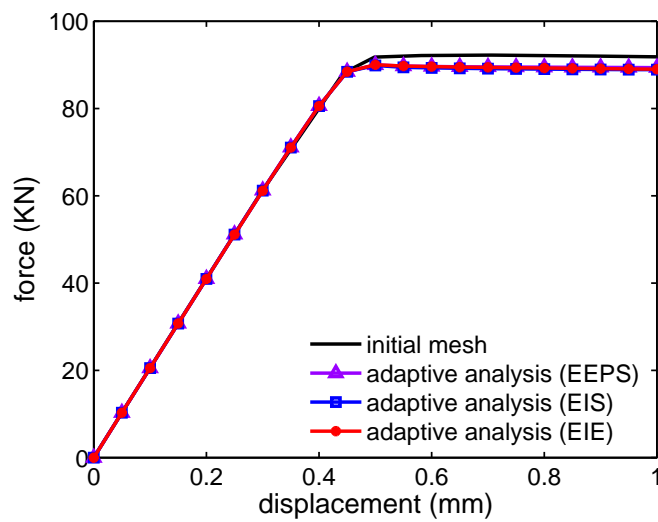


Figure 1.47: Plate with hole: load versus displacement for initial and adapted meshes.

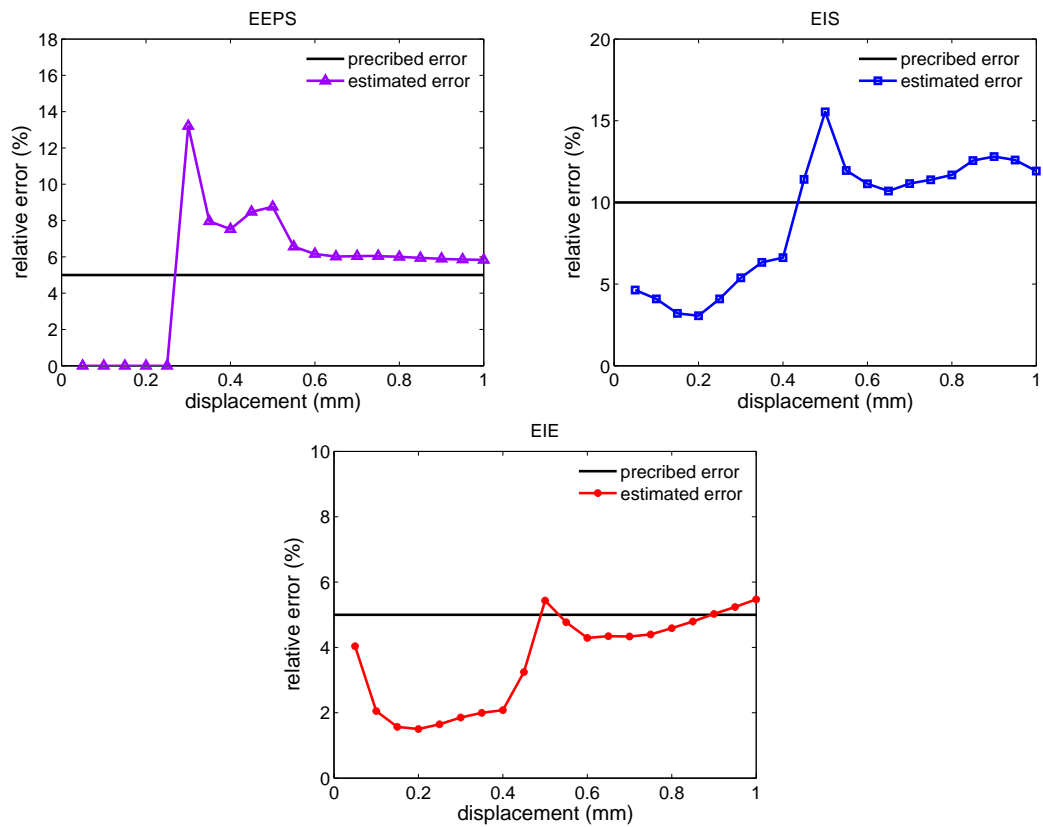


Figure 1.48: Plate with hole: error histories during incremental steps. Upper left: adaptive analysis based on the EEPS error estimator; Upper right: adaptive analysis based on the EIS error estimator; Lower: adaptive analysis based on the EIE error estimator.

1.9 Conclusions

In this chapter, several modified superconvergent patch recovery techniques and local extrapolation techniques have been proposed. The numerical tests show that the BF method provides the most accurate error estimation out of the methods which are evaluated in this chapter. To carry out adaptive finite element analysis for plasticity problems with reference to strain localization problems, several a-posterior error estimators and adaptivity strategies have been presented and compared. Numerical examples have been shown to demonstrate the presented adaptivity strategy.

Chapter 2

Automatic mesh refinement and coarsening

Abstract – In metal forming simulations, adaptive remeshing is essential for both, improving computational efficiency and maintaining mesh quality. Given a geometry, extracted from a distorted mesh, unstructured meshing techniques have been shown to be effective and robust in generating a new mesh to replace the old distorted mesh. However, there are difficulties in generating locally dense meshes. Another problem is the occurrence of distorted elements in graded meshes due to the mesh transition. In contrast, hanging-node-based hierarchical mesh refinement can easily achieve the desired local mesh density. To improve the mesh quality as well, we develop a combined unstructured and hanging-node-based remeshing strategy by exploiting the advantages of unstructured meshing techniques and hanging-node-based mesh refinement techniques. Mesh refinement and coarsening on boundary is realized by using a boundary node placement algorithm. Examples of the presented remeshing technique will be given.

Keywords: advancing front, paving, hanging node, unstructured mesh.

2.1 Introduction

During the finite element simulation of forming processes, the mesh which represents the work-piece, undergoes extreme large deformations, which could result in invalid elements and numerical failure in the simulation. To overcome these difficulties and improve computational efficiency, an adaptive remeshing technique is required to update the distorted mesh frequently.

Based on the geometry, which can be extracted from an existing distorted mesh, unstructured meshing techniques have been shown to be effective and robust in generating a new mesh to replace the old distorted mesh. However, there could be difficulties in generating local mesh densities (*e.g.*, Paving (Blacker and Stephenson, 1991)) or yield distorted elements for graded meshes due to mesh transition (*e.g.*, Krishnamoorthy et al., 1995; Sarrate and Huerta, 2000). In contrast, hanging-node-based hierarchical mesh refinement can easily achieve a desired mesh density locally. It has been widely used in Eulerian finite element formulation, in particular for fluid mechanics problems. However, there are few papers which apply hanging-node-based mesh refinement techniques to extreme large deformation problems in the context of Lagrangian finite element formulation, since it doesn't reduce mesh distortion. Using unstructured meshing technique and hanging-node-based mesh refinement technique separately, Hyun and Lindgren (2004) proposed an adaptive remeshing scheme for forging problems. That is, using the hanging-node-based mesh refinement technique at earlier stages and using the paving technique (Blacker and Stephenson, 1991) at later stages, when the deformation becomes too severe. As mentioned above, the paving technique is not able to generate local mesh densities inside interior regions. Hence, it is not suitable for strain localization problems, such as metal

cutting. To circumvent this difficulty, we develop a combined unstructured and hanging-node-based remeshing strategy by exploiting the advantages of unstructured meshing techniques and hanging-node-based refinement techniques.

The combined remeshing strategy comprises four steps:

1. extract boundary nodes from old mesh,
2. rearrange the boundary nodes according to the desired mesh density on the boundary and rebuild the geometry with updated boundary nodes,
3. perform unstructured mesh generation by projecting boundary segments towards the interior,
4. refine the unstructured mesh with hanging nodes according to the desired mesh size field.

This chapter is organized as follows. §2.2 deals with the unstructured mesh generation approach and boundary node placement algorithm. In §2.3, the fundamental concepts of hierarchical mesh refinement and coarsening are presented. Examples for the combined remeshing approach are given in the last section.

2.2 Unstructured mesh generation

In an adaptive simulation, remeshing techniques are required to re-discretize computational domains while the old spatial discretization is not suitable for further simulation. Various techniques can be utilized to create a new spatial discretization: h-adaptivity (changing the element size), p-adaptivity (changing the polynomial order of the interpolating function) and r-adaptivity (relocating the nodes without changing the topology). In this section, we focus on h-adaptivity with reference to unstructured meshing techniques, since it can not only refine or coarsen a mesh but also improve the mesh quality.

2.2.1 Advancing front meshing technique

Advancing front meshing techniques (*e.g.*, Blacker and Stephenson, 1991; Zhu et al., 1991) are commonly used by many researchers (*e.g.*, Gautham et al., 2003; Hyun and Lindgren, 2004) and commercial software (*e.g.*, ABAQUS and MSC Patran). The fundamental idea of this technique is to start mesh generation from the boundary which is constructed with boundary segments. Individual elements are generated by projecting boundary segments towards the interior. The element size is determined by the lengths of the boundary segments. After a complete row is formed, the paving boundary moves towards the interior, then mesh generation starts again on the basis of the new paving boundary. Hence, the element size, which is far from the boundary of the geometry, is essentially affected by the initial discretization of the boundary. In other words, the mesh size distribution of the generated mesh completely depends on the boundary discretization. For most metal forming simulations, this meshing technique is suitable, since the solution accuracy is mainly affected by boundary elements in contact zones instead of interior elements. However, for metal cutting problems, including strain localization, this technique can not supply interior local mesh densities. Therefore, it has to be used together with hanging-node-based mesh refinement techniques, which will be discussed in §2.3.

2.2.2 Boundary node placement

As mentioned above, the advancing front meshing technique highly depends on the boundary discretization. Thus, one of the most important aspects in the meshing strategy is to inherit the deformed boundary from the old mesh and then discretize the boundary according to the desired mesh density field.

Firstly, the boundary of the deformed body is extracted from the old mesh. Note that an interior element edge is shared by two elements while a boundary element edge only belongs to one element. Hence, the boundary segments are identified by analyzing the element connectivity of the old mesh. Subsequently, the boundary is formed by connecting the boundary segments counterclockwise.

Secondly, based on the desired mesh density field, which is usually derived from the discretization error in the finite element solution, the boundary is coarsened or refined by merging or splitting the boundary segments. Various criteria are considered to coarsen or refine the boundary.

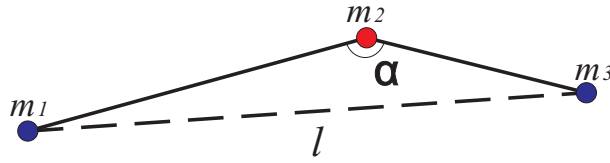


Figure 2.1: Merging of two neighboring boundary segments. Here, an angle criterion is applied.

Since boundary coarsening could lead to volume change if the two boundary segments to be merged are not collinear (see Figure 2.1), an angle criterion is used to restrict the volume change, which is defined as

$$|180^\circ - \alpha| < \alpha_{tol}, \quad (2.1)$$

where the limit α_{tol} is taken as, e.g., 5° . It is well known that transition elements are required



Figure 2.2: Ratio of boundary segment to its neighboring segments has to be checked, before merging.

for mesh transition from large elements to small elements. The quality of the transition element is affected by the gradient of the mesh size. To reduce mesh distortion, a ratio criteria is utilized in this work:

$$\max\left\{\frac{l}{l_1}, \frac{l}{l_2}\right\} < r_{lim}, \quad (2.2)$$

where l is the length of the segment resulting from the merging operation as shown in Figure 2.2, l_1 and l_2 are the lengths of its neighboring boundary segments and r_{lim} is the limit of the ratio, which is taken as 3 in the current work. If both, the angle criterion and the ratio criterion are satisfied, and the nodal desired mesh sizes m_i at the three nodes are all greater than the length l as shown in Figure 2.1, the two boundary segments are merged by eliminating their common node.

When the length of the current boundary segment is greater than the desired mesh size, new nodes need to be placed at appropriate positions on the old boundary segment. Given the nodal mesh sizes, various nodal spacing functions (*e.g.*, Frey, 1987; Prasad et al., 1994; Prasad and Rajagopal, 1997; Secchi and Simoni, 2003; Talbert, 1990; Zhu et al., 1991) are available to guide the node placement.

Firstly, we determine the number of new nodes which are required to be placed on the old boundary segment by computing

$$n = \text{integer}\left(\frac{2l}{m_1 + m_2} - 0.5\right), \quad (2.3)$$

where l is the length of the initial boundary segment, m_1 and m_2 are nodal mesh size parameters at the ends of the initial boundary segment and n is the number of new nodes to be added to the initial boundary segment.

Using the linear “ideal” nodal spacing function proposed by Talbert (1990), the length of the i^{th} ideal new segment, which is divided from the initial segment, is calculated by the following equation:

$$l_i^* = m_1 + (i - 1) * d, \quad (2.4)$$

where

$$d = \frac{m_2 - m_1}{n}. \quad (2.5)$$

Since the total ideal length $\sum_{i=1}^{n+1} l_i^*$ rarely equals the actual length of the initial segment l , each ideal segment is multiplied by a correction factor, which is the ratio of the actual length l to the ideal length l^* . The actual length of the i^{th} new segment is expressed as

$$l_i = (a + (i - 1) * d) * l/l^*. \quad (2.6)$$

The node placement procedure is illustrated with an example shown in Figure 2.3. Given the nodal mesh size and the length of the initial boundary segment, three new nodes are added to the initial boundary segment. The error between the ideal length and the actual length is corrected by the correction factor 10/9.

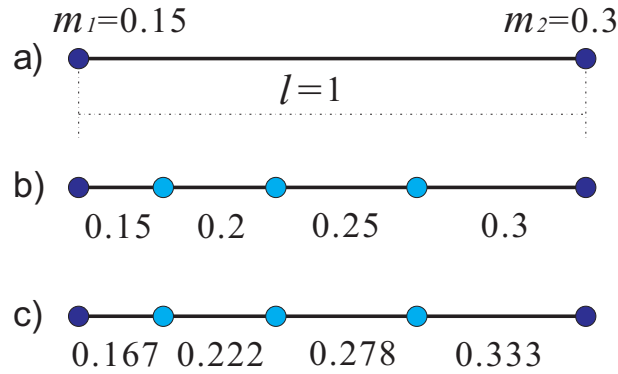


Figure 2.3: Example of node placement. a) Initial boundary segment; b) Three new nodes added using ideal spacing; c) Adjustment using correction factor.

2.3 Hierarchical mesh generation

The “Quadtree technique” was originally developed in computer graphics, then it was extended to mesh generation in finite element analysis by Yerry and Shephard (1983). Compared to conforming mesh generation, quadtree based hierarchical mesh generation is faster and easier to implement. Hence, it is widely used in mathematics and engineering applications (*e.g.*, Baeker et al., 2002; Carey et al., 1988; Fischer and Bar-Yoseph, 2000; Fish and Markolefas, 1994; Greaves and Borthwick, 1999; Hyun and Lindgren, 2001; Mcdill et al., 1987; Oden et al., 1986; Oh and Lim, 1997; Patra and Gupta, 2001; Petersen et al., 2000; Solin et al., 2008; Subbaraj and Dokainish, 1988; Tabarraei and Sukumar, 2005; Tang and Sato, 2004; Yue and Jr, 2005). It is also implemented in commercial software LS-DYNA, in which only subdivision of elements is available (Mathisen et al., 1999). In this work, a hanging-node-based hierarchical mesh generation technique, including both, refinement and coarsening is developed and implemented in VisualC++.

In hanging-node-based mesh generation, quadtree data structures play an important role, especially due to the complexity of the data structure in hierarchical meshes. The quadtree data structure is needed to handle the changing of the element connectivity, the nodal coordinates and the number of nodes and elements. The additional required data, such as the refinement level and the parent and children of the considered element, needs to be stored in the quadtree data structure (see Figure 2.4). In a quadtree data structure, the initial element is called root element. This element can be subdivided into four new elements, each new element can be subdivided recursively until the desired mesh density is reached. The new elements are called children of the subdivided (parent) element. The level of an element is the number of subdivisions, needed to obtain the element. The level of the root element is zero. After each refinement, if the new element and its neighboring elements are in different levels, hanging nodes need to be generated on their jointed face to handle the mesh transition. To ensure consistency of displacement, we impose constraint equations on the hanging nodes.

In order to obtain the smooth gradation of the refined mesh, additional elements are generated so that the number of hanging nodes on an element edge doesn’t exceed two. The algorithm is thus called 2 : 1 rule. Based on a hierarchical data structure, mesh coarsening can easily be

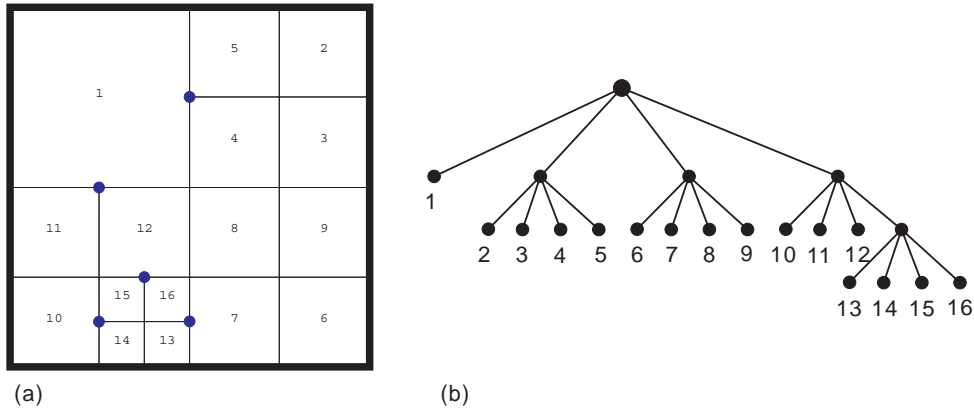


Figure 2.4: Quadtree data structure: (a) quadtree grid; (b) tree representation.

realized by removing the children elements and retrieving their parent element.

In this work, two approaches are available to guide mesh refinement. Element selection is a direct and simple approach to identify the elements to be splitted. The selected elements and refinement levels are predefined, the selected elements are splitted recursively until the refinement level is achieved. An example of this approach is presented in Figure 2.5.

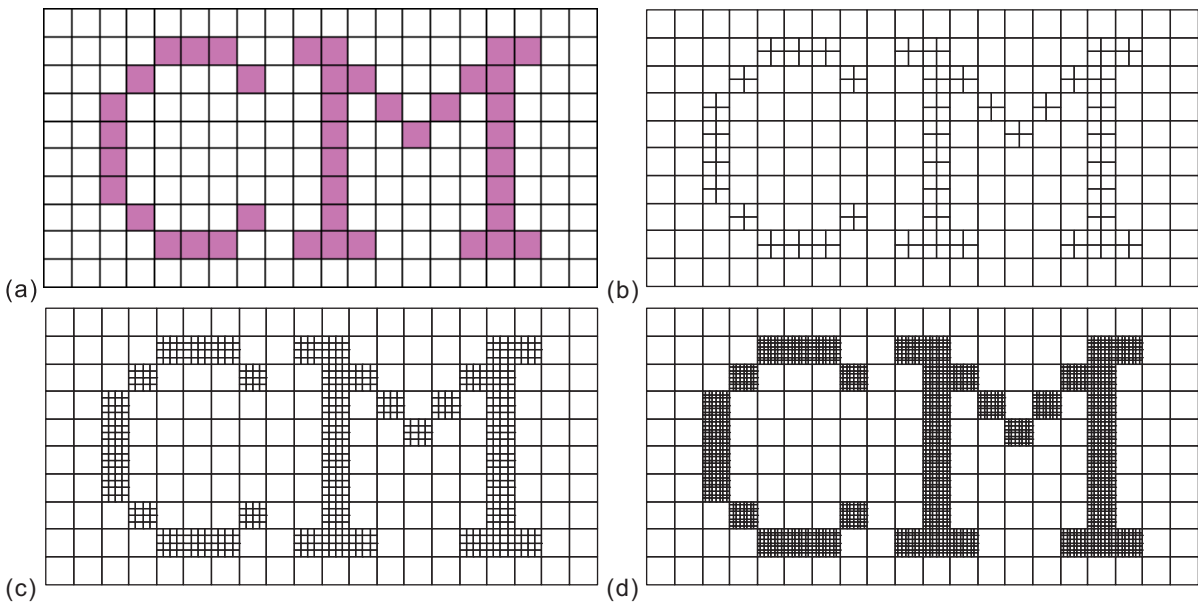


Figure 2.5: Hierarchical mesh refinement based on element selection. (a) Level 0 mesh with selected elements (231 nodes, 200 elements); (b) Level 1 (403 nodes, 106 hanging nodes, 323 elements); (c) Level 2 (1005 nodes, 318 hanging nodes, 815 elements); (d) Level 3 (3185 nodes, 742 hanging nodes, 2783 elements).

Alternatively, a refinement criterion is used if a mesh density field is given for adaptive mesh refinement, which is expressed as

$$\varpi = \frac{h_d}{h_c}, \tag{2.7}$$

where h_d is the desired element size and h_c is the current element size. The current element

is split if ϖ is less than a threshold value, which could be chosen as, *e.g.*, 0.75. Figure 2.6 shows an example of adaptive mesh refinement based on a mesh density field. In practice, with the help of a background mesh and nodal mesh size parameters, the mesh density field is obtained by using a standard interpolating function.

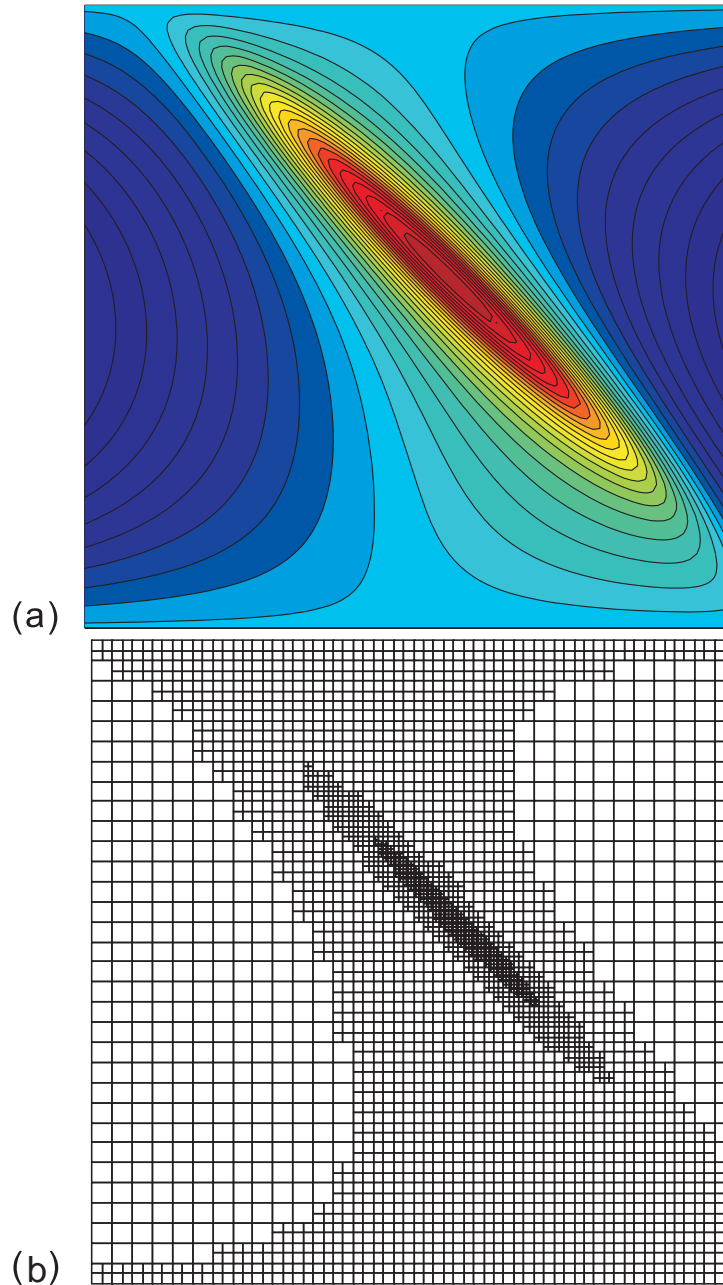


Figure 2.6: Hierarchical mesh refinement based on a mesh density field. (a) Mesh density field; (b) Refined mesh.

2.4 Examples

In this section, three examples of application of the developed mesh generation scheme on adaptive metal forming simulations are presented. The first example is the adaptive remeshing

in gear ring forging simulation. Figure 2.7 shows the procedure of automatic remeshing with boundary control. There are 180 elements and 217 nodes in the old mesh. The boundary is retrieved by extracting the 72 boundary nodes from the old mesh. On the basis of the mesh density field evaluated with the discretization error in the finite element solution, new boundary nodes are added into the upper-right part where the error is high and several boundary nodes, located at the lower part where the error is low are removed. The modified boundary consists of 70 boundary nodes. On this basis, 201 elements and 237 nodes are generated. In contrast to the old uniform mesh, the new adapted mesh is graded, which aims to reduce the discretization error.

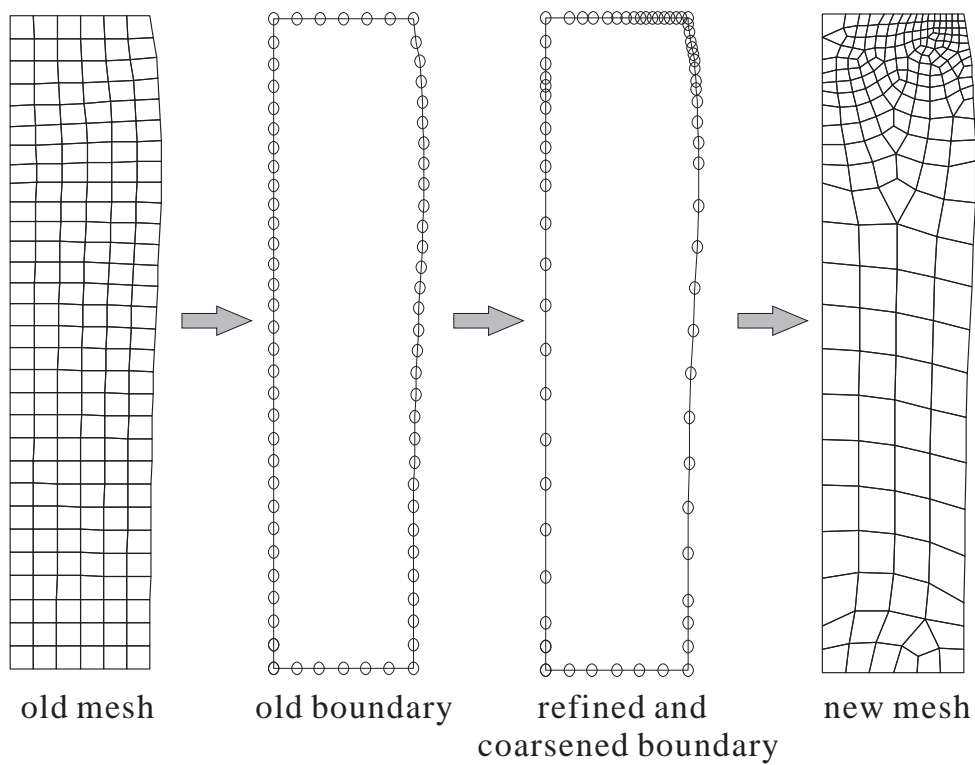


Figure 2.7: Remeshing in gear forging simulation.

Figure 2.8 illustrates an example of remeshing in forward extrusion simulation. There are 6446 elements and 6338 nodes in the old mesh. After remeshing, it can be observed that more elements are generated in the lower part where the material undergoes large deformation. Finally, the new mesh consists of 7009 elements and 7209 nodes.

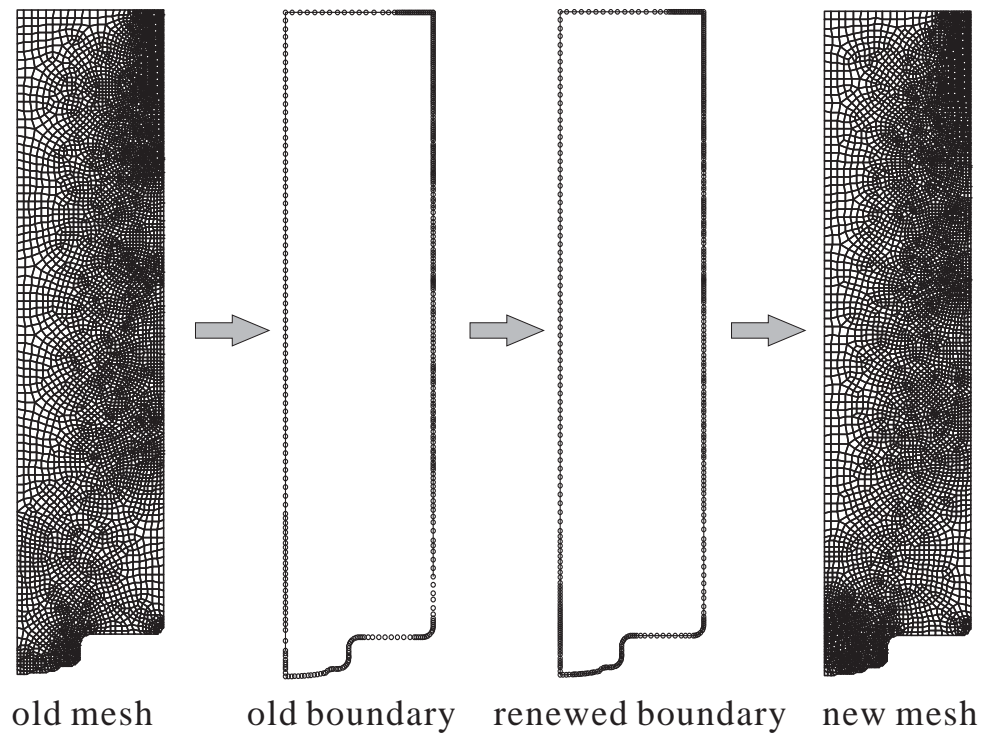


Figure 2.8: Remeshing in forward extrusion simulation.

The last example of remeshing in adaptive cutting simulation is presented to demonstrate the performance of the combined unstructured and hanging-node-based remeshing strategy. Figure 2.9 shows the procedure of the combined remeshing strategy. Based on the boundary segments, which are extracted and modified by the means, discussed in Section 2.2.2, the advancing front approach is first employed to generate the unstructured mesh. After that, hanging nodes are utilized to refine the mesh in the region of shear bands. There are 1044 elements and 1171 nodes in the mesh generated with the advancing front approach. The final mesh refined with hanging nodes consists of 6969 elements, 7533 nodes and 847 hanging nodes, which demonstrates the efficiency of hanging-node-based mesh refinement.

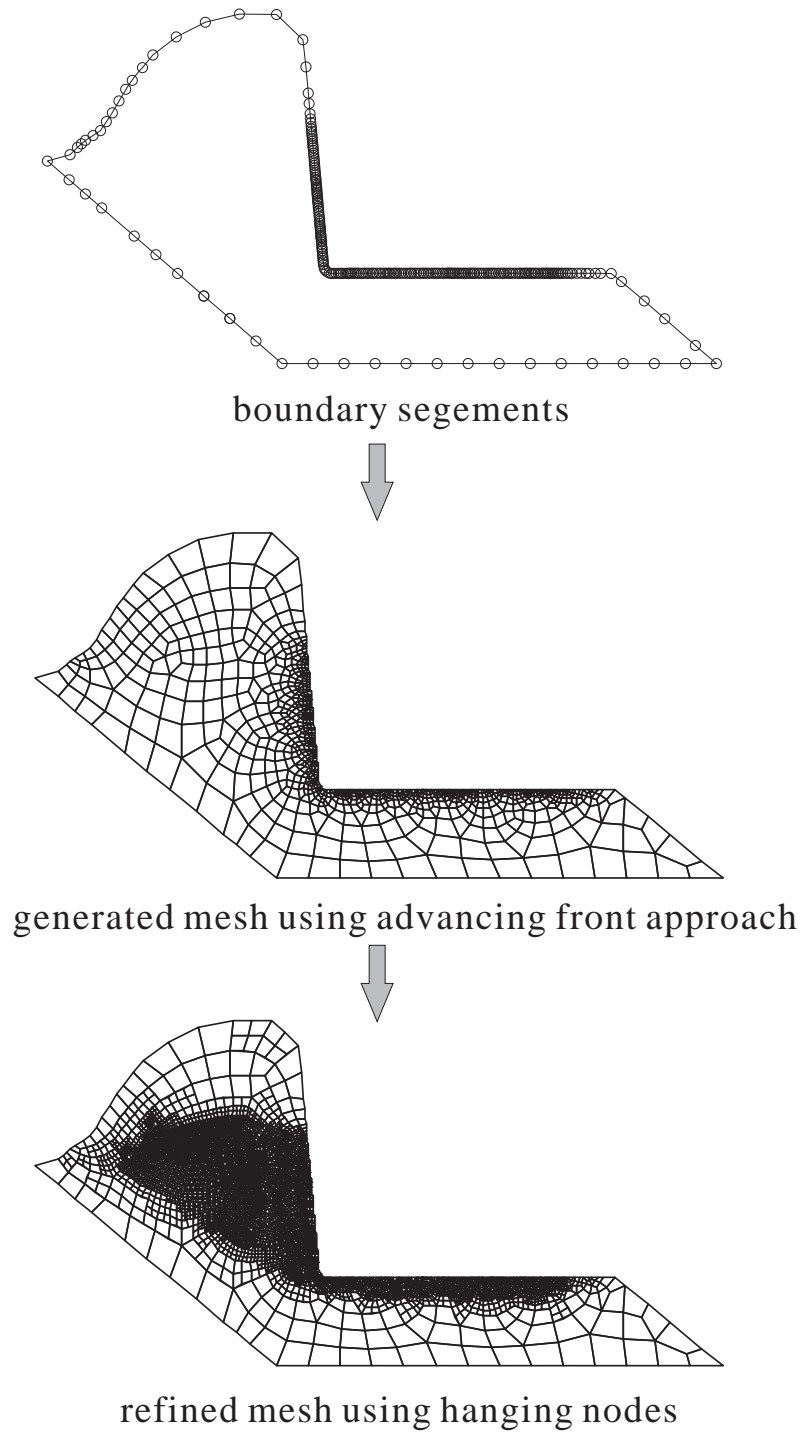


Figure 2.9: Remeshing in cutting simulation.

Chapter 3

Optimization based mesh smoothing for planar meshes

Abstract – In metal forming simulation, the mesh which represents the workpiece often undergoes large deformations, which could result in large discretization errors, numerical difficulties and even failure in the simulation. Mesh smoothing techniques such as Laplacian smoothing have been shown to be effective in improving geometrical mesh quality. However, when a badly shaped mesh contains invalid elements, most existing methods are not able to optimize such a mesh. Recently, an untangling technique was proposed by Freitag and Plassmann (2000). Based on this method, a new objective function is presented in this work, which can be used to carry out mesh optimization for an invalid mesh. The corresponding optimization problem is solved with the help of the steepest descent method. The method can be used together with any type of mesh refinement approach, e.g., hanging nodes. Numerical examples using the current approach demonstrating its robustness and effectiveness will be presented and discussed.

Keywords: mesh optimization, objective function, mesh quality, untangling, smoothing, steepest descent method.

3.1 Introduction

The finite element method is widely used in engineering applications. Unlike other mathematical modelling tools, such as meshless methods, the basic idea of the finite element method is to decompose the computational domain into a mesh, constructed by finite elements. Thus, the mesh plays an important role in finite element analysis. A low quality mesh, which contains poorly shaped or invalid elements, may lead to inaccurate solutions and even to failure.

In the past 30 years, much research work has been done on the issue of improving mesh quality. Mesh smoothing is the most commonly used technique, which repositions nodes, to improve the mesh quality without changing the topology. It is widely used as, e.g., the so-called ALE remeshing in ALE formulations (*e.g.*, Giuliani, 1982; Lohner and Yang, 1996; Sarrate and Hueta, 2001). In addition, mesh smoothing is also an important factor in a mesh generation procedure, since the mesh generated by a mesh generation technique is, in general, not optimal.

A very popular mesh smoothing technique is Laplacian smoothing (Field, 1988; Herrmann and ASCE, 1976), which relocates the interior nodes by solving a Laplacian equation. The method is simple to implement and computationally inexpensive, but it has the drawback, that it does not guarantee improvement of mesh quality. Actually, the nodes may run out of the domain near concavities (Hyun and Lindgren, 2001). A “smart” Laplacian smoothing, proposed by Lee and Lo (1994), can avoid the formation of lower quality elements, but still doesn’t guarantee the placement of the nodes at their optimal position. Similarly, there exist many other heuristic mesh smoothing methods, such as the weighted volume method (Jones, 1974), the

equipotential method (Brackbill and Saltzman, 1982), the iso-parametric method (Herrmann and ASCE, 1976) and the diamond smoothing method (Borouchaki and Frey, 1998), which move the nodes without any guarantee on improvement of mesh quality.

Actually, a new type of smoothing technique, based on the optimization of a mesh quality measure has been presented and is proven to be robust and effective. Using this smoothing techniques, the nodes are moved by optimizing an objective function, constructed with some measure of the geometric mesh quality. Various element quality measures have been used in optimization based mesh smoothing and evaluation of mesh quality, such as extreme angle, edge ratio and distortion metric (*e.g.*, Aiffa and Flaherty, 2003; Amenta et al., 1999; Bank and Smith, 1997; Calvo and Idelsohn, 2001; Chen et al., 2003; Freitag and Knupp, 2002; Joun and Lee, 1997; Knupp, 2000a,b,c, 2001, 2003a,b; Oddy et al., 1988; Pebay, 2004; Pebay and Baker, 2003; Riccius et al., 1997; Robinson, 1987). The optimization-based mesh smoothing techniques can be classified into two categories: Global and local mesh smoothing. In global mesh smoothing, all node locations are renewed simultaneously. In contrast, local smoothing moves the nodes in a sweep way recursively. Canann et al. (1993) proposed a global optimization method based on Oddy's distortion metric (Oddy et al., 1988). Balendran (1999) developed a method similar to the finite element analysis, using the global geometrical stiffness matrix, which was improved and extended by Diaz et al. (2004, 2005). The disadvantage of global smoothing is its high cost of memory and CPU time, so local mesh smoothing is more commonly used in practice (*e.g.*, Aiffa and Flaherty, 2003; Bottasso, 2004; Freitag, 1995; Garimella et al., 2004; Xu and Newman, 2006).

In general, there is a limitation in most existing smoothing algorithms. That is, the mesh to be smoothed must not have invalid elements. For invalid meshes, some two-stage schemes have been introduced to untangle the invalid mesh first and then smooth the untangled mesh. Li et al. (2000) proposed a procedure to repair invalid elements:

1. disconnect the invalid element from the remaining mesh,
2. reshape the invalid element,
3. assemble the repaired elements with the mesh.

A more simple and convenient optimization-based untangling approach was proposed to untangle the invalid mesh by Freitag and Plassmann (2000). After untangling, the mesh is not optimal since these two untangling schemes are not designed to optimize the mesh quality, and thus a subsequent smoothing scheme should be performed to achieve an optimal mesh.

In this chapter, we propose a new mesh optimization scheme, which performs mesh untangling and smoothing simultaneously. In Section 3.2, we review the mesh quality measure and discuss the corresponding objective function. We develop the new objective function in Section 3.3. An alternative objective function is discussed in Section 3.4. In Section 3.5, a combined Laplacian- and optimization-based smoothing scheme is discussed and extended to non-conforming meshes. The mesh optimization algorithm is given in Section 3.6. The numerical results are presented to demonstrate the performance of the new scheme in Section 3.7. In Section 3.8 we present some conclusions.

3.2 Mesh quality measures and objective function

3.2.1 Mesh quality measures

Mesh quality measures are the basis when evaluating the mesh quality. Among many measures, the one for triangles introduced by Bank and Smith (1997) can be computed efficiently and proven to be effective in mesh optimization (Canann et al., 1998). Later, a measure was derived based on the condition number of a Jacobian matrix, which expresses the linear transformation between the ideal reference element and the physical element (Knupp, 2001; Pebay, 2004; Pebay and Baker, 2003). In this section, we review the mesh quality measures for triangles and quadrilaterals.

Triangular quality measure

Figure 3.1 shows the transformation between the reference triangle and the physical triangle. The reference triangle is an equilateral triangle which is ideal to predict the finite element solution for most problems. The physical triangle is the real element inside a mesh. The coordinates of its three nodes are labelled as (x_k, y_k) , with $k = 0, 1, 2$. The edge matrix of the physical tri-

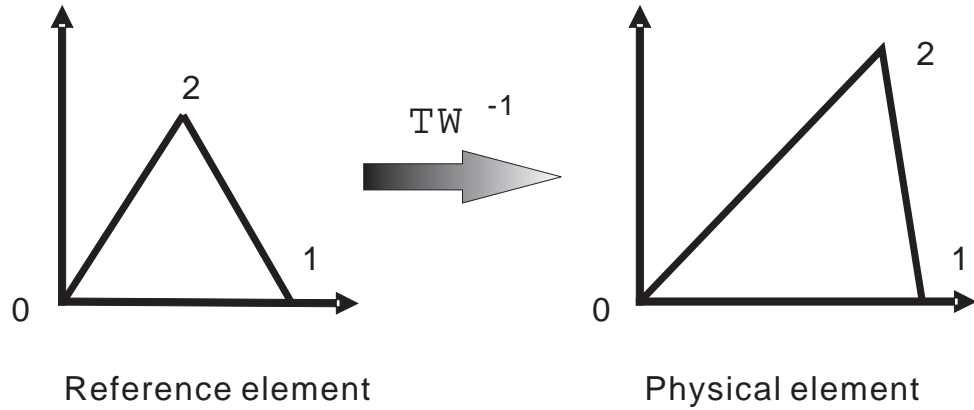


Figure 3.1: Transformation between the ideal equilateral triangle and the physical triangle.

angle is defined by

$$T = \begin{pmatrix} x_1 - x_0 & x_2 - x_0 \\ y_1 - y_0 & y_2 - y_0 \end{pmatrix}. \quad (3.1)$$

Let W be the edge matrix of an equilateral triangle, whose nodes are, for example, located at $(0, 0)$, $(1, 0)$, and $(\frac{1}{2}, \frac{\sqrt{3}}{2})$ so that W is expressed as

$$W = \begin{pmatrix} 1 & \frac{1}{2} \\ 0 & \frac{\sqrt{3}}{2} \end{pmatrix}. \quad (3.2)$$

Now the Jacobian matrix which maps the reference element to the physical element can be expressed as

$$S = TW^{-1}. \quad (3.3)$$

As described by Knupp (2001), the mesh quality measure is defined based on the condition number of S . In our work, the Frobenius norm is chosen for its definition. Here, the condition number of S can be expressed as

$$\kappa(S) = \|S^{-1}\| \|S\|, \quad (3.4)$$

where

$$\|S\| = \sqrt{\text{tr}(S^T S)}. \quad (3.5)$$

Although $\kappa(S)$ is continuous in the half space where the triangle is valid, it becomes discontinuous when the triangle goes inverted due to the infinite value of quality. For this reason, we take the inverse of the condition number and normalize it to obtain

$$q = \frac{2}{\|S^{-1}\| \|S\|}. \quad (3.6)$$

Note that q is a positive value even for an inverted element. An indicator for the validity of an element is defined by

$$\sigma = \frac{1}{2} \det(T), \quad (3.7)$$

which is the area of an element when the element is valid. The level sets of σ for a triangle with one adjustable node is illustrated in Figure 3.2, the other two nodes are fixed at $(-0.5, 0)$ and $(0.5, 0)$. Note that σ becomes negative when the element inverts. Hence it represents a reasonable indicator for the element direction. On this basis, a quality measure which can

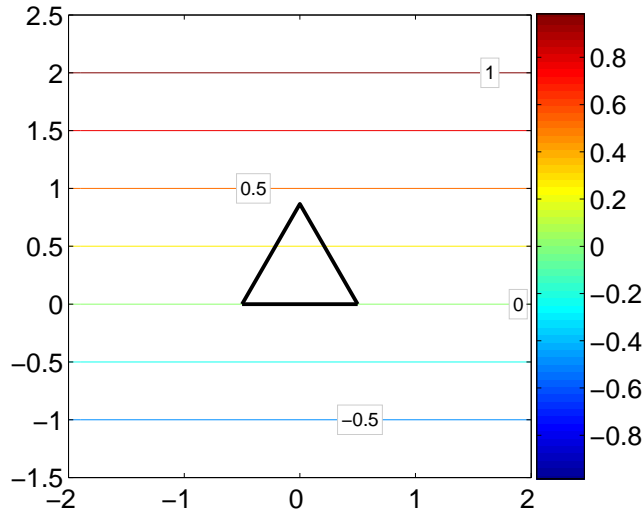


Figure 3.2: Level sets of σ for a triangle.

detect the validity of an element is defined as

$$q^e = \frac{2\sigma}{\|S^{-1}\| \|\Sigma\|}, \quad (3.8)$$

where Σ is the adjoint matrix of S :

$$\Sigma = \sigma S. \quad (3.9)$$

The quality measure q^e can be expressed in another form (Bank and Smith, 1997)

$$q^e = \frac{4\sqrt{3}\sigma}{|l_{0,1}|^2 + |l_{1,2}|^2 + |l_{2,0}|^2}, \quad (3.10)$$

where $l_{0,1}$, $l_{1,2}$ and $l_{2,0}$ are the edge lengths of the triangle, respectively. Figure 3.3 shows the level sets of q^e . It can be seen that the mesh quality ranges from -1 to 1 . The optimal quality 1 is achieved only when the adjustable node lies at $(0, \frac{\sqrt{3}}{2})$, which makes the triangle equilateral.

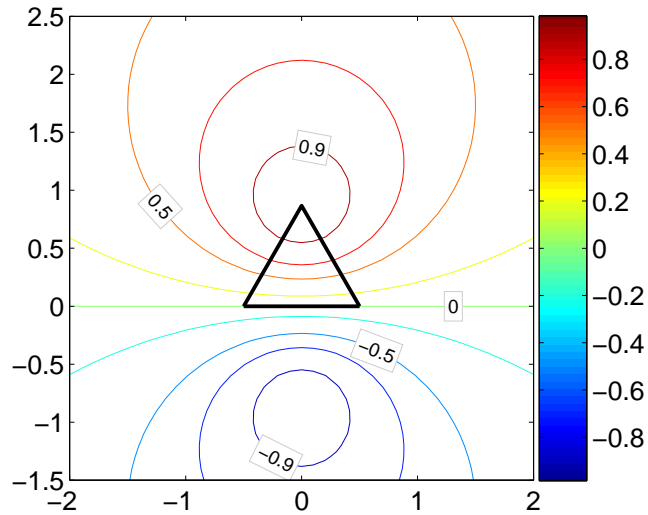


Figure 3.3: Level sets of q^e for a triangle.

Quadrilateral quality measure

The quality measure for quadrilaterals is derived with the help of sub-triangles of the quadrilateral element. Consider a quadrilateral element Q with its four nodes and their coordinates labelled as N_k , \mathbf{x}_k , $k = 1, 2, 3, 4$, respectively (see Figure 3.4). The quadrilateral Q can be decomposed into four triangular elements T_k , each consisting of three nodes N_k , N_{k+1} and N_{k+3} , where the indices are taken modulo 4. We note that the square shape of quadrilateral element is

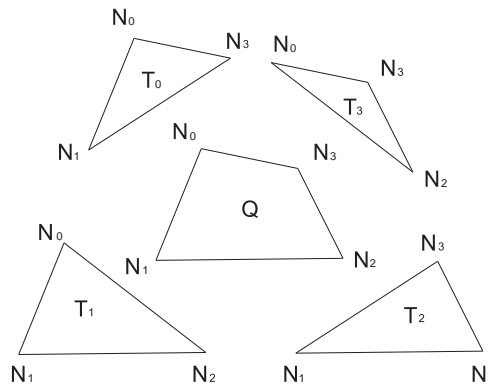


Figure 3.4: A quadrilateral, decomposed into four sub-triangles.

achieved when all these four sub-triangles are right isosceles triangles. Analogous to the quality measure for equilateral triangle, the quality measure for a right isosceles triangle can also be constructed by means of the condition number of transformation matrix.

The relationship between the reference triangle and the physical triangle is illustrated in Figure 3.5. Let W be the edge matrix of a right isosceles triangle, whose nodes are, for example, located at $(0, 0)$, $(1, 0)$, and $(0, 1)$ so that W is expressed as

$$W = \begin{pmatrix} 1 & 0 \\ 0 & 1 \end{pmatrix}. \quad (3.11)$$

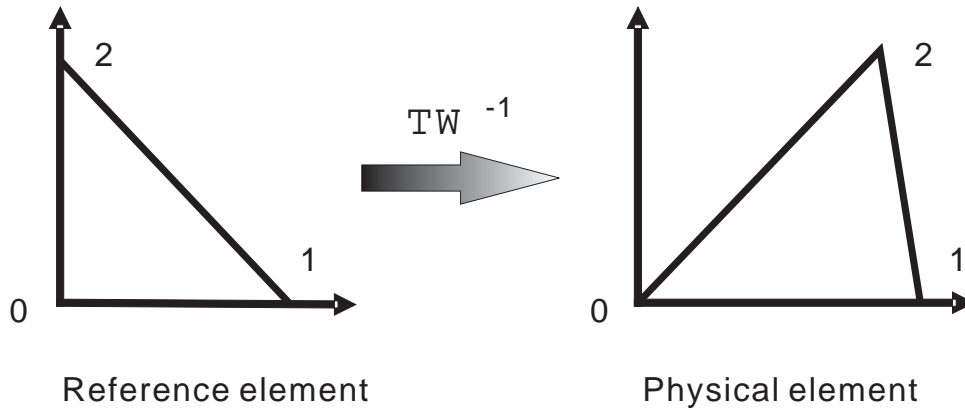


Figure 3.5: Transformation between the ideal right isosceles triangle and the physical triangle.

Considering again the condition number of S and σ , the quality measure is defined by the same form

$$q^r = \frac{2\sigma}{\|S^{-1}\| \|\Sigma\|}, \quad (3.12)$$

which can also be written as (Pebay, 2004)

$$q^r = \frac{4\sigma}{|l_{0,1}|^2 + |l_{2,0}|^2}. \quad (3.13)$$

Here,

$$l_{k,k+n} = (\mathbf{x}_{k+n} - \mathbf{x}_k) \quad (3.14)$$

are the corresponding edge vectors of the subelements.

Figure 3.6 shows the level sets of q^r for a triangle with one adjustable node, the other two nodes are fixed at $(0, 0)$ and $(1, 0)$. This figure shows that the mesh quality ranges from -1 to 1 . The maximum value of q^r is achieved only if the triangle is a right isosceles triangle. Now

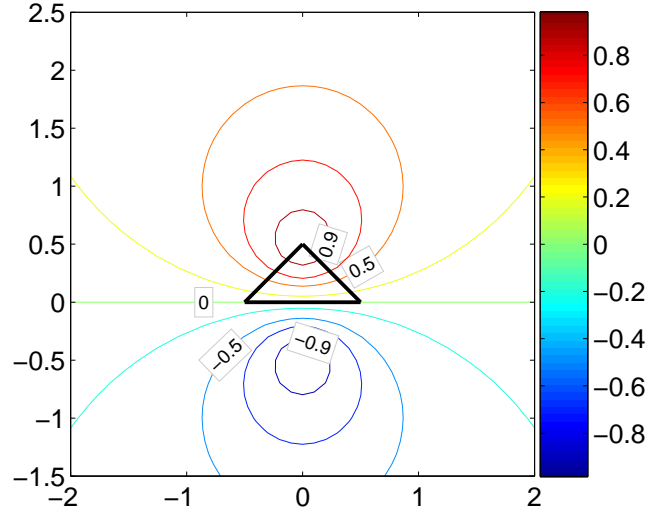


Figure 3.6: Level sets of q^r for triangle.

consider the sub-triangles in Figure 3.4. If vectors $l_{k,k+1}$ and $l_{k,k+3}$ are defined by

$$l_{k,k+1} = (\mathbf{x}_{k+1} - \mathbf{x}_k) \quad (3.15)$$

and

$$l_{k,k+3} = (\mathbf{x}_{k+3} - \mathbf{x}_k) . \quad (3.16)$$

The quality measure for each subtriangle is

$$q_k^r = \frac{4\sigma_k}{|l_{k,k+1}|^2 + |l_{k,k+3}|^2} . \quad (3.17)$$

Since the quality for single sub-triangle doesn't indicate the quality of quadrilaterals directly, we choose the min norm of these four qualities

$$q_Q^{min} = \min(q_0^r, q_1^r, q_2^r, q_3^r) \quad (3.18)$$

to express the quality of quadrilateral elements. The quadrilateral is a square only if all the four qualities have a maximum value of one, in other words q_Q^{min} is equal to one. Figure 3.7 gives the contour plots showing the level sets of q_Q^{min} for a group of quadrilaterals in which the top node is adjustable and other nodes are fixed, respectively.

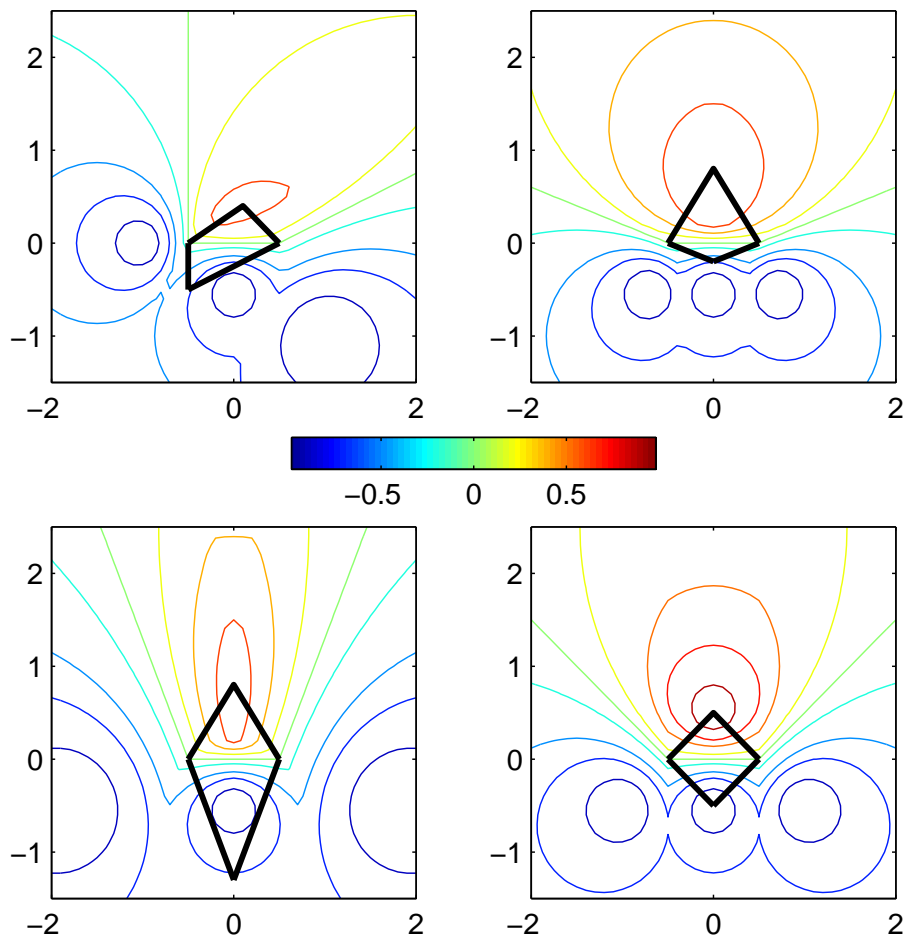


Figure 3.7: Level sets of q_Q^{min} for a group of quadrilaterals.

3.2.2 Objective function

Triangular meshes

Given the quality measure for triangular elements, we can derive the objective function for a triangular mesh. Consider a local sub-mesh, we formulate the composite objective function for local sub-mesh optimization. In each local sub-mesh optimization step, the considered node is set to be adjustable while other nodes are fixed. Let N_i be an adjustable node connected to its surrounding elements, which construct the local sub-mesh. The objective function for the single triangular element in the sub-mesh is derived from the quality measure. It is expressed as

$$\phi_j^T(\mathbf{x}) = q_j^e(\mathbf{x}), \quad (3.19)$$

where $\phi_j^T(\mathbf{x})$ is the objective function associated to the j^{th} element in the local sub-mesh. In order to move N_i so that the quality of the worst shaped element in the sub-mesh is increased as much as possible, we utilize the minimum value in the sub-mesh as objective function, which is expressed as

$$\Phi^T(\mathbf{x}) = \min_{1 \leq j \leq n} (\phi_j^T(\mathbf{x})), \quad (3.20)$$

where n is the total number of triangles in the local sub-mesh. To illustrate the level sets of this objective function, an example is given in Figure 3.8. The shaded region in Figure 3.8 is the feasible region, which is the set of possible locations of the adjustable node N_i so that all the elements connected to the node N_i in the sub-mesh are valid. Figure 3.9 illustrates the level sets. It can be observed that the level sets are non-convex if the adjustable node is placed outside the feasible region. Due to this fact, the gradient based optimization techniques such as the steepest descent method are not guaranteed to find the global maximum value if the starting adjustable node lies outside the feasible region.

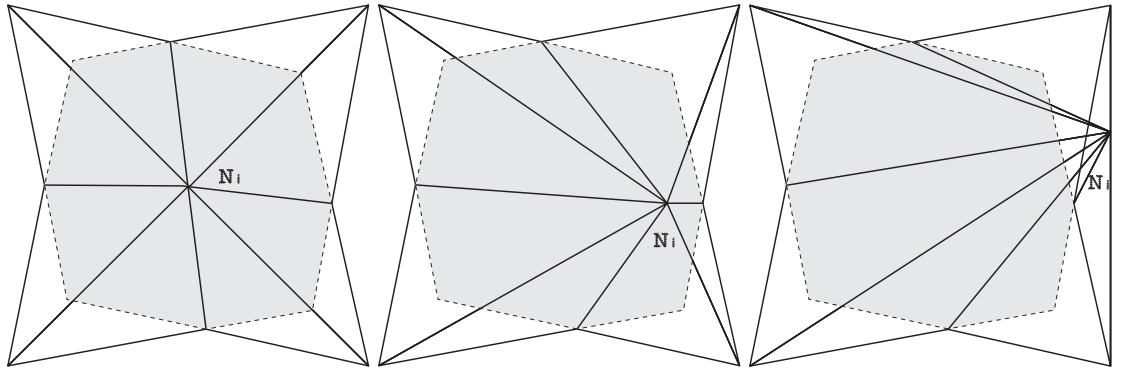


Figure 3.8: A sub-mesh with the adjustable node N_i . The shaded region is the feasible region. Left: high quality mesh; Middle: poor quality mesh; Right: invalid mesh.

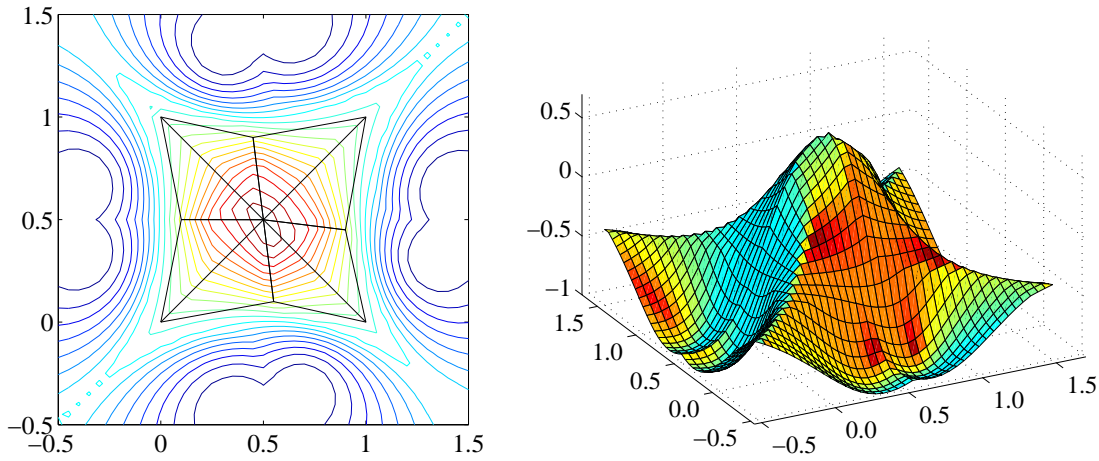


Figure 3.9: The level sets for the objective function $\Phi^T(\mathbf{x})$. Left: contour representation; Right: 3D representation.

Quadrilateral meshes

Taking into account the quadrilateral Q , we assume that N_i is the adjustable node while the other three nodes are fixed and \mathbf{x} is the position of N_i . Then the quality for the sub-triangle T_{i+2} is

$$q_{i+2}^r = \frac{4\sigma_{i+2}}{|l_{i+2,i+3}|^2 + |l_{i+2,i+1}|^2}. \quad (3.21)$$

Notice that \mathbf{x} is absent in this expression, in other words, the node N_i doesn't have an effect on the quality of the triangle T_{i+2} . Actually, the possible movement of N_i only affects three other triangles which are associated with N_i , so the objective function for quadrilateral element Q is formulated as

$$\phi^Q(\mathbf{x}) = \min(q_i^r(\mathbf{x}), q_{i+1}^r(\mathbf{x}), q_{i+3}^r(\mathbf{x})). \quad (3.22)$$

Now, we formulate the composite objective function for local sub-mesh optimization. In each local sub-mesh optimization step, the considered node is set to be adjustable while the other nodes are fixed. Let N_i be an adjustable node connected to its surrounding elements, which construct the local sub-mesh. In order to move N_i , so that the quality of the worst shaped element in the sub-mesh is increased as much as possible, the objective function for local sub-mesh is expressed as

$$\Phi^Q(\mathbf{x}) = \min_{1 \leq j \leq n} (\phi_j^Q(\mathbf{x})). \quad (3.23)$$

Combining Equations (3.22) and (3.23) yields the alternative form

$$\Phi^Q(\mathbf{x}) = \min_{1 \leq j \leq 3n} (q_j^r(\mathbf{x})), \quad (3.24)$$

where n is the number of quadrilaterals in the local sub-mesh, j is the global index of the sub-triangle associated with the adjustable node in the sub-mesh and $q_j^r(\mathbf{x})$ is the quality of the j th sub-triangle. Figure 3.10 shows an example of a sub-mesh and its feasible region. The level sets of the objective function are illustrated in Figure 3.11.

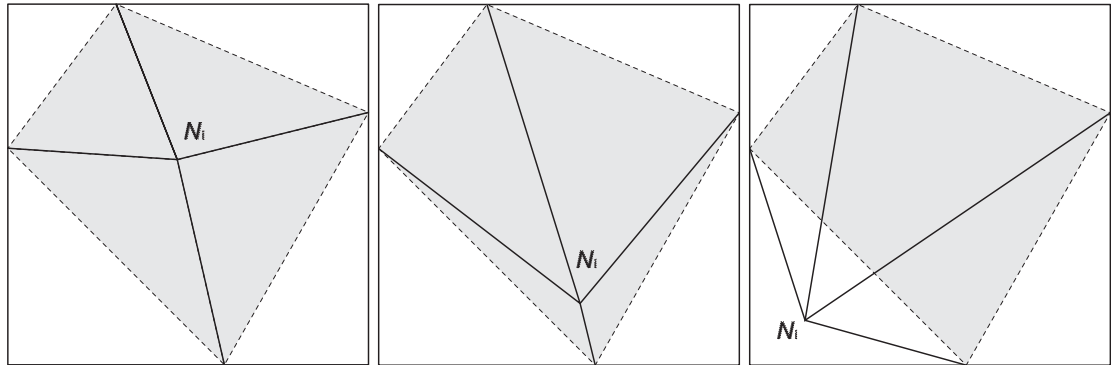


Figure 3.10: A sub-mesh with the adjustable node N_i . The shaded region is the feasible region. Left: high quality mesh; Middle: poor quality mesh; Right: invalid mesh.

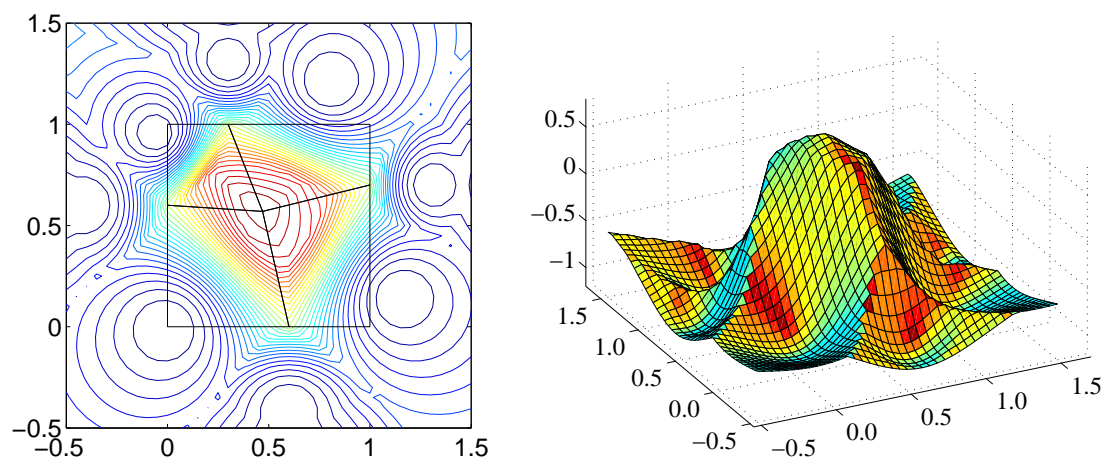


Figure 3.11: The level sets for the objective function $\Phi^Q(\mathbf{x})$. Left: contour representation; Right: 3D representation.

3.3 Modified objective functions

It is known that the level sets of the objective function must be convex over the entire domain if we take the objective function for both mesh untangling and smoothing. In this section, we propose modified objective functions by introducing σ in the original objective functions to satisfy the above condition.

3.3.1 Triangular meshes

For triangular meshes the new objective function is expressed as

$$\Theta^T(\mathbf{x}) = \min_{1 \leq j \leq m} \xi_j^T(\mathbf{x}), \quad (3.25)$$

with

$$\xi_j^T(\mathbf{x}) = \frac{|\sigma_j(\mathbf{x})| + |q_j^e(\mathbf{x})| - \sigma_j(\mathbf{x}) + q_j^e(\mathbf{x})}{2}. \quad (3.26)$$

The term $\sigma_j(\mathbf{x})$ in equation (3.26) was introduced by Freitag (2001) for untangling. The reason why we take the term $\sigma_j(\mathbf{x})$ into consideration is that the level sets of minimum $\sigma_j(\mathbf{x})$ are convex outside the feasible region. Note that $q_j^e(\mathbf{x})$ differs from $\sigma_j(\mathbf{x})$ by a positive coefficient in equation (3.10), so they have the same sign. Both of their minima are positive inside the feasible region and negative outside the feasible region, so $\Theta^T(\mathbf{x})$ takes the minimum of the term $q_j^e(\mathbf{x})$ inside the feasible region and the minimum of the term $\sigma_j(\mathbf{x})$ outside the feasible region, respectively. Since both, the minimum of $q_j^e(\mathbf{x})$ and the minimum of $\sigma_j(\mathbf{x})$ become zero on the boundary of the feasible region, $\Theta^T(\mathbf{x})$ is continuous over the boundary of the feasible region. Considering that the level sets of the minimum $q_j^e(\mathbf{x})$ inside of the feasible region and the level sets of the minimum $\sigma_j(\mathbf{x})$ outside of the feasible region are both convex, the level sets of the new objective function $\Theta^T(\mathbf{x})$ are convex in the entire domain.

The level sets for the function $\Theta^T(\mathbf{x})$ are shown in Figure 3.12. Since the level sets are convex, regardless of the location of the adjustable node, the objective function $\Theta^T(\mathbf{x})$ can be used to untangle and smooth a tangled mesh.

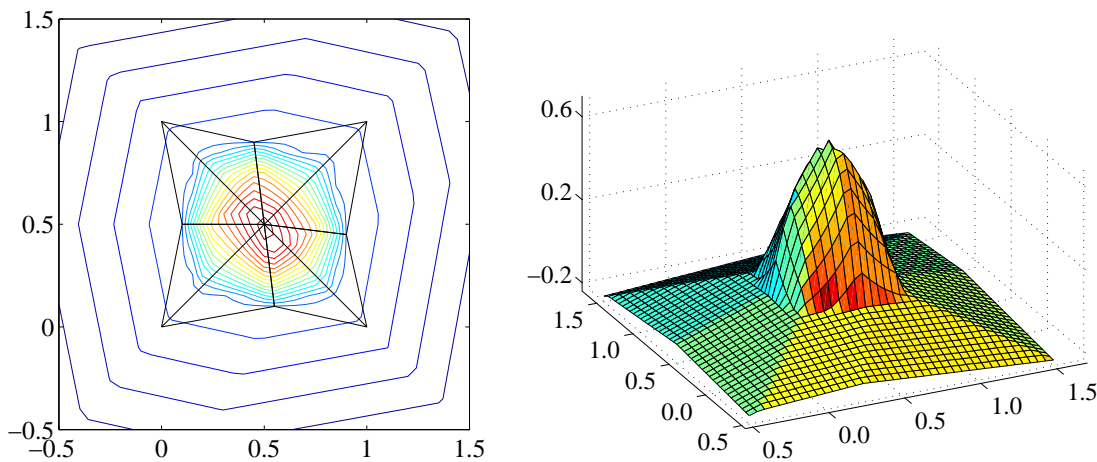


Figure 3.12: The level sets for the new objective function $\Theta^T(\mathbf{x})$. Left: contour representation; Right: 3D representation.

3.3.2 Quadrilateral meshes

Following the same procedure as described in Section 3.3.1, we obtain the modified objective function for quadrilateral meshes:

$$\Theta^Q(\mathbf{x}) = \min_{1 \leq j \leq 3n} \xi_j^Q(\mathbf{x}), \quad (3.27)$$

where

$$\xi_j^Q(\mathbf{x}) = \frac{|\sigma_j(\mathbf{x})| + |q_j^r(\mathbf{x})| - \sigma_j(\mathbf{x}) + q_j^r(\mathbf{x})}{2} \quad (3.28)$$

and n is the number of quadrilaterals in the local sub-mesh. As can be observed from Figure 3.13, the level sets of the function $\Theta^Q(\mathbf{x})$ is convex in the whole domain. The convexity of the level sets enable the ability of mesh untangling for quadrilateral meshes.

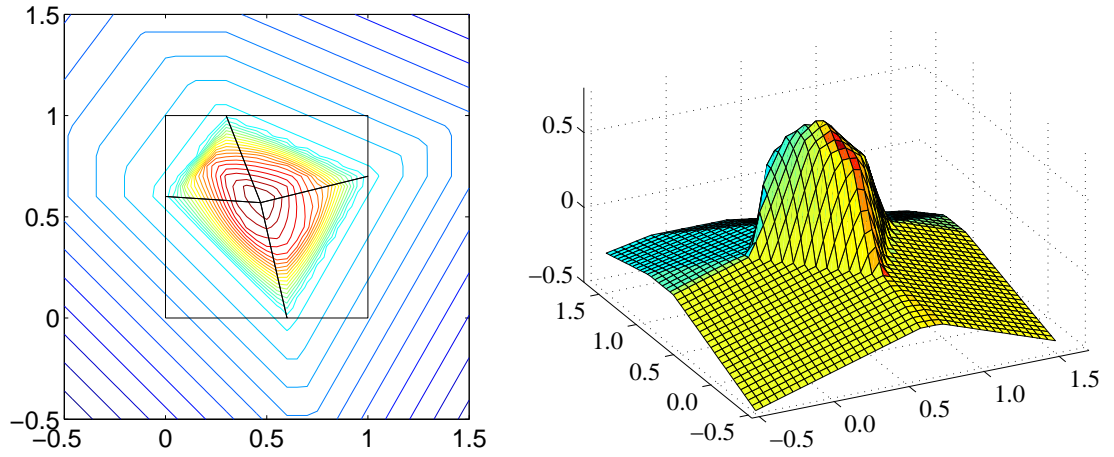


Figure 3.13: The level sets for the new objective function $\Theta^Q(\mathbf{x})$. Left: contour representation; Right: 3D representation.

3.3.3 Mixed meshes

To optimize a mixed triangular and quadrilateral mesh, the objective functions for these two different element types have to be normalized to work together, in other words, the objective functions should not over-emphasize any of the element types. Since $\xi_i^T(\mathbf{x})$ and $\xi_j^Q(\mathbf{x})$ are both normalized functions, the objective function for mixed meshes can be constructed by $\xi_i^T(\mathbf{x})$ and $\xi_j^Q(\mathbf{x})$

$$\Theta^M(\mathbf{x}) = \min_{1 \leq i \leq m, 1 \leq j \leq 3n,} (\xi_i^T(\mathbf{x}), \xi_j^Q(\mathbf{x})), \quad (3.29)$$

where m is the number of triangles and n is the number of quadrilaterals in the sub-mesh.

3.4 Alternative objective function

Alternatively, the objective function can be constructed with the help of an increasing function proposed by Escobar et al. (2005, 2006, 2003). Using the idea, the modified objective function is constructed by substituting σ with an increasing function $h(\sigma)$, which is expressed as

$$h(\sigma) = \frac{1}{2}(\sigma + \sqrt{\sigma^2 + \delta^2}), \quad (3.30)$$

where δ is a relatively small value compared to σ . Employing the inverted form of equation (3.8), the modified objective function for the j element is then written as

$$\eta_j(\mathbf{x}) = \frac{\|S^{-1}\|\|\Sigma\|}{\sigma + \sqrt{\sigma^2 + \delta^2}}. \quad (3.31)$$

Consequently, the corresponding objective function for local sub-mesh is defined as

$$\Gamma(\mathbf{x}) = \sum_{j=1}^m \eta_j(\mathbf{x}). \quad (3.32)$$

Note that the parameter δ in equation (3.31) affects the optimal solution while minimizing the objective function. Hence, during the optimization process, the parameter δ has to be set as zero once the local sub-mesh is untangled.

3.5 Combined Laplacian and optimization based smoothing for non-conforming mesh

Optimization based smoothing is effective and robust for mesh optimization, however, solving optimization problems can be time consuming. On the other hand, Laplacian smoothing is much faster since no optimization problem is involved in this technique, but it can not guarantee the improvement of the mesh quality. Therefore, the combination of Laplacian- and optimization-based smoothing can achieve a compromise between mesh quality and computational costs (Canann et al., 1998; Chen et al., 2003; Freitag, 1997). In this procedure, a threshold value is predefined. ‘‘Smart’’ Laplacian smoothing is performed in the first step. If the mesh quality of the smoothed mesh exceeds the threshold value, the smoothing procedure is terminated; otherwise, the optimization based smoothing is activated.

In the current work, hanging node based, hierarchical mesh refinement technique is incorporated with reference to adaptive remeshing. Hence, corresponding mesh smoothing techniques need to be developed. In this section, Laplacian smoothing and optimization based smoothing are modified and discussed, in particular for non-conforming meshes.

3.5.1 Modified Laplacian smoothing

The original Laplacian smoothing method (Herrmann and ASCE, 1976) repositions each node by averaging the coordinates of its neighboring nodes, which is connected to the considered node (see Figure 3.14):

$$\mathbf{x}_i = \frac{1}{n} \sum_{j=1}^n \mathbf{x}_j, \quad (3.33)$$

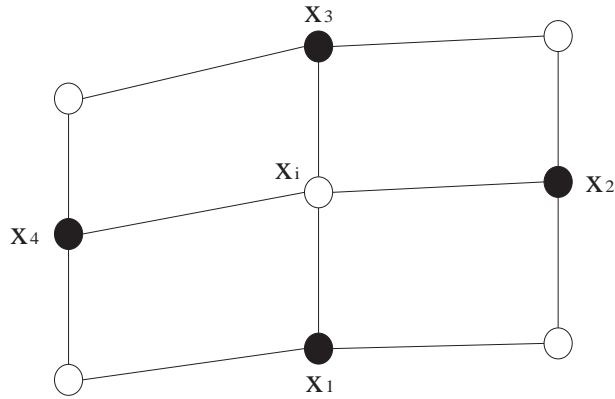


Figure 3.14: Original Laplacian smoothing.

where i ranges over all moveable nodes, j is the j th node connected to the considered node i and n is the total number of the neighboring nodes connected to the node i .

For non-conforming meshes, the original Laplacian smoothing can not be used directly, due to the constrained hanging nodes and the different refinement levels of the elements. In the modified Laplacian smoothing scheme for non-conforming meshes, the neighboring node is replaced with the midpoint on the edge if the edge belongs to an element in higher refinement levels (see Figure 3.15).

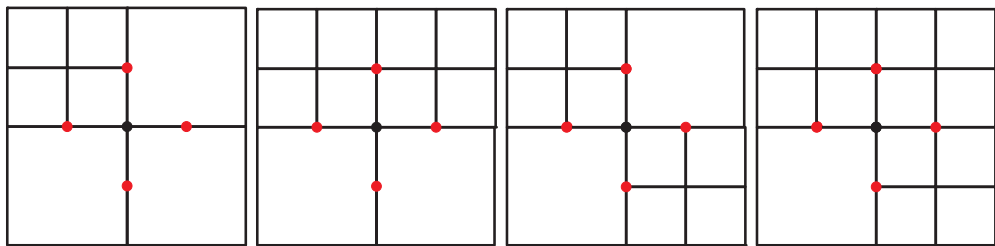


Figure 3.15: Modified Laplacian smoothing for the elements in different refinement levels.

3.5.2 Optimization based smoothing

The basic idea of the mesh optimization scheme is, to move the considered node so that the mesh quality is improved. In the case of non-conforming meshes, the construction of the sub-mesh is tricky since the degrees of freedom of the hanging nodes are not independent. The movement of the considered node has effect on some elements which are not connected to the considered node directly. Figure 3.16 shows the construction of the sub-mesh for possible mesh configurations.

3.6 Mesh optimization algorithm

The optimization approach is performed in an iterative Gauss-Seidel-like scheme by sweeping over all the adjustable nodes iteratively until convergence is achieved. In each step, only one node is adjustable while the other nodes are fixed. The local optimization approach finds the position \mathbf{x}^* by maximizing the new objective function $\Theta(\mathbf{x})$, which is a continuous and

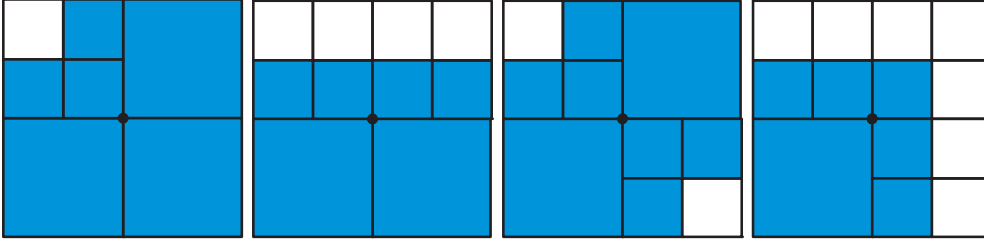


Figure 3.16: Optimization based smoothing for the elements in different refinement levels. The elements, affected by the movement of the corresponding point are marked.

non-smooth composite function or minimizing the objective function $\Gamma(\mathbf{x})$ which is a smooth function. The steepest descent method and the conjugate gradient method are employed to solve the optimization problems based on the objective functions $\Theta(\mathbf{x})$ and $\Gamma(\mathbf{x})$, respectively.

3.6.1 The steepest descent method

The steepest descent method is used to solve the non-smooth optimization problem. Firstly, the gradients $\mathbf{g}_j(\mathbf{x})$ are calculated for each sub-triangle associated with the adjustable node. Note that $\xi_j(\mathbf{x})$ is not differentiable when $\xi_j(\mathbf{x}) = 0$. In this case, the gradients of $q_j(\mathbf{x})$ are taken as the pseudo-gradients.

When the adjustable node lies on the smooth surface, the search direction \mathbf{g} is computed by

$$\mathbf{g} = \frac{1}{2} \left(\frac{\mathbf{g}_a(\mathbf{x})}{\|\mathbf{g}_a(\mathbf{x})\|} + \frac{\mathbf{g}_b(\mathbf{x})}{\|\mathbf{g}_b(\mathbf{x})\|} \right), \quad (3.34)$$

where the indices a and b indicate the two lowest quality elements in the sub-mesh. If the adjustable node lies on non-smooth manifold, the search direction \mathbf{g} is determined by finding the shortest vector inside the *Convex Hull* ($\mathbf{g}_k(\mathbf{x})$), where $\mathbf{g}_k(\mathbf{x})$ are the possible gradients around the node (Burke et al., 2005; Freitag and Plassmann, 2000).

Secondly, the step length γ is determined by predicting the position at which the worst quality element will change (Canann et al., 1998), in other words, the worst quality element should be still the worst one after the movement of the adjustable node, which can be described by

$$\xi_{min}(\mathbf{x}^+) \leq \xi_j(\mathbf{x}^+). \quad (3.35)$$

With the help of the first order Taylor series approximation for the function associated with each element

$$\xi_j(\mathbf{x}^+) = \xi_j(\mathbf{x} + \gamma\mathbf{g}) \approx \xi_j(\mathbf{x}) + \gamma\mathbf{g} \cdot \mathbf{g}_j, \quad (3.36)$$

the step length is limited by

$$\gamma \leq \frac{\xi_j(\mathbf{x}) - \xi_{min}(\mathbf{x})}{(\mathbf{g} \cdot \mathbf{g} - \mathbf{g} \cdot \mathbf{g}_j)}. \quad (3.37)$$

Using the constraint condition, the upper limit of γ is taken as the initial step length. If the initial step length is not accepted, then it is halved recursively until a step length is accepted.

3.6.2 The conjugate gradient method

Since the objective function $\Gamma(\mathbf{x})$ is smooth, the Hestenes-Stiefel conjugate gradient method is employed in this work. At the first iteration, the gradient direction is used

$$\Lambda(\mathbf{x}_0) = \mathbf{g}(\mathbf{x}_0) . \quad (3.38)$$

In the consequent iterations, the conjugate gradient is computed by

$$\Lambda(\mathbf{x}_n) = \mathbf{g}(\mathbf{x}_n) + \beta_n \Lambda(\mathbf{x}_{n-1}) , \quad (3.39)$$

where

$$\beta_n = \frac{\mathbf{g}_n^T (\mathbf{g}_n - \mathbf{g}_{n-1})}{\Lambda_{n-1}^T (\mathbf{g}_n - \mathbf{g}_{n-1})} . \quad (3.40)$$

To determine the step length, a line search approach is implemented in the current work. In this approach, besides the current position, one point with higher value and one point with lower value need to be found along the search direction. Then the value is interpolated using quadratic polynomial to find the minimum.

3.7 Examples

To evaluate the performance of our mesh optimization algorithm, we will present several examples to test our method based on the objective function $\Theta(\mathbf{x})$. After that, a numerical example will be given to compare these two objective functions $\Theta(\mathbf{x})$ and $\Gamma(\mathbf{x})$ discussed in this chapter. Five quality metrics are used to evaluate the mesh quality.

Q_{min} assesses the quality of the poorest shaped element and Q_{avg} is the average value. They are expressed as

$$Q_{min} = \min_{1 \leq i \leq n} Q_i \quad (3.41)$$

and

$$Q_{avg} = \frac{1}{n} \sum_{i=1}^n Q_i , \quad (3.42)$$

where n is the total number of the elements, Q_i represents the element quality for triangles and the minimum quality of the four sub-triangles in a quadrilateral mesh, respectively. For ideal triangular and quadrilateral elements, Q_{min} and Q_{avg} would be 1. To evaluate how tangled an invalid mesh is, σ_i is used to replace Q_i when an element is invalid.

Considering each angle of an element, we can detect the minimum angle α_{min} and maximum angle α_{max} in the whole mesh. They have the ideal value of 60° for triangular meshes and the ideal value of 90° for quadrilateral mesh.

The aspect ratio is the ratio of the longest edge to the shortest edge in one element. We compute the aspect ratios for each element and take the maximum value as the maximum aspect ratio r_{max} , which has the ideal value of 1.

3.7.1 Example I

The first example (Case 1) using a triangular mesh is shown in Figure 3.17. Figure 3.17 (Upper left) shows the initial mesh whose elements are tangled. Figure 3.17 (Upper middle)-(Lower right) show the smoothed meshes after 1, 2, 3, 4 and 5 iterations. Here, N_{el} , N_{nd} and N_{inv} indicate the number of elements, the number of nodes and the number of invalid elements, respectively. It can be observed that the number of invalid elements decreases very rapidly. Only five iterations are needed for untangling in this case.

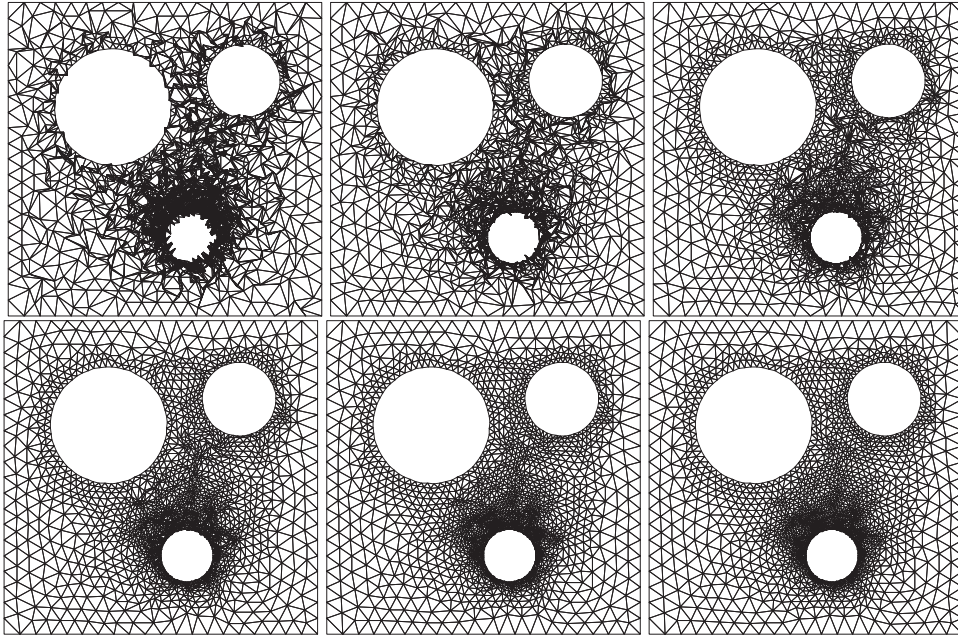


Figure 3.17: Case 1. Upper left: initial tangled mesh ($N_{el} = 3952$, $N_{nd} = 2119$, $N_{inv} = 1143$); Upper middle: smoothed mesh after the 1st iteration ($N_{inv} = 553$); Upper right: the 2nd iteration ($N_{inv} = 191$); Lower left: the 3rd iteration ($N_{inv} = 37$); Lower middle: the 4th iteration ($N_{inv} = 3$); Lower right: the 5th iteration ($N_{inv} = 0$).

3.7.2 Example II

Using a quadrilateral mesh, the second example (Case 2) is shown in Figure 3.18. Figure 3.18 (Upper left) shows the initial mesh whose elements are tangled. Figure 3.18 (Upper middle)-(Lower right) show the smoothed meshes after 1, 3, 5, 10 and 20 iterations. The mesh quality metrics (minimum element quality, average element quality, minimum angle, maximum angle and maximum aspect ratio) for these meshes are listed in Table 3.1. It can be seen that the mesh is untangled after only a few iterations, in the mean while, the mesh quality is significantly improved. In particular, the minimum element quality 0.706 and the average element quality 0.807 show that both, the worst element and overall mesh qualities after smoothing are improved.

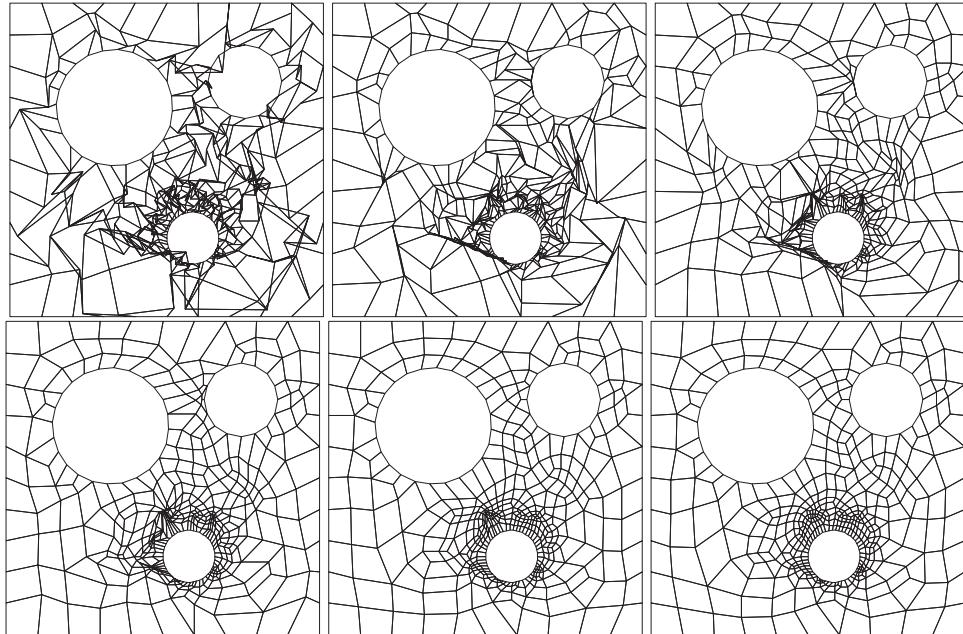


Figure 3.18: Case 2. Upper left: initial tangled mesh; Upper middle: smoothed mesh after the 1st iteration; Upper right: the 3rd iteration; Lower left: the 5th fifth iteration; Lower middle: the 10th iteration; Lower right: the 20th iteration.

metric	initial mesh	smoothed mesh after several iterations				
		1	3	5	10	20
Q_{min}	-45.869	-8.040	-0.270	-0.001	0.389	0.706
Q_{avg}	-1.368	-0.197	0.490	0.615	0.768	0.807
α_{min}	0.026	0.062	0.088	0.060	27.339	46.661
α_{max}	359.868	359.938	359.224	359.940	154.546	134.620
r_{max}	24.578	1366.212	1791.391	892.078	3.835	2.946

Table 3.1: Case 2. Mesh qualities for initial mesh and smoothed mesh.

3.7.3 Example III

In Case 3, we compare our method with the Laplacian method and the “smart” Laplacian method. The initial mesh and smoothed meshes are presented in Figure 3.19. We observe that the smoothed mesh produced by the Laplacian method has many invalid elements. The mesh, created by the new method is much better than the initial mesh and better than the smoothed meshes generated by the two other methods. The mesh quality metrics are shown in Table 3.2. The “smart” Laplacian method also produces some invalid elements although the average quality is good. In Figure 3.20, we show the number of invalid elements after each iteration step. The invalid elements are eliminated after five iterations with our new method. Although the number of invalid elements decreases more rapidly at the beginning while using the Laplacian and “smart” Laplacian methods, the invalid elements can’t vanish completely at later stages. The number of invalid elements even increases after a few iterations using the Laplacian method.

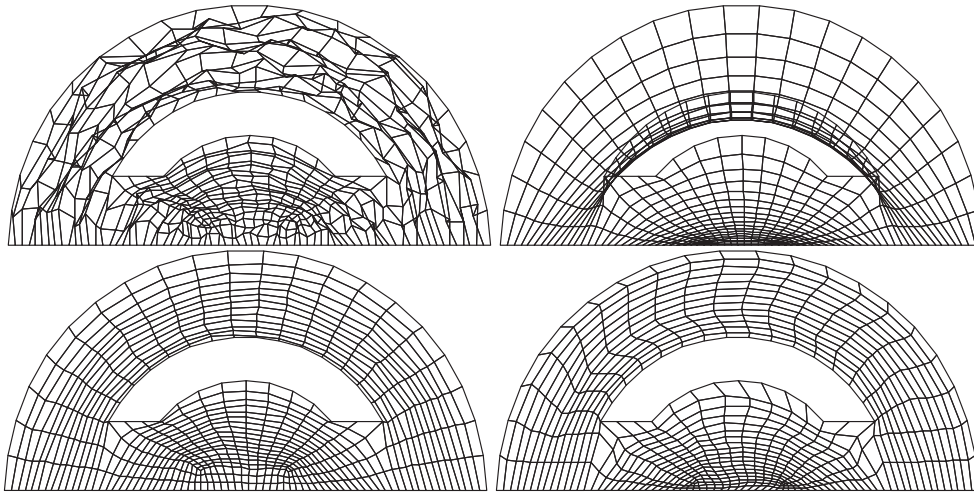


Figure 3.19: Case 3. Upper left: initial mesh; Upper right: Laplacian; Lower left: “smart” Laplacian; Lower right: new method.

metric	initial mesh	Laplacian	“smart” Laplacian	new method
Q_{min}	-20.535	-11.066	-0.421	0.358
Q_{avg}	-0.758	-0.0355	0.547	0.535
α_{min}	0.011	3.154	1.113	39.068
α_{max}	359.989	356.429	195.541	150.838
r_{max}	91.741	112.025	15.012	5.380

Table 3.2: Case 3. Mesh qualities for the initial mesh and the smoothed meshes.

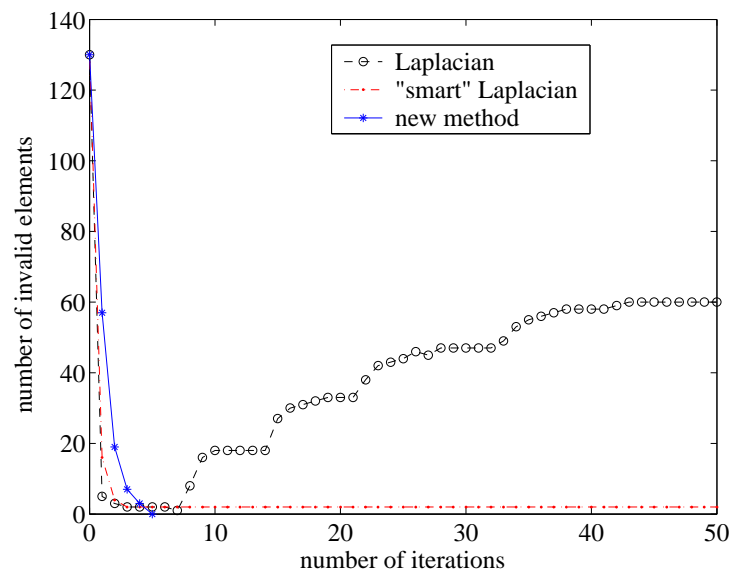


Figure 3.20: Case 3. Number of invalid elements inside the mesh after each iteration.

3.7.4 Example IV

The mesh quality distributions for Case 4 are shown in Figure 3.21. Note that there are still some badly shaped elements inside the smoothed meshes created by Laplacian method and “smart” Laplacian method. An overall high quality mesh is obtained with the new method (Figure 3.21 (Lower right)). In Figure 3.22, we show the convergence history for 50 iterations in terms of Q_{min} . It can be seen that Laplacian smoothing performs well at early stages, however, it fails to achieve an optimized mesh at later stages.

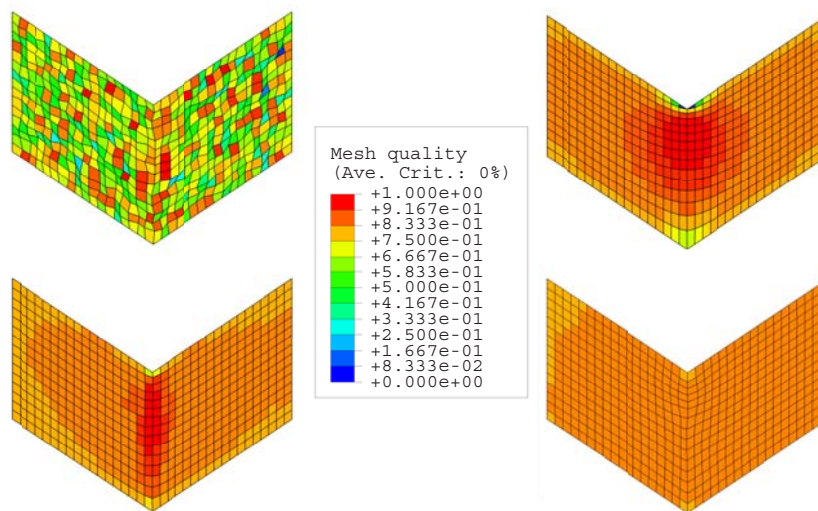


Figure 3.21: Case 4. Upper left: initial mesh; Upper right: Laplacian; Lower left: “smart” Laplacian; Lower right: new method.

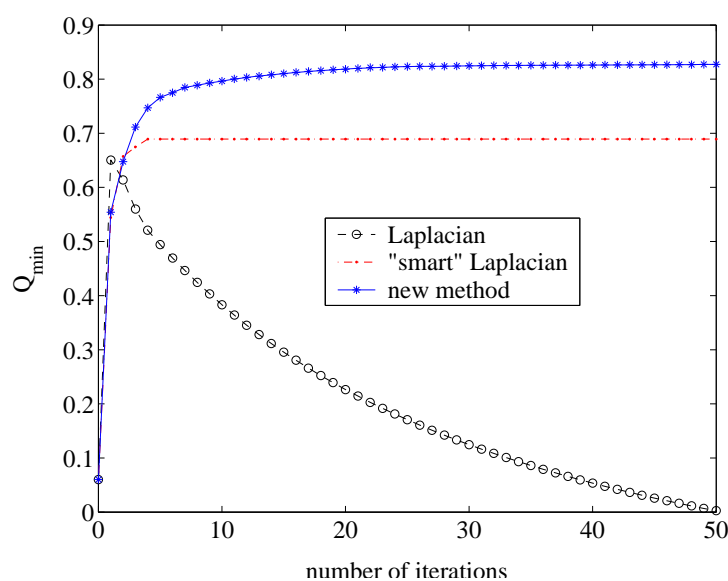


Figure 3.22: Case 4. Convergence history.

3.7.5 Example V

In the fifth case, the mesh quality distributions Q for the initial mesh and the smoothed meshes are shown in Figure 3.23. In Figure 3.23 (Upper right and Lower left), a bad quality element is indicated by yellow color. In Figure 3.23 (Lower right), we note that this element's quality is improved. The percentage of mesh quality distributions is illustrated in Figure 3.24, where the percentage of mesh quality is computed with the number of elements inside an interval of size 0.05. As it can be seen, using the optimization based smoothing, all the elements' quality locates at the interval between 0.8 and 1, which is nearly optimal. The mesh quality metrics are shown in Table 3.3.

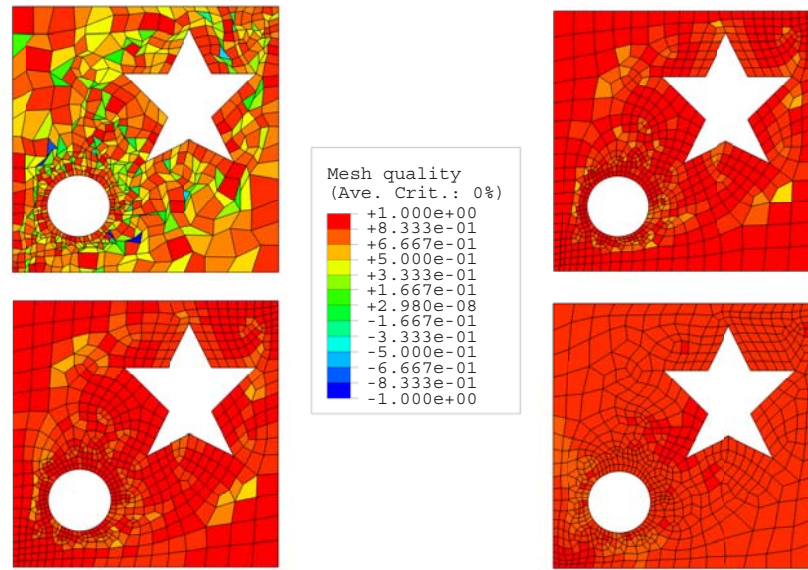


Figure 3.23: Case 5. Upper left: initial mesh; Upper right: Laplacian; Lower left: “smart” Laplacian; Lower right: new method.

metric	initial mesh	Laplacian	“smart” Laplacian	new method
Q_{min}	-0.946	0.579	0.533	0.820
Q_{avg}	0.596	0.907	0.902	0.868
α_{min}	3.433	45.511	46.313	55.370
α_{max}	356.493	144.613	147.505	124.698
r_{max}	13.328	2.381	2.434	2.314

Table 3.3: Case 5. Mesh quality for the initial mesh and the smoothed mesh.

3.7.6 Example VI

Using Case 1 again, the sixth example is given to compare the objective functions $\Theta(\mathbf{x})$ and $\Gamma(\mathbf{x})$. A group of tangled meshes are generated by perturbing interior nodes randomly. Table 3.4 shows the comparison on mesh untangling. Here, N_{inv} is the number of invalid elements in the initial tangled mesh, I_{unt} is the number of iterations which are required to untangle the mesh. As

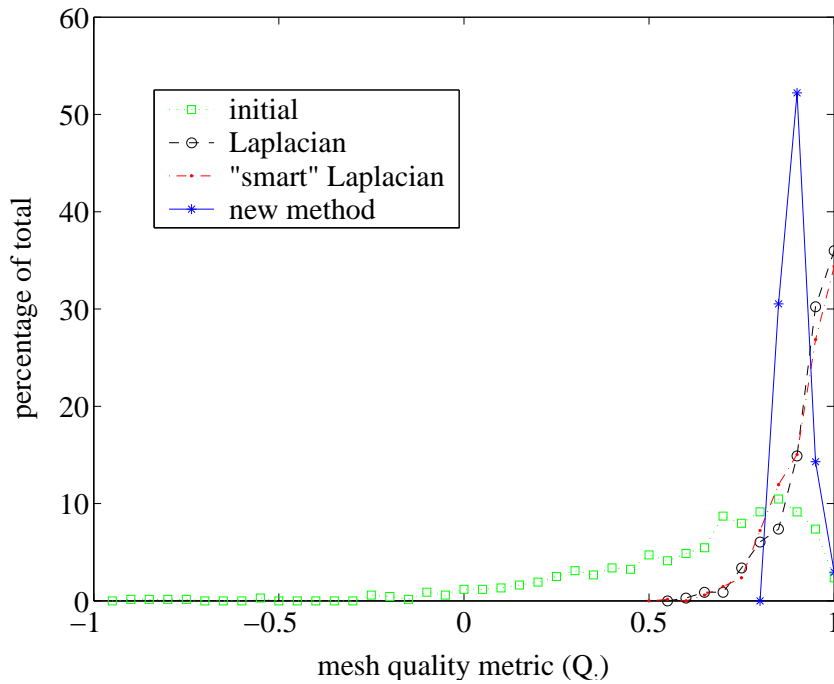


Figure 3.24: Case 5. The percentage of mesh quality distributions. Here, the percentage of mesh quality is computed with the number of elements inside an interval of size 0.05.

can be seen, the mesh is untangled after only a few iterations by both of the objective functions. The computation costs are also very similar (only a few seconds).

The minimum and average element qualities of the smoothed meshes are shown in Table 3.5. It can be seen that the worst element quality of the smoothed mesh in the objective function $\Theta(\mathbf{x})$ is higher than that in the objective function $\Gamma(\mathbf{x})$. In contrast, the average element quality in the objective function $\Theta(\mathbf{x})$ is less than that in the objective function $\Gamma(\mathbf{x})$. The reason is that the objective function $\Theta(\mathbf{x})$ is designed to improve the worst element quality while the objective function $\Gamma(\mathbf{x})$ is designed to improve the average element quality.

N_{inv}	$I_{unt}(\Theta(\mathbf{x}))$	time(s)($\Theta(\mathbf{x}))$	$I_{unt}(\Gamma(\mathbf{x}))$	time(s)($\Gamma(\mathbf{x}))$
155	3	1.012	2	0.987
302	3	1.282	2	1.157
567	4	1.593	3	1.458
1143	5	1.972	4	1.816

Table 3.4: Comparison on mesh untangling.

3.7.7 Example VII

Finally, the last example is presented, in which the distorted mesh is obtained from an extrusion simulation. An element is degenerated in the distorted mesh due to the large deformations during the extrusion simulation. Figure 3.25 shows the distorted mesh and smoothed mesh. The degenerated element in the distorted mesh is indicated by blue color. It can be seen that the quality of this element is significantly improved by our smoothing method. Besides the

N_{inv}	$Q_{min}(\Theta(\mathbf{x}))$	$Q_{avg}(\Theta(\mathbf{x}))$	$Q_{min}(\Gamma(\mathbf{x}))$	$Q_{avg}(\Gamma(\mathbf{x}))$
155	0.859	0.958	0.736	0.982
302	0.855	0.958	0.748	0.982
567	0.852	0.953	0.750	0.981
1143	0.855	0.953	0.744	0.982

Table 3.5: Comparison on mesh qualities after fifteen smoothing iterations.

degenerated element, we also note that the qualities of many elements whose color is yellow in the distorted mesh are improved by mesh smoothing.

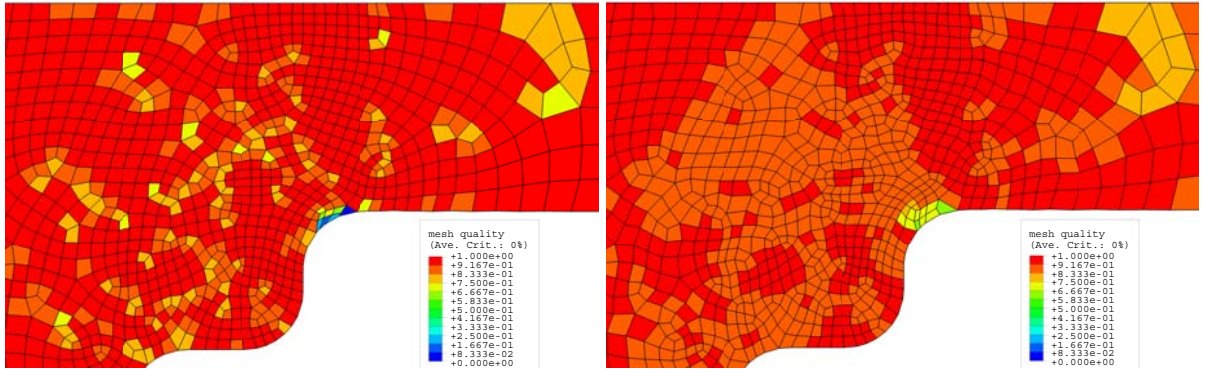


Figure 3.25: Mesh smoothing for extrusion simulation. Left: distorted mesh; Right: smoothed mesh.

3.8 Conclusions

In this chapter, an optimization based mesh smoothing scheme based on the mesh quality measure, derived from the condition number of the Jacobian matrix, has been presented to optimize a mesh by moving nodes. Using the steepest descent method, untangling and smoothing is carried out with the new objective function, simultaneously. Numerical experiments demonstrate that the proposed mesh optimization approach is effective for both, invalid and valid meshes. The comparison between the current objective function and alternative objective functions proposed by Escobar et al. (2003) validates the robustness on improvement of the worst quality element using the current objective function.

Although the smoothing techniques discussed in this chapter are focused on improvement of mesh quality, it can be extended to the field of r-adaptivity which is also called adaptive moving mesh (*e.g.*, Branets and Carey, 2004; Kanchi and Masud, 2007; Mieke and Gurses, 2007; Nordlund et al., 1998; Oden et al., 1986; Tan and Huang, 2008), which moves nodes to achieve the desired element size instead of an optimal mesh quality. In this case, a size measure needs to be incorporated inside the objective function for optimization. Furthermore, one can combine a mesh quality measure and a size measure to achieve a compromise, which is an interesting topic in adaptive finite element analysis.

Chapter 4

Adaptive remeshing for metal forming simulations

Abstract – Finite element simulations of metal forming processes often involve mesh distortion due to the material flow. From a practical point of view, static mesh density distribution lacks efficiency for stress concentration or strain localization problems. Due to this fact, an adaptive remeshing procedure is essential for the simulation of metal forming processes. In the current work, a fully automatic remeshing strategy is presented. To achieve a prescribed accuracy, an *a posteriori* error estimator controls the hr-adaptivity procedure. After each remeshing step, the state variables and boundary conditions are transferred from the old to the new mesh. Several examples of metal forming simulations are presented to demonstrate the performance of the adaptive remeshing scheme.

Keywords: adaptive remeshing, error estimation, mesh size map, data transfer, metal forming.

4.1 Introduction

Manufacturing processes, such as metal forming and cutting, play an important role in modern industry. Traditionally, a great deal of experience has been accumulated by using the trial and error process. However, the mechanical and thermal properties of the material and the mechanics of metal forming processes are not fully understood yet. The cost of a trial and error process can be very expensive due to the high cost of prototypes and experiments. In addition, the requirement of a lot of trials and errors leads to long design periods. Therefore, mathematical modelling tools such as the finite element method have been developed to reduce the number of prototypes and design iterations. In the past decade, the computational power of modern computers has been significantly improved, so that the finite element method has been applied to the simulation of manufacturing processes by more and more industrial companies.

In the context of the finite element method, a deformable body is discretized by a mesh, which is defined by a finite number of nodes and elements. The solution is approximated and interpolated by the shape functions of elements inside the mesh. The geometrical shape of an element, which can be evaluated by a mesh quality measure, certainly, has effect on its shape function. Although there is no direct relationship between solution accuracy and mesh quality because solution accuracy highly depends on the problem being analyzed, it is well known that severely distorted meshes reduce the solution accuracy (Oddy et al., 1988). In the Lagrangian formulation, the mesh of a workpiece evolves to represent the material flow. During the simulation of manufacturing processes, the mesh often undergoes large deformation, which could result in large discretization errors, numerical difficulties and even in failure of the simulation. Therefore, remeshing techniques are required to update distorted meshes frequently for such large deformation problems. In addition, strain localization and stress concentration often occur in the simulation of manufacturing processes. A small local element size is required to

predict the solution in the localization area in which the solution gradient is very high. Given a prescribed accuracy, obviously, uniform mesh density lacks efficiency. Thus, an adaptive remeshing technique is required to generate graded meshes and improve computational efficiency within a certain accuracy.

An adaptive remeshing strategy includes three main factors:

1. an error estimator for the assessment of the accuracy of the finite element solution,
2. a mesh generator for the generation of a new mesh and
3. a mapping scheme which transfers the solution from the old to the new mesh.

In addition, a mesh size optimization scheme is required to convert the estimated error map to a new mesh size map, which needs to be imported to a mesh generator.

In the past twenty years, adaptive remeshing strategies have been investigated and widely applied to various problems. A goal oriented adaptivity strategy based on point-wise error representation was proposed by Diez et al. (2007). Baeker et al. (2002); Diez et al. (2000); Huerta and Diez (2000); Huerta et al. (1999); Khoei et al. (2005); Peric et al. (1994); Selman et al. (1997) and Khoei et al. (2007) applied adaptive remeshing for strain localization problems. Several adaptive remeshing strategies for fracture and damage problems were introduced by Borouchaki et al. (2005); Bouchard et al. (2003, 2000); Espinosa et al. (1998); Jr. and Owen (2001); Murthy and Mukhopadhyay (2000); Rodriguez-Ferran and Huerta (2000); Rodriguez-Ferran et al. (2004); Secchi et al. (2007) and Khoei et al. (2008). On the application to production processes, such as forging, extrusion, deep drawing, welding and so on, a great deal of work has been presented (*e.g.*, Boussetta et al., 2006; Fernandes and Martins, 2007; Gautham et al., 2003; Hamide et al., 2008; Hyun and Lindgren, 2004; Khoei and Lewis, 2002, 1999; Kubli and Reissner, 1995; Kwak et al., 2002; Kwak and Im, 2002; Lee et al., 2007; Lewis and Khoei, 2001; Li et al., 2000; Owen and Jr., 1999; Park and Yang, 2006; PavanaChand and KrishnaKumar, 1998; Peric et al., 1999; Pires et al., 2004; Ravindranath and Kumar, 2000; Rieger and Wriggers, 2004; Sheng et al., 2004; Xing et al., 1999).

In this chapter, we investigate and discuss each of the factors in adaptive remeshing and present the applications of adaptive remeshing strategy in several metal forming simulations. The chapter is organized as follows: Recovery techniques are briefly reviewed in §4.2. Several error estimators are given in §4.3. In §4.4, the optimization of the mesh size map is discussed. The mapping algorithms are introduced in §4.5. In §4.6, the examples of extrusion, cutting, forging and rolling are simulated to validate the proposed adaptive remeshing strategy. For large deformation problems with damage, an adaptive remeshing with damaged element elimination procedure is proposed in §4.7. The conclusions are given in the last section.

4.2 Error estimation

In the current work, two recovery based error estimation techniques are implemented to obtain the improved finite element solution.

4.2.1 Superconvergent patch recovery (SPR)

The original superconvergent patch recovery method (SPR) is based on a least-squares fit of derivatives at the optimal sampling points. In this work, integration points are chosen as sampling points. The node patch (see Figure 4.1) is defined for the SPR method by the union of elements surrounding the node in question.

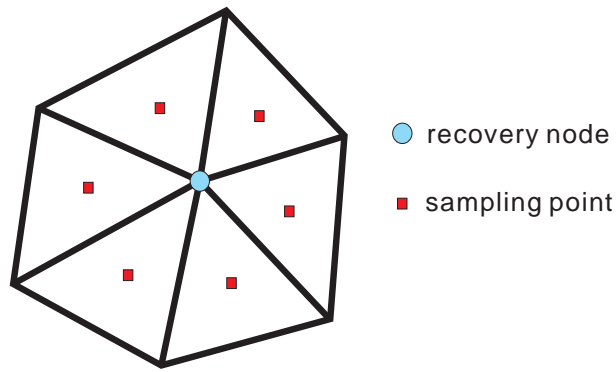


Figure 4.1: Node patch.

Let σ^* represent any component of the recovered element stress field. This is related to the set $\mathbf{s}_m = (s_1, s_2, \dots)$ of corresponding nodal values at the mesh nodes via the usual ansatz

$$\sigma^* = \mathbf{h}_m \cdot \mathbf{s}_m^* . \quad (4.1)$$

in terms of the array $\mathbf{h}_m = (h_1, h_2, \dots)$ of element shape functions. The set \mathbf{s}_m is obtained by assuming that σ^* is given by an order p polynomial expansion over a node patch, *i.e.*,

$$\sigma^* \equiv \sigma_p^* = \mathbf{p} \cdot \mathbf{a} , \quad (4.2)$$

where \mathbf{p} is an array consisting of the terms of an order p polynomial and \mathbf{a} is a set of unknown parameters. In the case of a three-node triangular elements, for example, we have

$$\mathbf{p} = (1, x, y) \quad (4.3)$$

and

$$\mathbf{a} = (a_1, a_2, a_3) . \quad (4.4)$$

Then

$$\sigma_p^* = a_1 + a_2x + a_3y \quad (4.5)$$

follows. The unknown parameters \mathbf{a} are determined by a least square fit to a set of sample points at which the stress component σ_h , obtained from the finite-element solution, is known to

be superconvergent or at least highly accurate. The least-squares fit is based on minimizing the objective function

$$f(\mathbf{a}) = \sum_{i=1}^n |\sigma_h(x_i, y_i) - \sigma_p^*(x_i, y_i)|^2, \quad (4.6)$$

with n the number of sampling points and $(x_1, y_1), (x_2, y_2), \dots$ the coordinates of these points. Extremization of $f(\mathbf{a})$ yields the linear system

$$\mathbf{A}\mathbf{a} = \mathbf{b}, \quad (4.7)$$

with

$$\mathbf{A} = \sum_{i=1}^n \mathbf{p}(x_i, y_i) \otimes \mathbf{p}(x_i, y_i) \quad (4.8)$$

and

$$\mathbf{b} = \sum_{i=1}^n \sigma_h(x_i, y_i) \mathbf{p}(x_i, y_i). \quad (4.9)$$

4.2.2 Recovery method based on local extrapolation (BF)

With the help of 2×2 integration points at one quadrilateral element, the recovered solution field can be obtained by using local extrapolation (Hinton and Campbell, 1974). In the case of a linear triangular element, one integration point is not sufficient for local extrapolation. The average derivative at the midpoint of the common edge of neighboring elements in structured mesh was shown to be superconvergent by Levine (1985). Hence local extrapolation can be realized by using such midpoints. In practice, unstructured meshes are usually employed instead of structured mesh. Therefore, the corresponding optimal point for unstructured meshes has to be investigated. The details are referred to Chapter 1. Given the best-fit point for unstructured meshes, we consider the element patch as given in Figure 4.2.

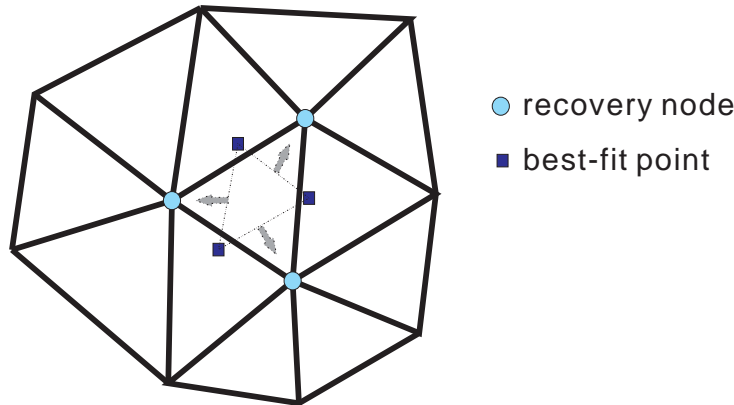


Figure 4.2: Element patch for local extrapolation.

The recovery procedure based on local extrapolation is summarized as follows:

1. average the derivatives at the best-fit point,
2. extrapolate these three superconvergent values to the nodes and
3. calculate the average value of the overlapping recovered solutions at the nodes.

4.3 A posteriori error estimation

In the category of recovery based error estimation, the discretization error of finite element solution is evaluated by comparing the finite element solution and the recovered solution. In the past 20 years several recovery based error estimators have been proposed (*e.g.*, Gallimard et al., 1996; Lee and Bathe, 1994; Li and Bettess, 1997; Peric et al., 1994; Zienkiewicz et al., 1988; Zienkiewicz and Zhu, 1987, 1992a,b). For linear elasticity problems, one can simply use the derivatives of displacement or stresses to evaluate the discretization error (Lee and Bathe, 1994; Zienkiewicz and Zhu, 1992a,b, *e.g.*). In the case of nonlinear plasticity problems, it is much more sophisticated since the error estimation for plasticity problems is highly problem dependent (Li and Bettess, 1997). Here, it is recommended to design various error estimators for various simulation purposes. In the following, we will review possible quantities to be used in context of error estimation.

4.3.1 The incremental energy (EIE)

The error estimator based on the incremental energy was proposed by Boroomand and Zienkiewicz (1999). This error estimator is based on the increment of recovered stresses and recovered strains. The incremental energy norm is defined as

$$\|e\|_{\Omega} = \left(\int_{\Omega} |(\sigma^* - \sigma^h)(\Delta\varepsilon^* - \Delta\varepsilon^h)| d\Omega \right)^{1/2}, \quad (4.10)$$

where σ and σ^h are the recovered stresses and the finite element approximation of stresses, respectively. $\Delta\varepsilon$ and $\Delta\varepsilon^h$ are the recovered incremental strains and the finite element approximation of strains, respectively. In the n^{th} increment the above norm may be written as

$$\|e\|_{\Omega} = \left(\int_{\Omega} |(\sigma_n^* - \sigma_n^h)(\Delta\varepsilon_n^* - \Delta\varepsilon_n^h)| d\Omega \right)^{1/2}, \quad (4.11)$$

where

$$\begin{aligned} \Delta\varepsilon_n^* &= \varepsilon_n^* - \varepsilon_{n-1}^* \\ \Delta\varepsilon_n^h &= \varepsilon_n^h - \varepsilon_{n-1}^h \end{aligned} \quad (4.12)$$

Peric et al. (1994) proposed a similar error estimator with the plastic strain increment instead of the strain.

4.3.2 The incremental strain error (EIS)

Similar to the error estimator based on energy norm, we can use an error estimator which emphasizes the discretization error in strain rate. The error in the n^{th} incremental step is expressed as follows:

$$\|e\|_{\Omega} = \left(\int_{\Omega} (\Delta\varepsilon_n^* - \Delta\varepsilon_n^h)^2 d\Omega \right)^{1/2} \quad (4.13)$$

where $\Delta\varepsilon_n^h$ is the finite element approximation of strain increment in the n^{th} incremental step, $\Delta\varepsilon_n^*$ is the recovered solution of $\Delta\varepsilon_n^h$.

4.3.3 The equivalent plastic strain error (EEPS)

In the applications to strain localization problems, we note that the strain rate based error estimators show high efficiency in catching shear band when the shear band is being formulated. However, once the strain rate lowers down, consequent mesh coarsening causes the loss of the solutions in the formulated shear band. Therefore, a total strain based error estimator needs to be considered for this special situation. Here, an error estimator based on effective plastic strain is given by

$$\|e\|_{\Omega} = \left(\int_{\Omega} (\varepsilon_{ep}^* - \varepsilon_{ep}^h)^2 d\Omega \right)^{1/2} \quad (4.14)$$

where ε_{ep}^h is the finite element approximation of effective plastic strain, ε_{ep}^* is the recovered solution of ε_{ep}^h .

4.4 Optimization of mesh size map

After the assessment of the discretization error in a finite element solution, the next step in an adaptive remeshing strategy is to generate an optimized new mesh size map based on the estimated error. The aim of optimization of mesh size map is to achieve a prescribed solution accuracy with the least elements.

Let η be the global relative error in a finite element solution, which is defined as

$$\eta = \frac{\|e\|}{\|u_h\|}, \quad (4.15)$$

where $\|u_h\|$ is computed with the finite element solution. Then, the local relative error in the element i is expressed as

$$\eta_i = \frac{\|e\|_i}{\|u_h\|}, \quad (4.16)$$

where $\|e\|_i$ is the elemental error in the element i .

To describe the local mesh size optimization strategy, we inherit the idea about the local remeshing indicator ξ , which was proposed by Bugeda (2002) and rewrite the indicator in the following form

$$\xi_i = \frac{\eta_i}{\eta_{p_i}}, \quad (4.17)$$

where η_{p_i} is the prescribed relative error in element i . Note that the current element size fits the expected element size if $\xi_i = 1$, refinement is required if $\xi_i > 1$, and coarsening is required if $\xi_i < 1$. Given a global prescribed error, one needs a criterion to determine the distribution of the prescribed error in the mesh. Several remeshing strategies have been proposed in the past 20 years (e.g., Boroomand and Zienkiewicz, 1999; Bugeda, 2002; Bugeda and Onate, 1993; Diez et al., 2000; Diez and Huerta, 1999; Li and Bettess, 1995; Li et al., 1995; Zienkiewicz and Zhu, 1987). Generally, those strategies can be classified into two categories:

1. uniform elemental error distribution (*e.g.*, Boroomand and Zienkiewicz, 1999; Fuenmayor and Oliver, 1996; Li and Bettess, 1995; Li et al., 1995; Zienkiewicz and Zhu, 1987);
2. uniform error density distribution (*e.g.*, Bugada, 2002; Bugada and Onate, 1993).

4.4.1 Equal distribution of the elemental error (MDE)

The most popular optimization algorithm of mesh size map is to enforce the error to be equally distributed between all elements (Zienkiewicz and Zhu, 1987). Let n be the total number of elements and η_{p_i} the elemental prescribed relative error. Combining equations (4.15) and (4.16), the global prescribed relative error is then computed by

$$\eta_p = \left(\sum_{i=1}^n \eta_{p_i}^2 \right)^{1/2}. \quad (4.18)$$

Enforcing η_{p_i} to be uniformly distributed on each element, we have

$$\eta_{p_i} = \frac{\eta_p}{\sqrt{n}}. \quad (4.19)$$

Considering Equation (4.17) again, the local remeshing indicator ξ_i can be rewritten as

$$\xi_i = \frac{\eta_i \sqrt{n}}{\eta_p}. \quad (4.20)$$

According to the convergence rate of discretization error, the ratio of the old local element size to the new local element size is computed by Zienkiewicz and Zhu (1987)

$$\frac{h_i^{old}}{h_i^{new}} = (\xi_i)^{1/p} = \left(\frac{\eta_i \sqrt{n}}{\eta_p} \right)^{1/p}, \quad (4.21)$$

with p , the polynomial degree of the element interpolating functions. Hence, we obtain the new element size which is expressed as

$$h_i^{new} = h_i^{old} \left(\frac{\eta_p}{\eta_i \sqrt{n}} \right)^{1/p}. \quad (4.22)$$

4.4.2 Constrained computational costs based optimization strategy (MCE)

Although the prescribed error based mesh size optimization strategy has a direct relationship with the expected solution accuracy, it can lead to high computational costs, if the prescribed accuracy is not given accordingly. Since for practical metal forming simulations, the material flow can become more and more complicated during the forming process, a fixed prescribed accuracy would result in a huge total number of elements. Therefore, from a practical point of view, constraining the computational costs is also an important issue in adaptive remeshing. A few approaches have been proposed, to constrain the computational costs by imposing a

prescribed number of elements, prescribed memory or prescribed CPU time (Boussetta et al., 2006; Coorevits and Bellenger, 2004).

Given a prescribed accuracy, we can approximate the total number of new elements by using (Li et al., 1995)

$$n_p = \sum_{i=1}^n \left(\frac{h_i^{old}}{h_i^{new}} \right)^2 = \sum_{i=1}^n \left(\frac{\eta_i}{\eta_{p_i}} \right)^{2/p}. \quad (4.23)$$

With the imposed number of elements n_{imp} , the adjusted prescribed accuracy according to the prescribed number of elements is expressed as

$$\eta_{imp} = \eta_p \left(\frac{n_p}{n_{imp}} \right)^{p/2}. \quad (4.24)$$

In addition, in adaptive simulations for large deformation problems, the total number of remeshing steps is highly dependent on the minimum element size. For example, in the simulation of an extrusion process, the tool displacement in each remeshing step is suggested to be less than the minimum element size, otherwise, the mesh could be extremely distorted or even degenerated. It is known that a large number of mapping steps could result in error in the mapped solution. Hence the total number of remeshing steps should be restricted by specifying a minimum element size.

While determining the new mesh density, based on error estimation, we note that the error could be zero in some regions, where the solution, such as plastic strain, used for error estimation is zero. In this case, the new element size calculated by equation (4.22) is infinite, which could result in an extremely coarse new mesh and consequently lead to numerical difficulties in the next time step. Therefore a maximum element size can be imposed to overcome this problem.

4.5 Mapping algorithm

After each remeshing step, all state variables, such as velocities, stresses, temperatures and hardening parameters, have to be transferred from the old mesh to the new mesh (*e.g.*, Araujo et al., 2000; Boroomand and Zienkiewicz, 1999; Cecot, 2007b; Cirak and Ramm, 2000; Fernandes and Martins, 2007; Kalhori, 2001; Khoei et al., 2007; Mediavilla et al., 2006; PavanaChand and KrishnaKumar, 1998; Peric et al., 1996, 1999; Ravindranath and Kumar, 2000). Data transfer is a key issue in an adaptive finite element analysis, since the mapping algorithm directly affects the initial condition of the next analysis step. Unsuitable mapping algorithms could cause large errors between the original solution and mapped solution and consequently lead to an inaccurate final simulation result.

The mapping process consists basically of identifying the element inside the old mesh that contains the node n of the new mesh and subsequent transfer of the state variables from the old mesh to the new mesh.

4.5.1 Element identification

Before transferring the state variables from the old to the new mesh, the old element, which contains the new point has to be identified. An overall searching algorithm is quite time consuming. To overcome this problem, an efficient searching algorithm is required. Selman et al. (1997) proposed a searching technique by using area-coordinates. Zhao et al. (1999) developed a searching algorithm specifically for bilinear quadrilateral elements. In the current work, we use a searching technique which is based on a background grid (Hortig and Svendsen, 2008). In this method, a background grid with an appropriate number of elements is built to classify the old elements. Thus, the searching is performed within a reduced domain of background elements instead of the whole domain, which drastically decreases the computational costs on the searching process.

4.5.2 Data transfer

The state variables, which are available at nodes, can be interpolated directly from the old nodes to the new nodes. However, the transfer of variables from old gauss points to the new ones is somehow tricky. In most cases, the state variables in the old mesh are first projected to nodes, then the values at the new integration points of the new mesh are computed by simple interpolation of the old nodal value using the original shape functions (*e.g.*, Araujo et al., 2000; PavanaChand and KrishnaKumar, 1998; Peric et al., 1996; Ravindranath and Kumar, 2000). Boroomand and Zienkiewicz (1999) introduced a new mapping strategy in which the state variables are transferred from the old integration points to the ones directly.

In the field of recovery-based error estimation, a great deal of solution recovery techniques have been developed to obtain a recovered solution which is supposed to be more accurate than the original finite element solution. Naturally, these recovery techniques can be also utilized to improve the finite element solution before mapping it from the old to the new mesh. In the current work, three recovery techniques are implemented to improve the finite element solution. These are nodal averaging (NA), superconvergent patch recovery (SPR) and best-fit point based extrapolation (BF) techniques.

The procedure of data transfer is summarized as follows:

1. identify the old element, which contains the new node or integration point,
2. for the state variables at integration points, smooth the original state variables to obtain the recovered values at nodes by using recovery techniques,
3. compute the local coordinates of the new nodes,
4. transfer the recovered nodal values from the old mesh to the new mesh, using the shape functions of the corresponding old elements.

4.6 Metal forming simulation

In this section, several examples of adaptive finite element simulations of production processes are presented. The adaptive remeshing strategy is shown in Figure 4.3. After each calculation

step, an a posteriori error estimator is employed to assess the discretization error. Consequently, a new mesh is generated by a mesh generator with the help of an optimization algorithm for the mesh size map. After that, the state variables and boundary conditions are transferred from the old to the new mesh. Finally, a new finite element model, based on the new mesh is built for the finite element analysis for the next time step.

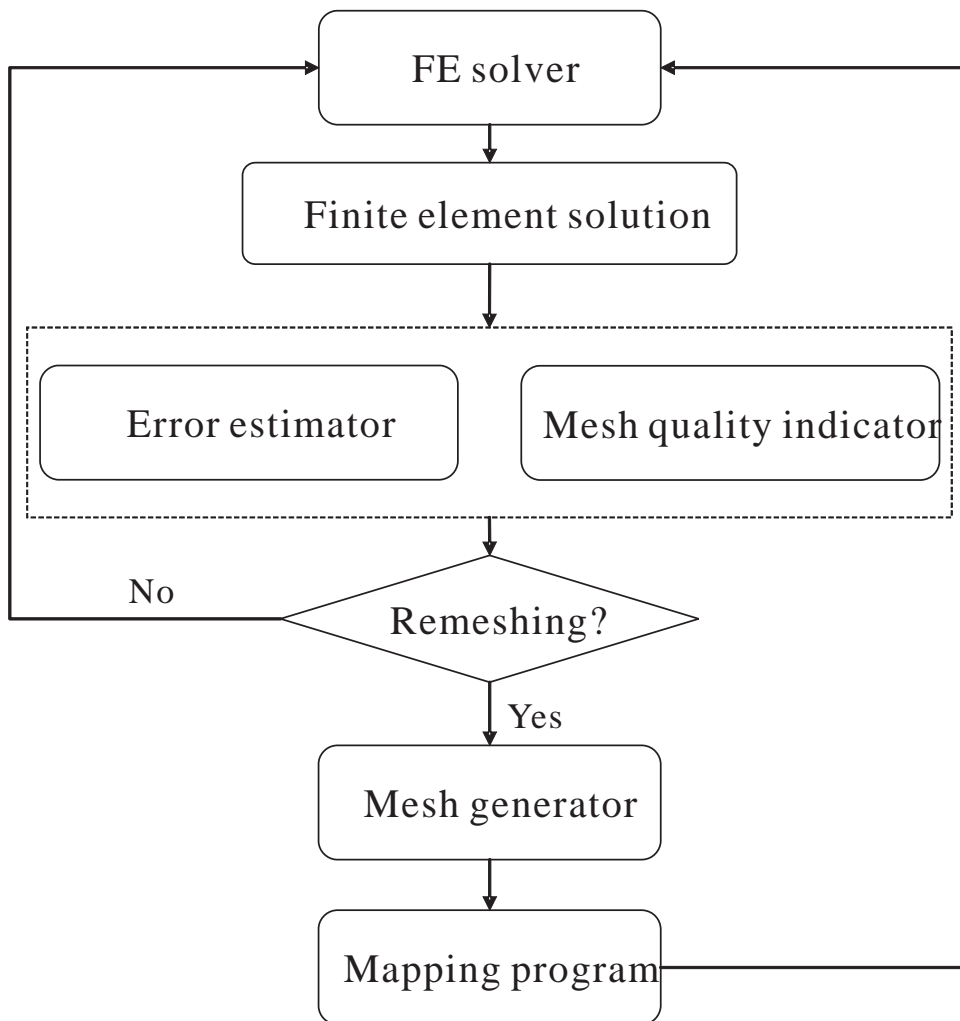


Figure 4.3: Workflow of the adaptive finite element simulation procedure (see text for details).

4.6.1 Extrusion simulation

Extrusion is a manufacturing process, used to produce objects with a fixed cross section (*e.g.*, pipes), in which a material is extruded through a die of the desired cross section. Two examples are presented in this section. The first example is a forward extrusion of aluminum alloy. The simulation involves severe mesh distortion when the material is extruded through the neck region. Taking advantage of axis symmetry, the problem is analyzed with an axis symmetric model (see Figure 4.4). The material behavior is assumed to be linear isotropic hardening. Element sizes $h_{min} = 1$ mm and $h_{max} = 5$ mm are specified for adaptive remeshing.

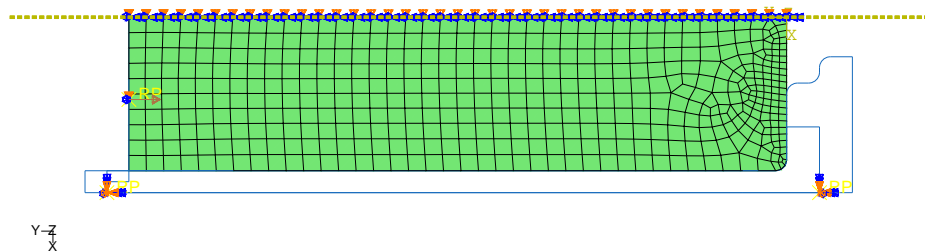


Figure 4.4: The initial mesh and boundary conditions for the forward extrusion process.

Figure 4.5 shows the adapted meshes and the distribution of equivalent plastic strain at different punch displacements. It can be seen, that the mesh near the bottom of the container is refined due to high strains. This is induced by the friction between the material and the container. The mesh near the neck region is also refined where the material undergoes large deformations. The distribution of equivalent plastic strain in the 3D representation of the workpiece is shown in Figure 4.6.

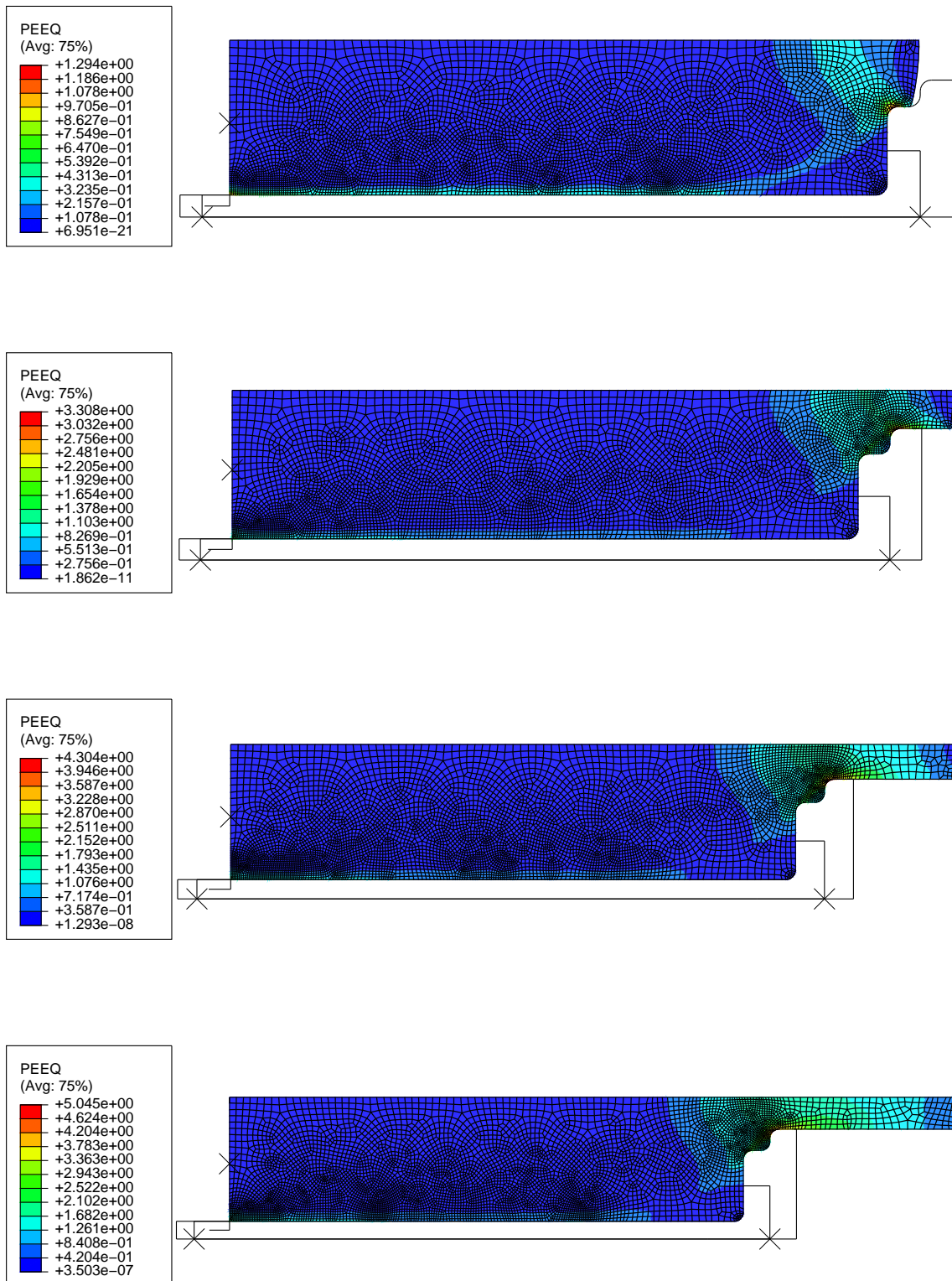


Figure 4.5: Adapted meshes at displacement of 5, 10, 15 and 20 mm using the EIE error estimator.

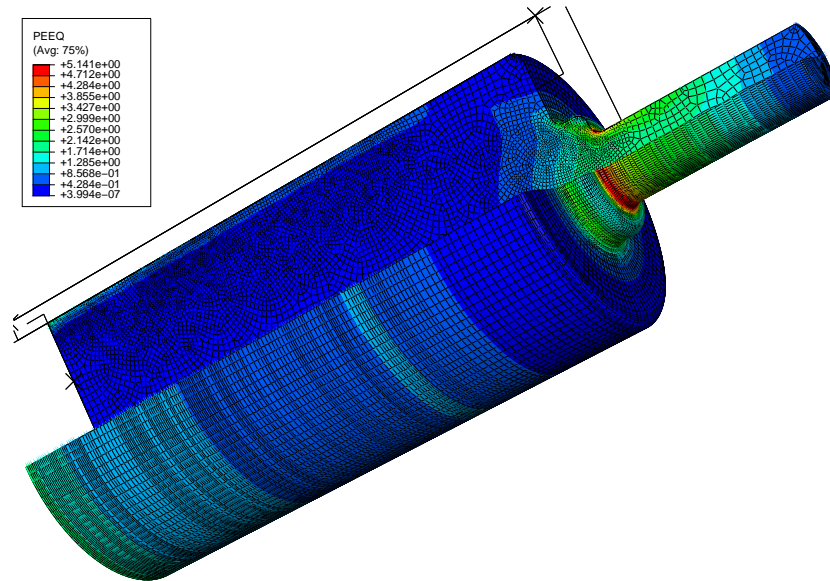


Figure 4.6: Distribution of the equivalent plastic strain in the workpiece.

The meshes before and after remeshing are shown in Figure 4.7. It can be seen, that some elements near the die in the neck region are highly distorted before remeshing. The mesh quality is significantly improved by updating the deformed mesh (the worst element quality in the deformed mesh is 0.1395 and the worst element quality in the updated mesh is 0.5285). The worst element quality of the meshes before and after remeshing during the whole adaptive simulation is plotted in Figure 4.8.

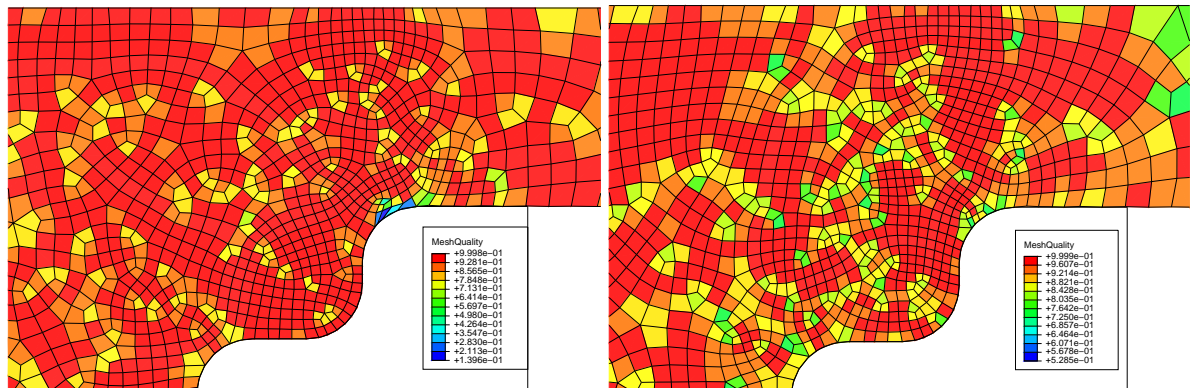


Figure 4.7: Meshes before and after remeshing. Left: before remeshing; Right: after remeshing.

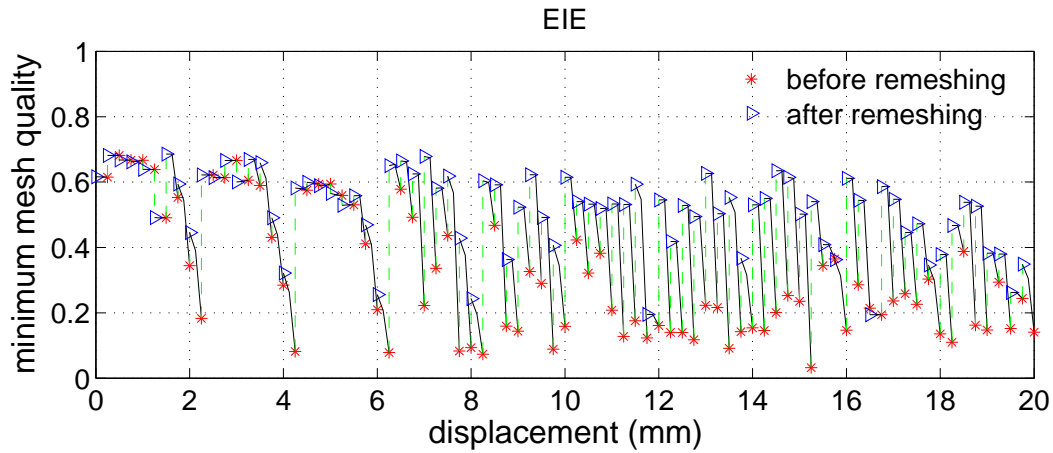


Figure 4.8: Mesh quality during the adaptive simulation.

Comparison on various error estimators

To compare the performance of different error estimators, three different error estimators EEPS, EIS and EIE are employed to drive the adaptive simulation. Figure 4.9 shows the simulation results based on different error estimators. It can be observed that the mesh is coarsened after it goes through the die while using the EIS and EIE error estimator. This is because the strain rate decreases rapidly after the material passes the die. In contrast, while using the EEPS error estimator, the mesh density is almost fixed.

Figure 4.10 shows the number of elements during the adaptive simulation. The discretization errors in the simulation are shown in Figure 4.11.

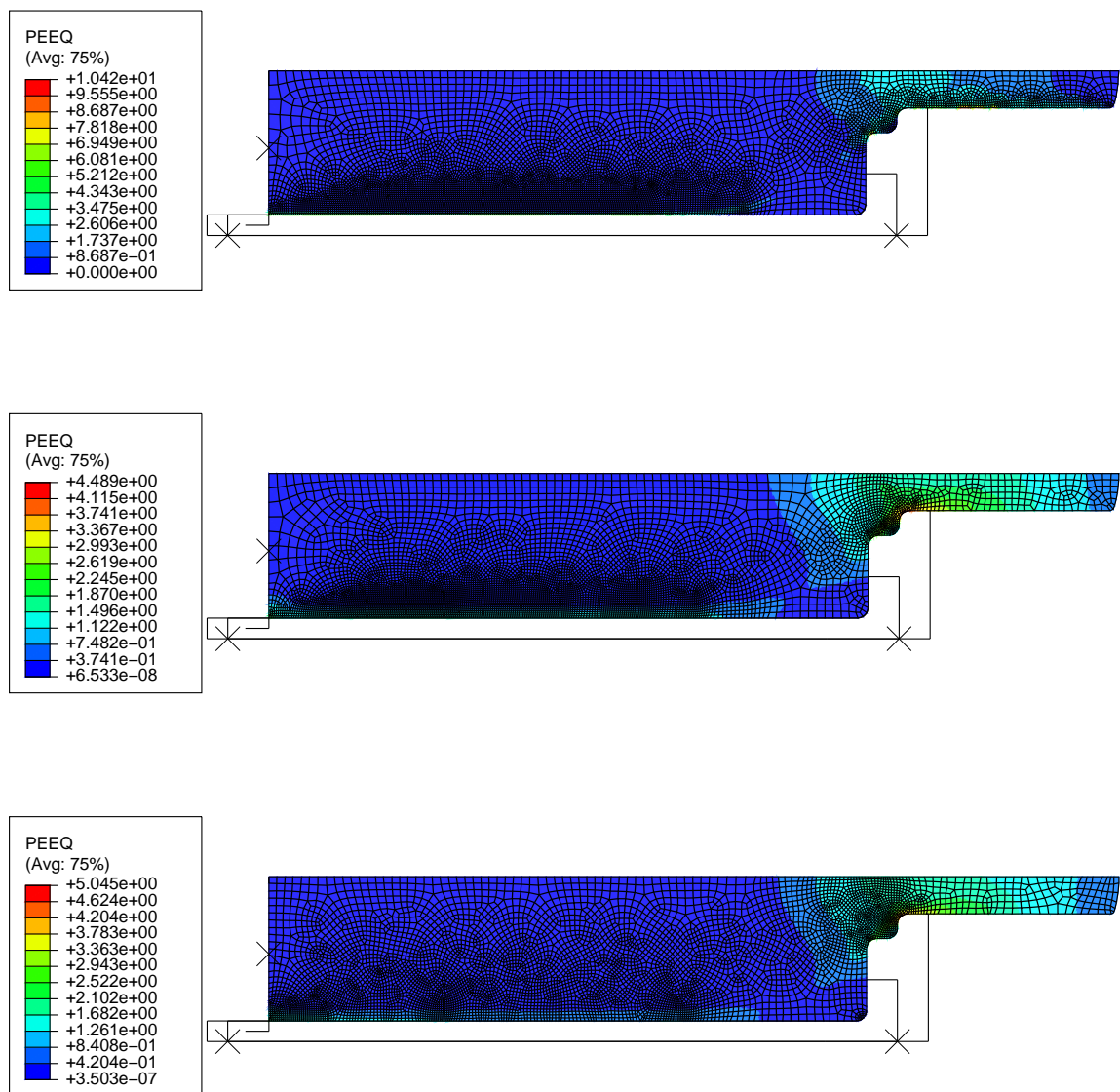


Figure 4.9: Adapted meshes using different error estimators. Upper: EEPS; Middle: EIS; Lower: EIE.

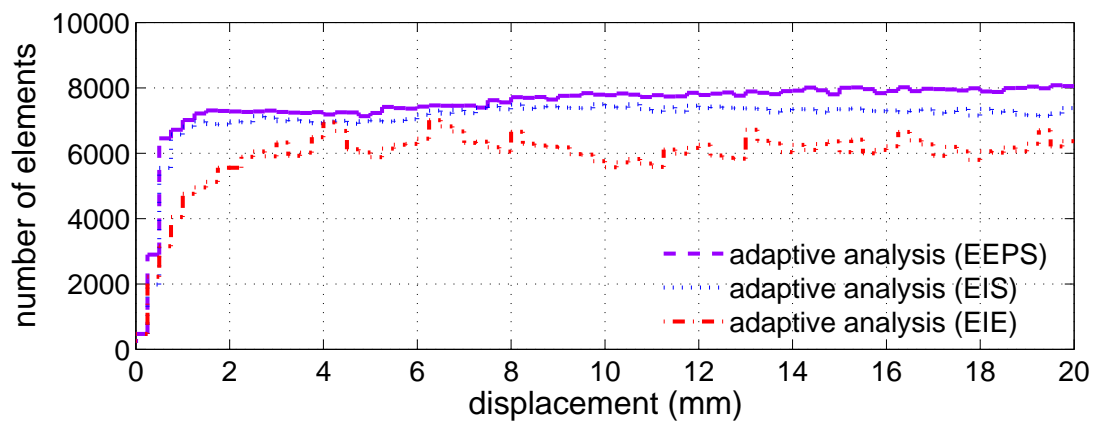


Figure 4.10: Number of elements during the adaptive analysis.

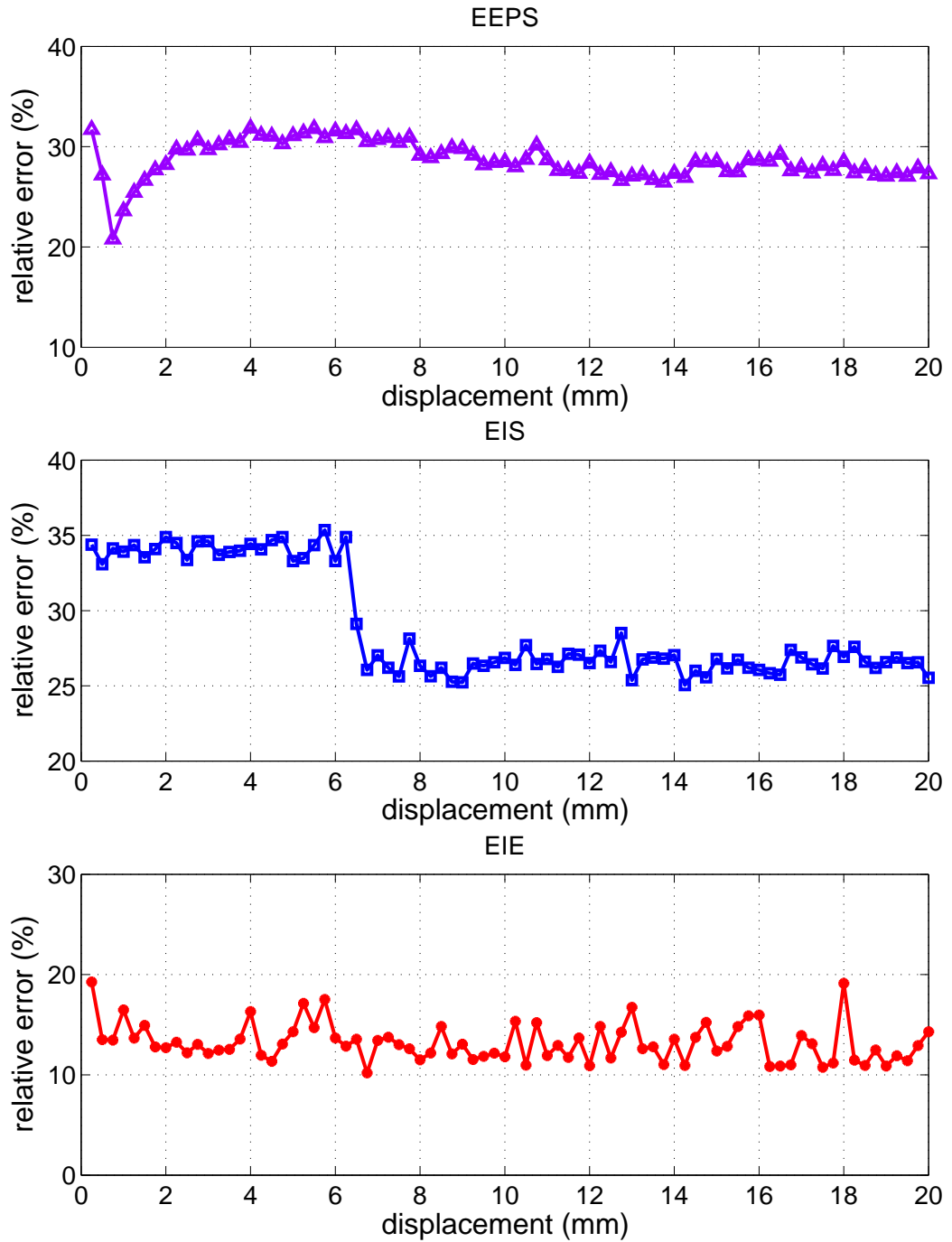


Figure 4.11: Error histories during the adaptive analysis.

Effect of element type

In order to compare the performance of quadrilateral and triangular meshes for extrusion simulations, the results, obtained by using a quadrilateral mesh and a triangular mesh are shown in Figure 4.12. As can be seen in Figure 4.12 and 4.13, the triangular mesh yields unrealistic high plastic strains at the upper-right corner. In addition, it can be seen in Figure 4.13 that the triangular mesh results in the zigzags of the lower deformed boundary. Figure 4.14 shows the discretization error during the adaptive simulation. The number of elements which are used for the adaptive analysis are plotted in Figure 4.15.

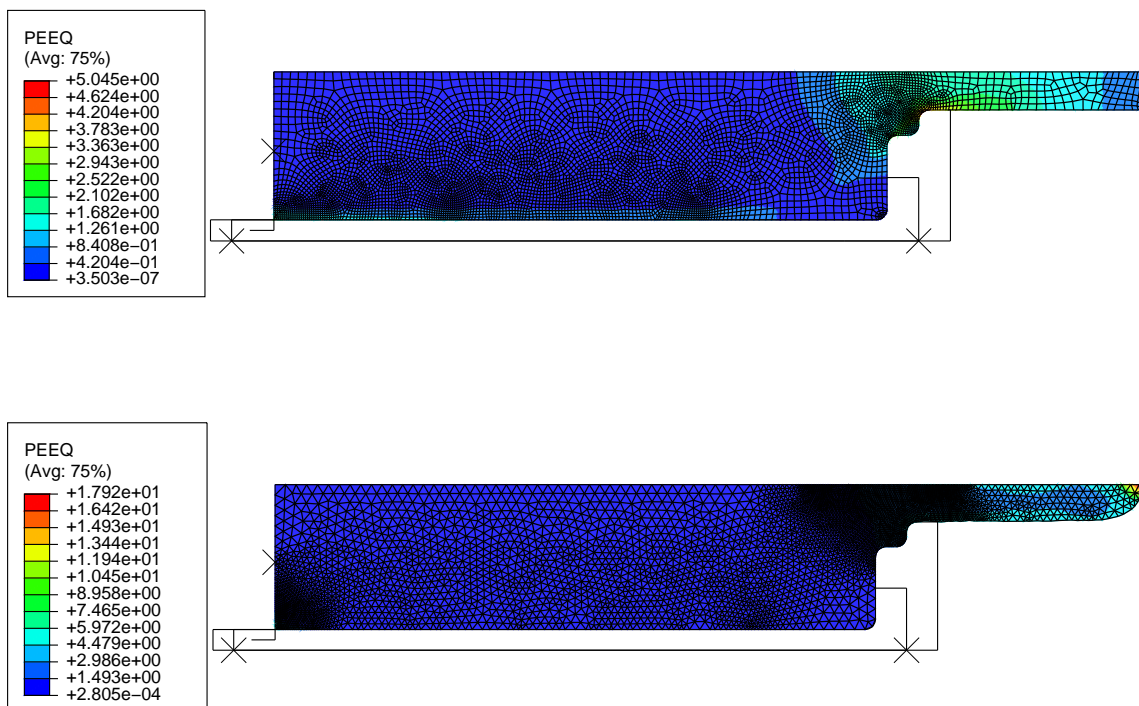


Figure 4.12: Adapted meshes for extrusion simulation. Upper: quadrilateral mesh; Lower: triangular mesh.

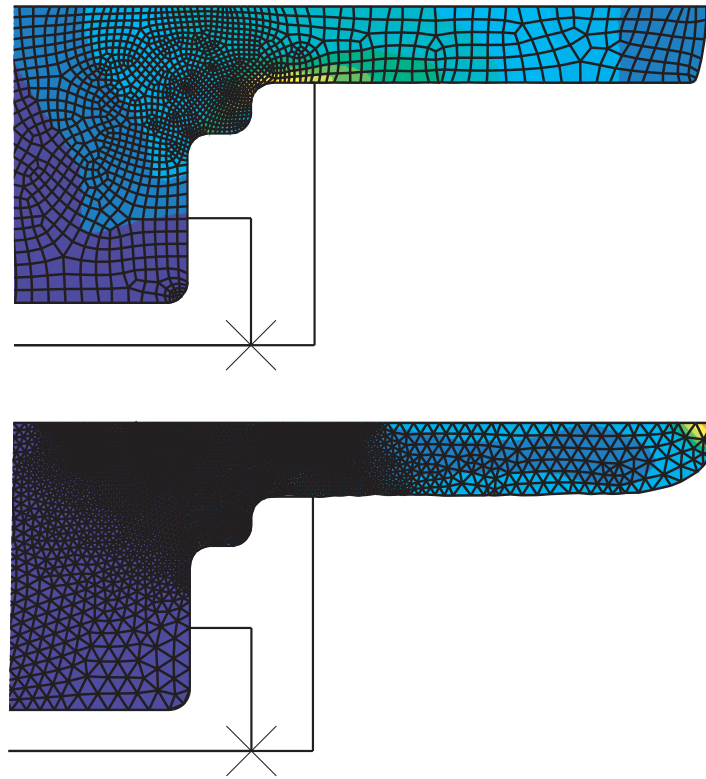


Figure 4.13: Comparison on quadrilateral and triangular meshes.

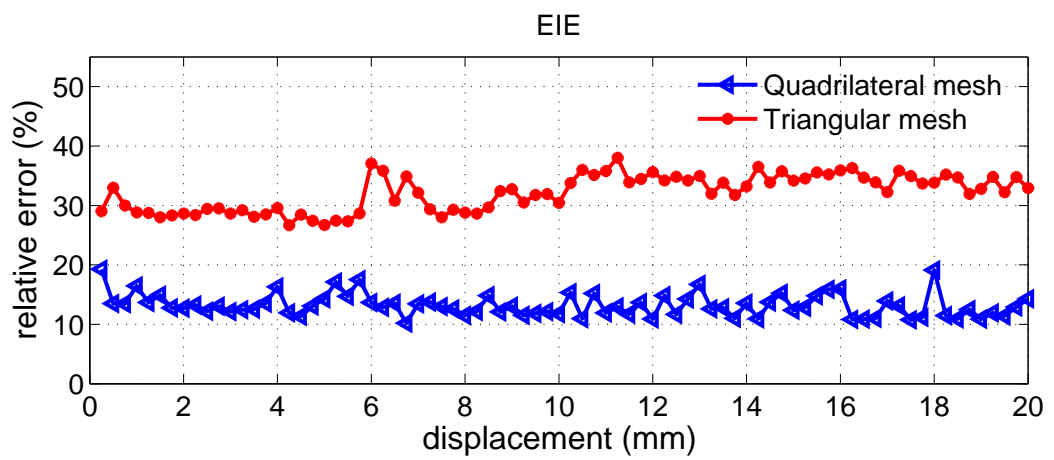


Figure 4.14: Error histories during the adaptive analysis.

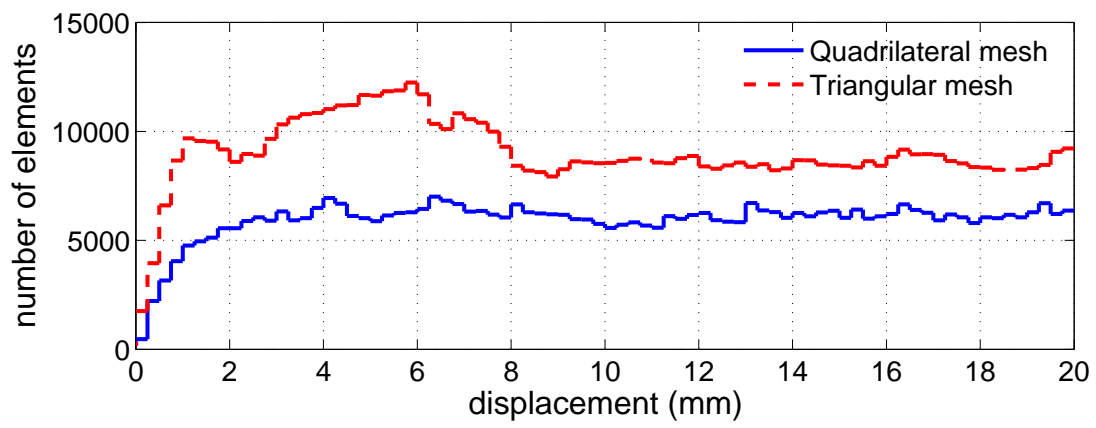


Figure 4.15: Number of elements during the adaptive analysis.

The second extrusion example is a backward extrusion. Figure 4.16 shows the initial mesh and boundary conditions. For the adaptive simulation, the element sizes $h_{min} = 0.8$ mm and $h_{max} = 10$ mm are specified. The adapted meshes and the distribution of the equivalent plastic strain during the process are given in Figure 4.17.

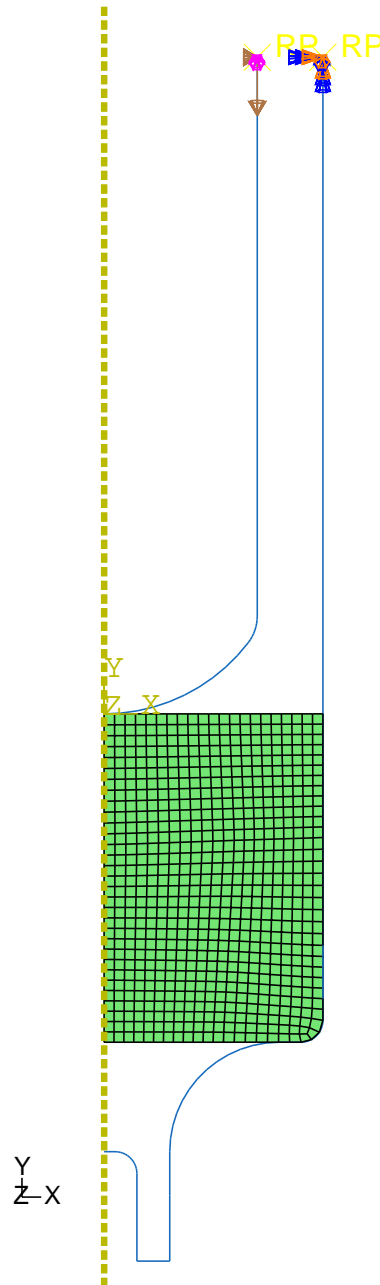


Figure 4.16: The initial mesh and boundary conditions for backward extrusion simulation.

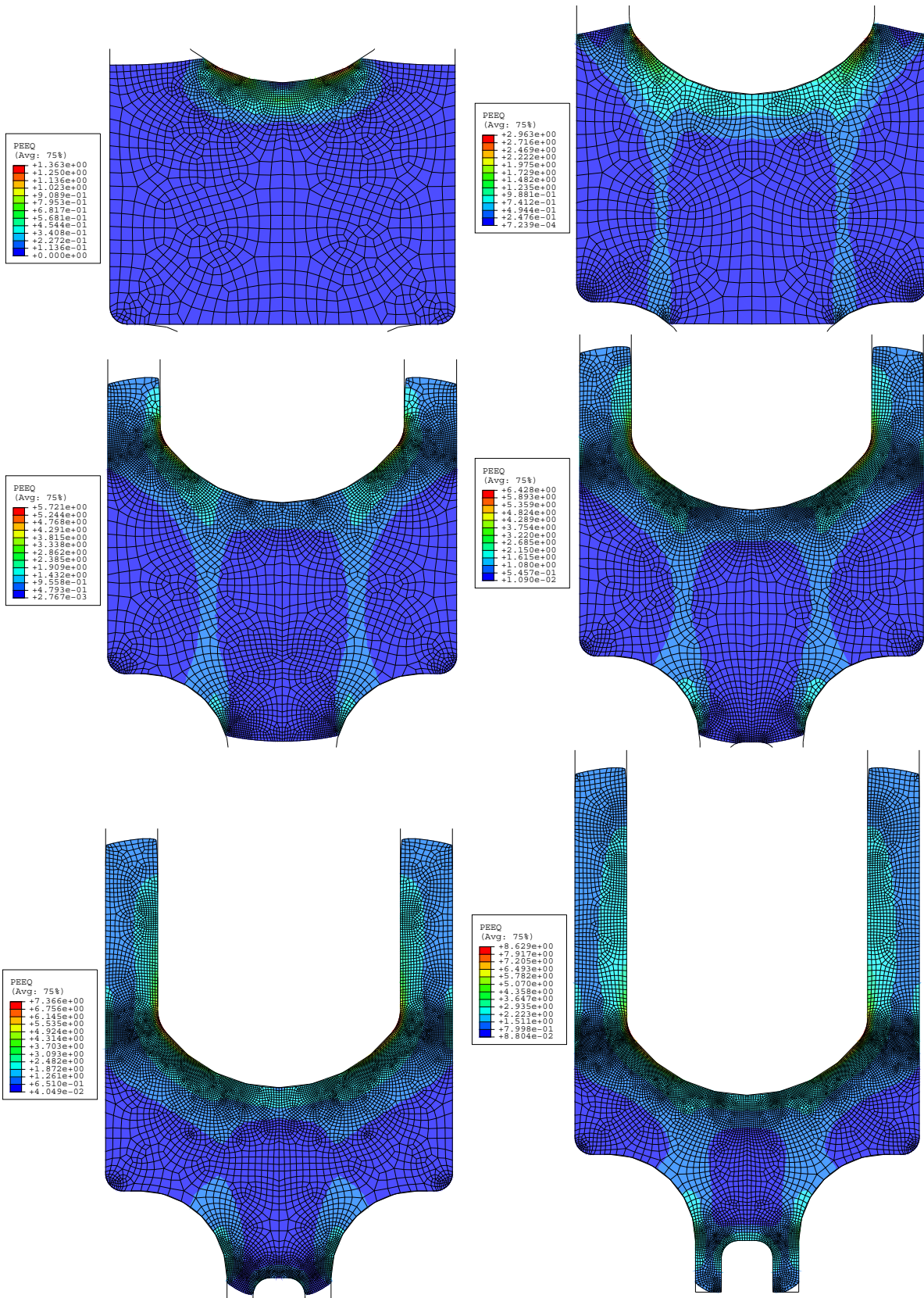


Figure 4.17: Adaptive remeshing for backward extrusion simulation.

4.6.2 Cutting simulation

Metal cutting is one of the most common manufacturing processes, which cuts the material to achieve the desired geometry. When the cutting tool advances into the workpiece, the workpiece material is separated into two parts and the chip is formed. Hence, a chip separation criterion and a mesh separation approach are needed to model the chip formation.

There are two types of chip separation criteria: geometrical and physical (ABAQUS-Manual). Usually, geometrical criteria are employed for predefined node debonding techniques. The criteria are defined by geometrical parameters, such as the distance between the front node and the cutting tool. When the distance is less than a prescribed value, the bonded nodes are separated. Physical criteria are based on the physical behavior of the material, such as critical stress states and equivalent plastic strain. When the physical parameter exceeds a critical value, material failure occurs.

Several numerical methods can be used to model the chip formation in finite element simulation (Xie, 2004). Element elimination techniques eliminate the failure element when the failure criteria are reached. Node debonding techniques separate the mesh by debonding the tied nodes, however the path of crack growth has to be predefined. In contrast to node debonding, node splitting techniques separate two neighboring elements by creating new nodes. In the context of cutting simulation, adaptive remeshing techniques can also be employed to realize chip formation. The advantage of remeshing techniques is, that no chip separation criterion is required, the chip is modelled by mesh deformation. Since the material undergoes extremely large deformations in metal cutting simulations, the distorted mesh has to be updated frequently.

In this work, we employ an adaptive remeshing technique to model the chip formation. The initial mesh and boundary conditions are shown in Figure 4.18. Johnson-Cook material model with adiabatic heating is used for the simulation (Hortig and Svendsen, 2008).

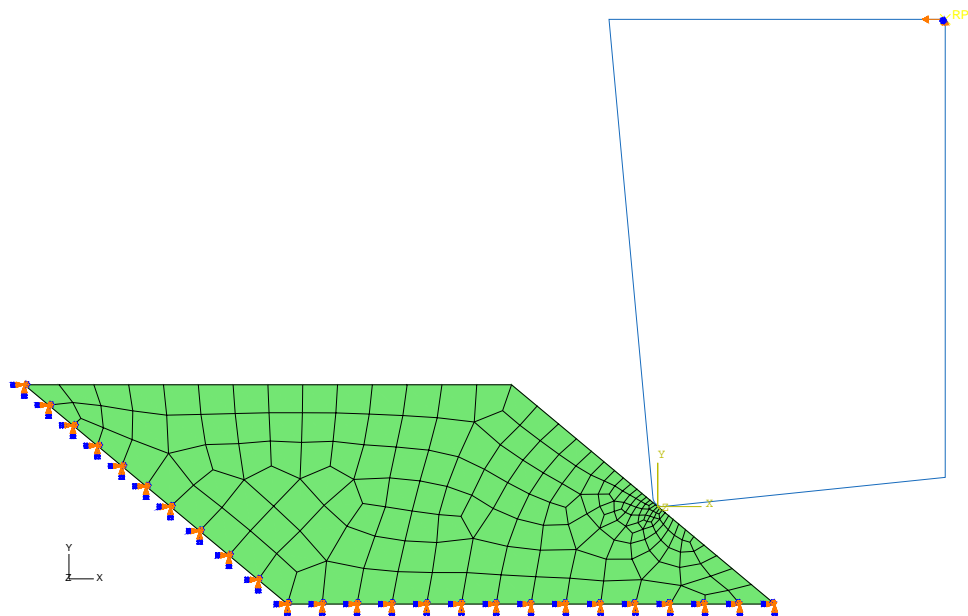


Figure 4.18: The initial mesh and boundary conditions for high speed cutting (Hortig and Svendsen, 2008).

The results of the adaptive simulation are reported in Figure 4.19. It can be observed that several shear bands developed in the chip. The mesh is refined with the help of hanging nodes.

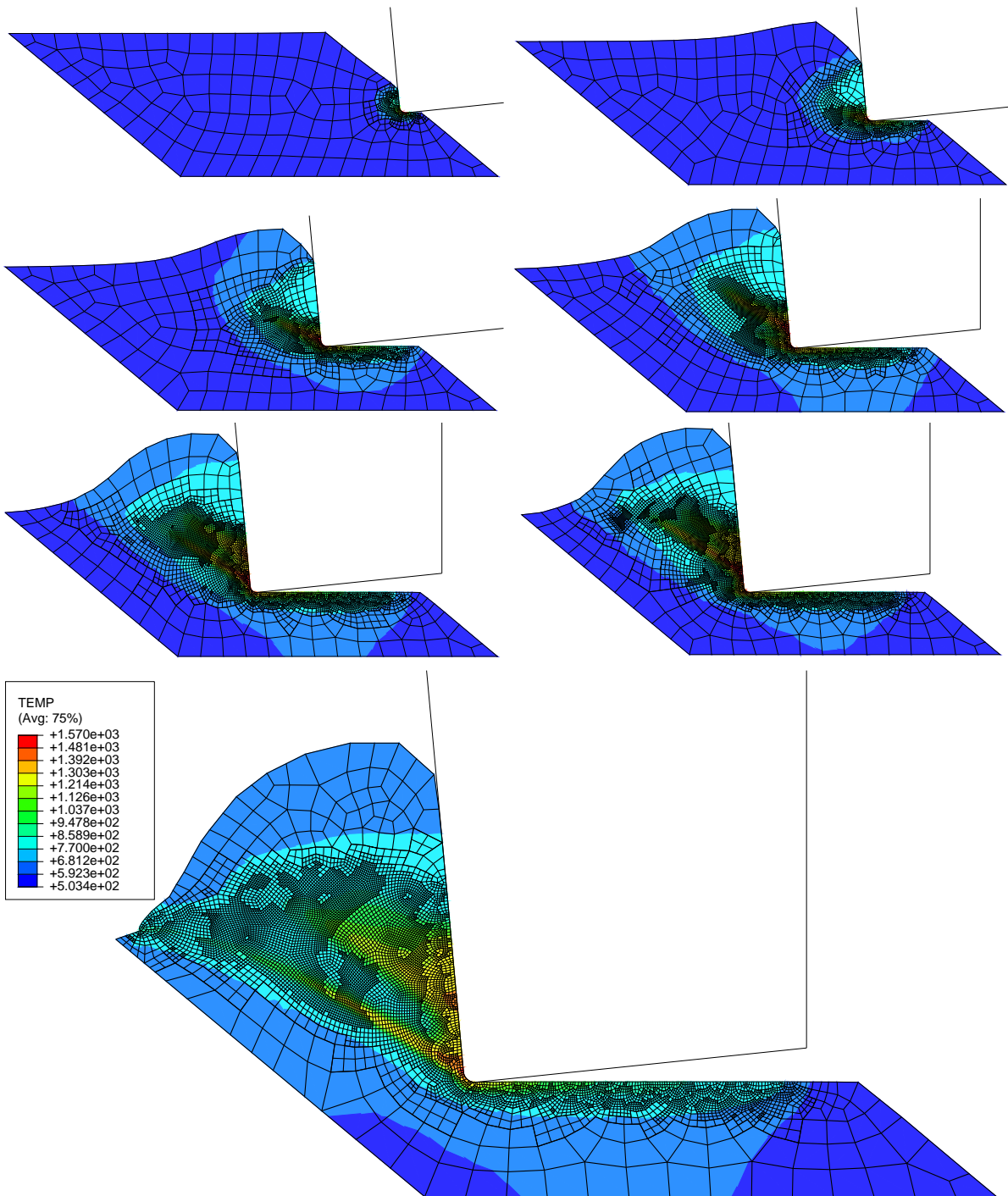


Figure 4.19: Adaptive remeshing for high speed cutting.

Effect of mesh coarsening

To investigate the effect of mesh coarsening, two groups of simulations are carried out. In the first group, the mesh is updated completely according to the desired mesh density field. Here, mesh refinement is performed if the current element size is greater than the desired element size and mesh coarsening is performed if the current element size is less than the desired element size. In the second group, the mesh coarsening function in our mesh generation scheme is turned off. As can be seen in Figure 4.20 (Nel: number of elements; Nnd: number of nodes; Nhnd: number of hanging nodes), both cases yield a similar temperature distribution, whereas the second case yields more elements and nodes due to lack of mesh coarsening. Therefore, mesh coarsening is proven to be helpful to obtain a certain solution accuracy with less computational costs. In addition, it is of interest to note that the number of hanging nodes in the first case is higher than that of the second case. One possible reason is, that mesh coarsening makes the new mesh optimal, the gradient of mesh size is greater than that without mesh coarsening. Thus, more hanging nodes are required, to handle mesh transition between different mesh sizes.

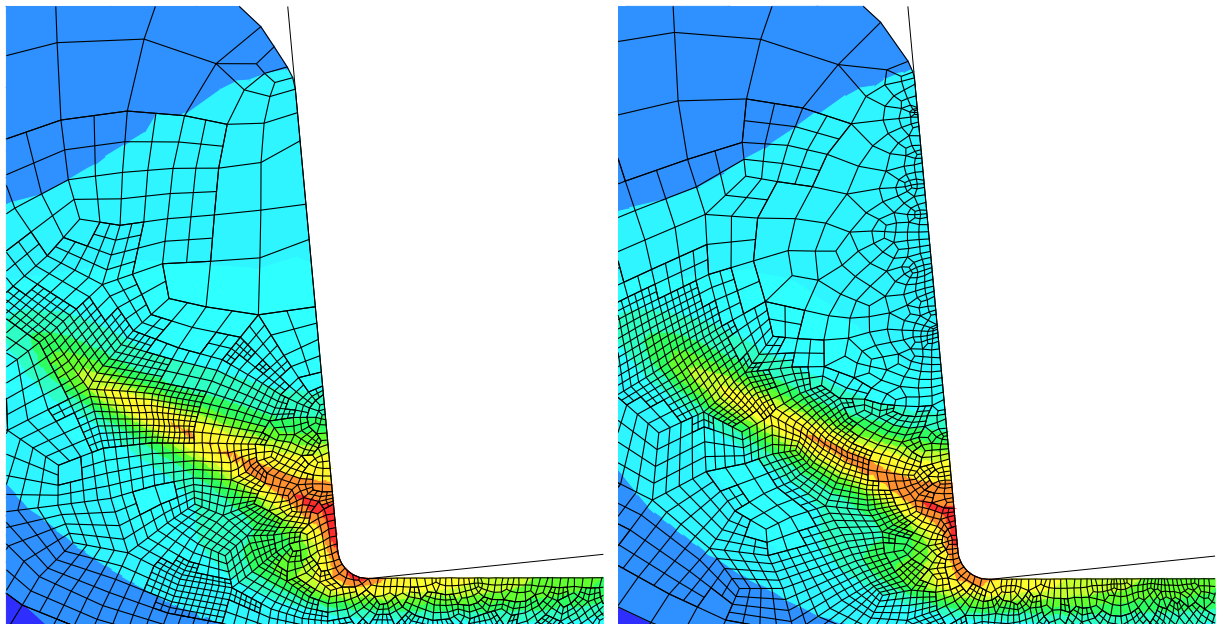


Figure 4.20: Effect of mesh coarsening. Left: with coarsening (Nel = 2655, Nnd = 2988, Nhnd = 492); Right: without coarsening (Nel = 3248, Nnd = 3602, Nhnd = 428).

Comparison on quadrilateral and triangular meshes

The performance of quadrilateral and triangular meshes for adaptive simulation of metal cutting is investigated in this part. Figure 4.21 shows the distribution of temperature.

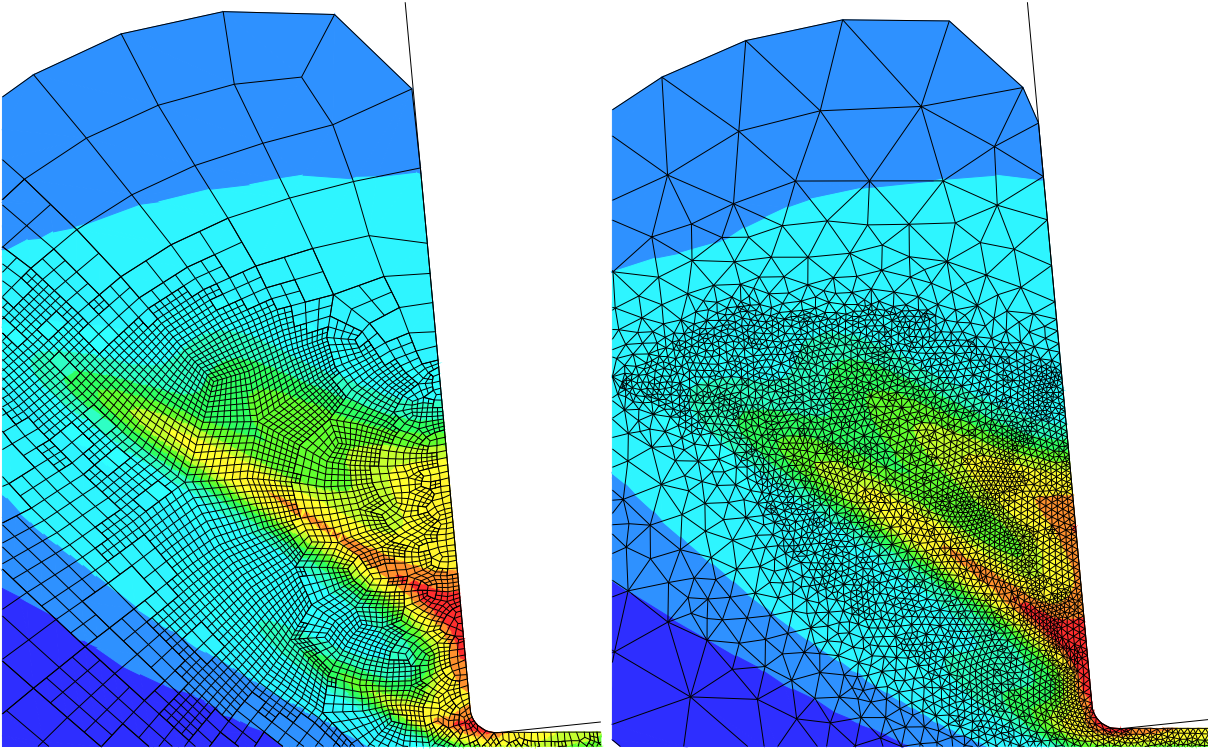


Figure 4.21: Comparison on quadrilateral and triangular meshes. Left: quadrilateral mesh ($N_{el} = 5732$, $N_{nd} = 6296$, $N_{hnd} = 875$); Right: triangular mesh ($N_{el} = 10049$, $N_{nd} = 5147$).

It can be observed that both, quadrilateral and triangular meshes lead to similar results. The number of degree of freedom during the adaptive simulation is plotted in Figure 4.22.

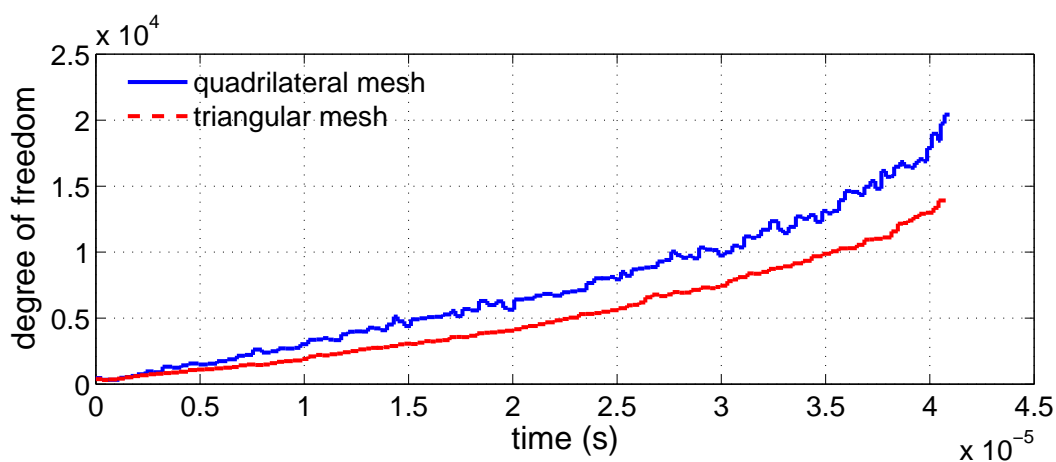


Figure 4.22: Number of degree of freedom during the adaptive simulation.

The total amount of computational costs for error estimation & mesh generation (ErrorE & MeshG), searching & mapping and that for the FE solver are illustrated in Figure 4.23.

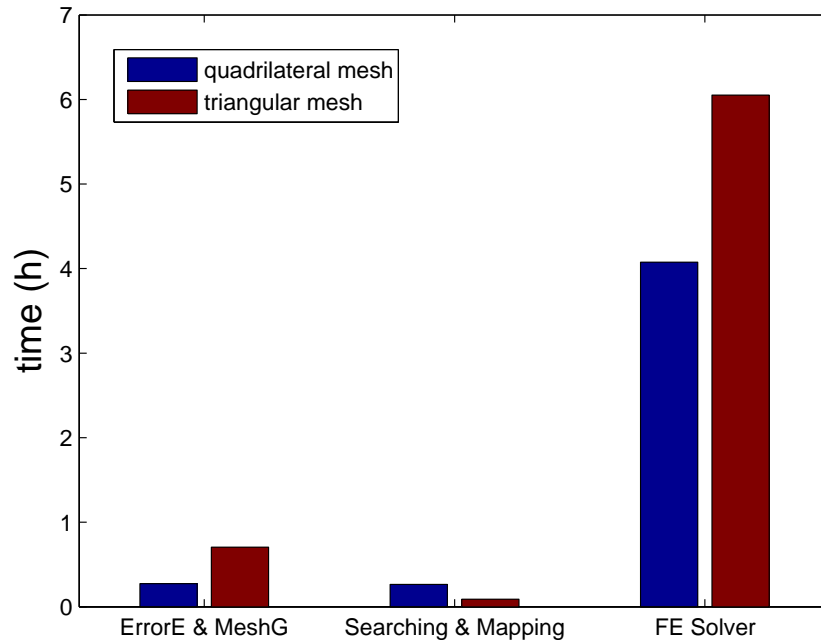


Figure 4.23: Comparison on computational cost.

It can be seen that, although the number of degrees of freedom in a quadrilateral mesh is higher than that in a triangular mesh, the CPU time of finite element computation for a quadrilateral mesh is less, than that for the triangular mesh. In addition, we note that the procedure of error estimation and mesh generation for the quadrilateral mesh is faster. This advantage benefits from the hierarchical mesh generation technique, which is much faster than conforming mesh generation such as advancing front or Delaunay mesh generation techniques. Currently, two different searching algorithms are employed for quadrilateral and triangular meshes. The searching algorithm used for the quadrilateral mesh is slower due to the larger searching region, therefore the computational costs for the quadrilateral mesh is more expensive than that for the triangular mesh.

Effect of mapping algorithm

Using this metal cutting example, the mapping algorithms based on various recovery techniques are investigated. Nodal averaging (NA), superconvergent patch recovery (ZZ) and best-fit point based local extrapolation (BF) techniques are employed to obtain improved solutions before mapping them from the old to the new mesh. Figure 4.24 shows the distribution of temperature for two groups of results. The results at cutting tool displacement of 0.61 mm are displayed in Figure 4.24(a)-(c) and the results at tool displacement of 0.76 mm are shown in Figure 4.24(d)-(f). These three columns show the results based on the NA (left), ZZ (middle) and BF (right) mapping algorithms, respectively.

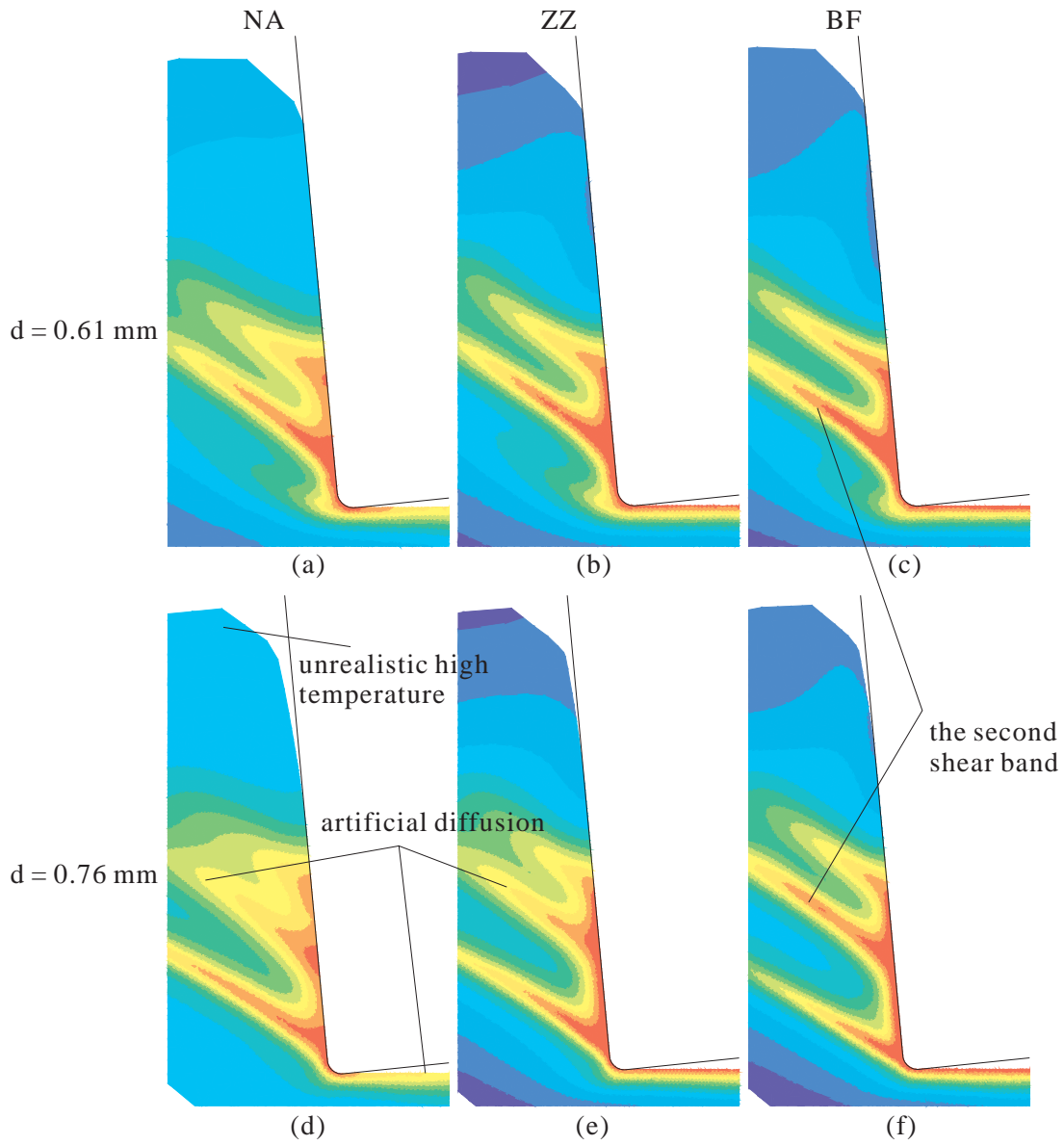


Figure 4.24: Effect of mapping algorithm. Results at cutting tool displacement of 0.61 mm (a)-(c) and the results at tool displacement of 0.76 mm (d)-(f). The three columns show the results based on the NA (left), ZZ (middle) and BF (right) mapping algorithms, respectively.

As can be observed in Figure 4.24(a)-(c), the development of the second shear band in these three cases is quite similar. However, it can be seen in Figure 4.24(d), at a later stage, after about 30 remeshing and mapping steps, the NA mapping algorithm leads to artificial diffusion of the second shear band. The temperature near the horizontal machined surface also decreases due to the error in the NA mapping algorithm. In addition, compared to Figure 4.24(e) and (f), the NA algorithm leads to unrealistic high temperature in the upper region of the workpiece. In Figure 4.24(e), we note that the ZZ mapping algorithm also results in numerical diffusion of the second shear band, but this algorithm shows a good performance in mapping the solution near the horizontal boundary. It is of interest to note that the second shear band in Figure 4.24(f) is the most similar to the second shear band in Figure 4.24(a)-(c), which demonstrates the good performance of the BF mapping algorithm.

4.6.3 Forging simulation

Forging is a manufacturing process which is used to shape the material by using localized compressive forces. In this section, we first consider a gear ring forging problem. The geometry and boundary conditions are shown in Figure 4.25. The material behavior is assumed to be linear isotropic hardening.

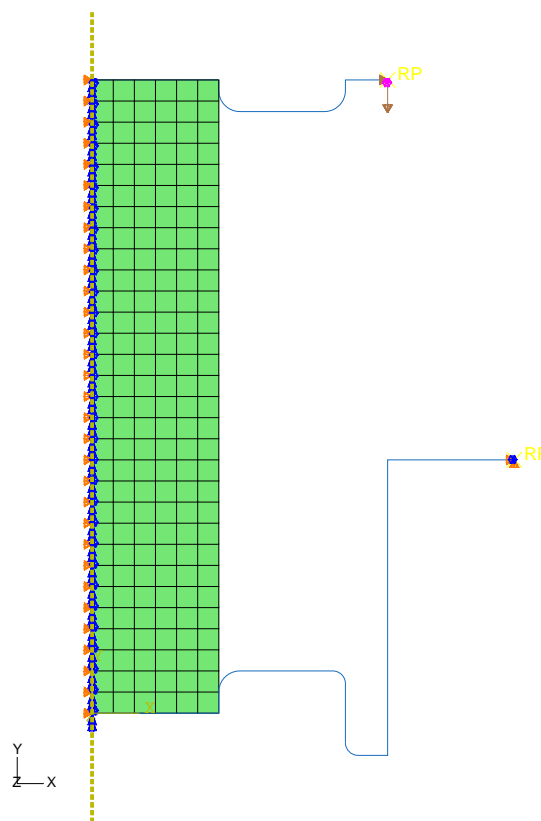


Figure 4.25: The initial mesh and boundary conditions for the gear ring forging simulation.

The EIE error estimator is employed to drive the adaptive remeshing. Figure 4.26 shows the adapted meshes at various stages. At an early stage, the material is compressed. It can be seen that the mesh near the round corner is refined due to high energy error.

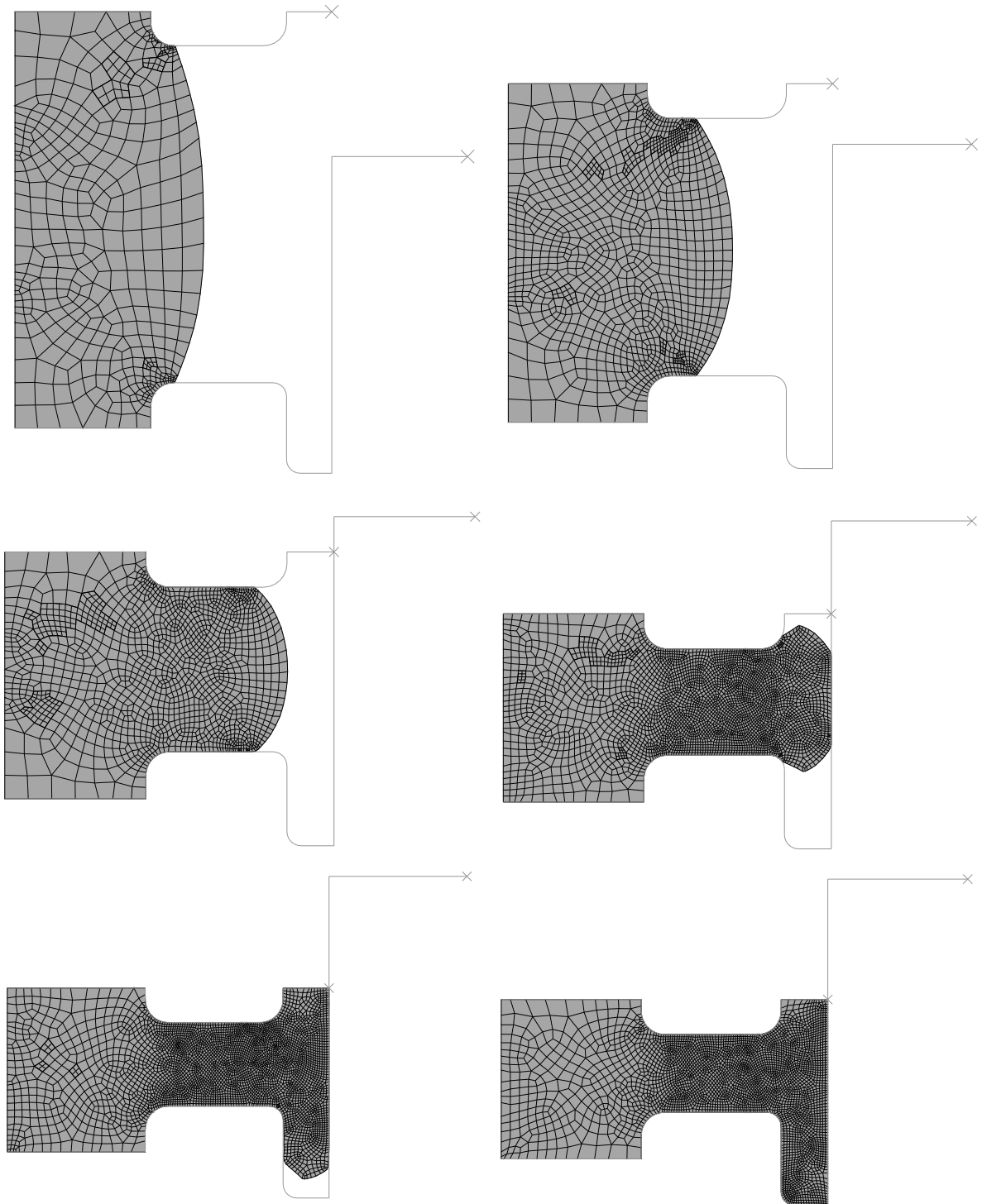


Figure 4.26: Adaptive remeshing for gear forging simulation.

At later stages, the material flows towards the right side. The gradient of strain rate is quite high due to the friction between the die and material flow, therefore the mesh is further refined. The distribution of the equivalent plastic strain in the workpiece at the final stage is shown in Figure 4.27. It can be observed that the equivalent plastic strain near the rigid tool is very high.

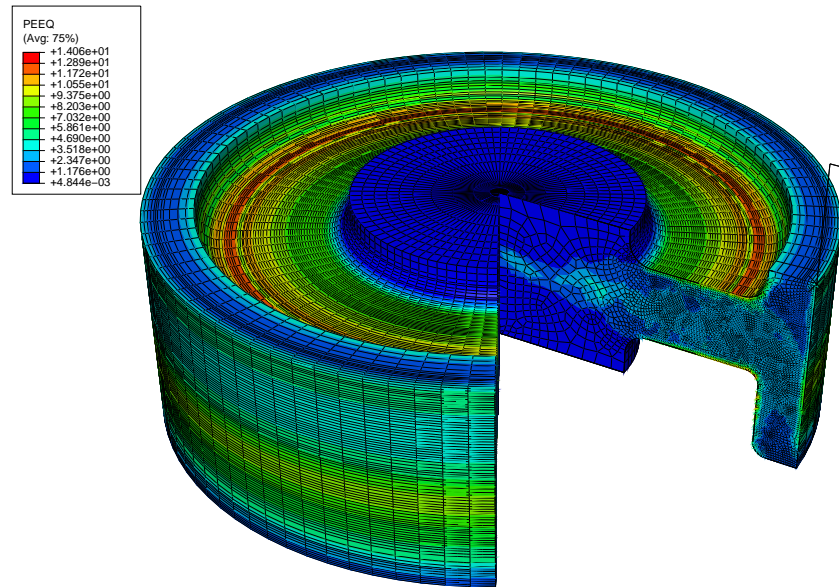


Figure 4.27: Distribution of equivalent plastic strain in the workpiece.

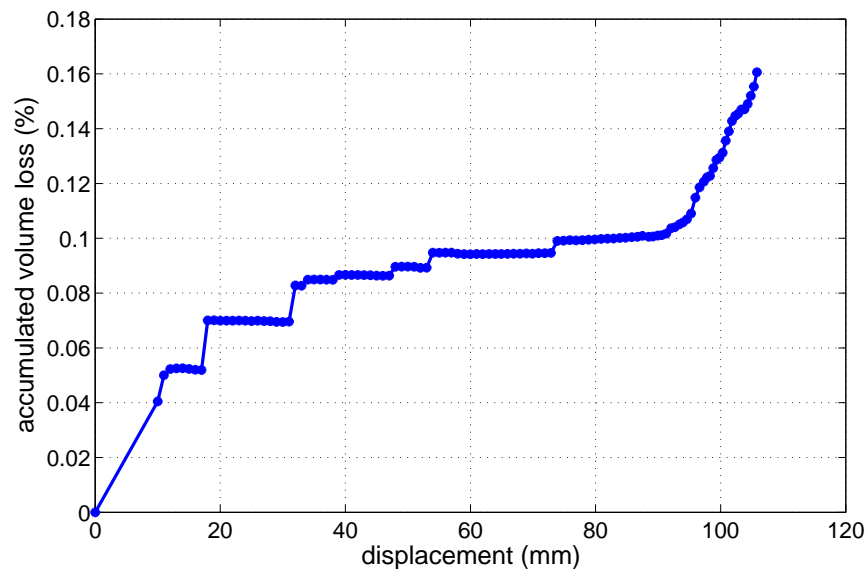


Figure 4.28: Accumulated volume loss during the adaptive simulation.

On the other side, the adaptive remeshing procedure results in more elements in contact zones, which reduces the interference between the mesh and the round rigid tool. Figure 4.28 displays the accumulated loss of volume during the adaptive simulation. It can be seen that the total loss of volume at the final stage is only 0.161%. The volume loss is related to the

remeshing steps and element size near the curved die. In general, the more remeshing steps, the less the volume loss since frequent remeshing makes the adapted mesh optimally match the curved die. The volume loss can also be decreased by fitting the mesh to the curved die with smaller elements.

The second forging example is considered, using geometrically complex dies. The simulation involves large plastic strains near the punch and the die. The initial mesh and boundary conditions are shown in Figure 4.29. The rigid tool moves vertically. The EIS error estimator is used to determine the adapted mesh density. Figure 4.30 shows the adapted mesh and the distribution of equivalent plastic strain according to different displacements of the punch. It is noticed that the mesh in contact with the rigid tool is refined.

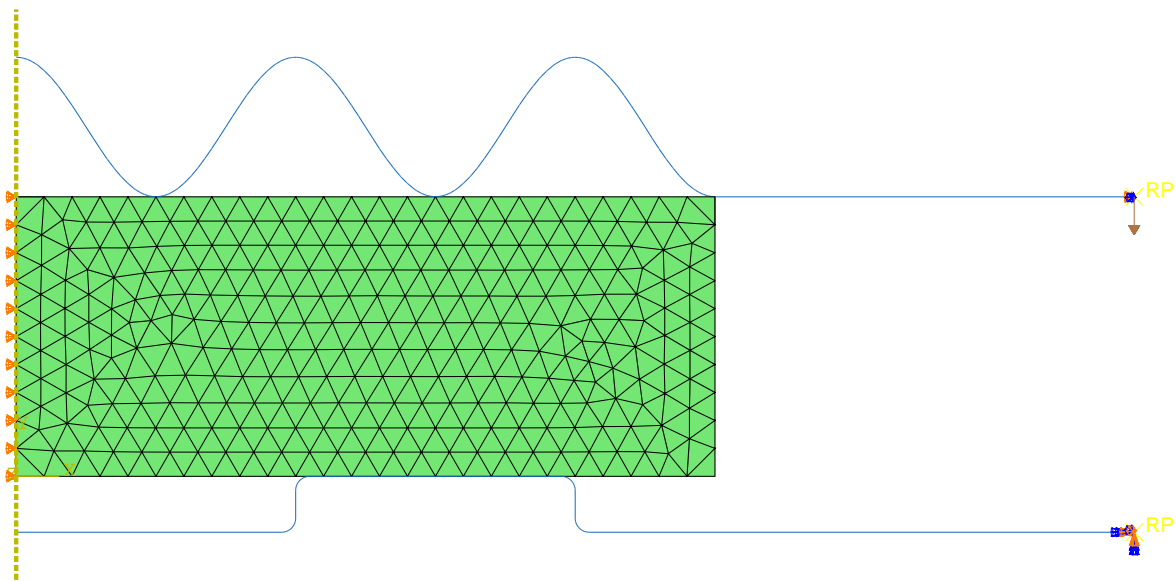


Figure 4.29: The initial mesh and boundary conditions for cold forging simulation.

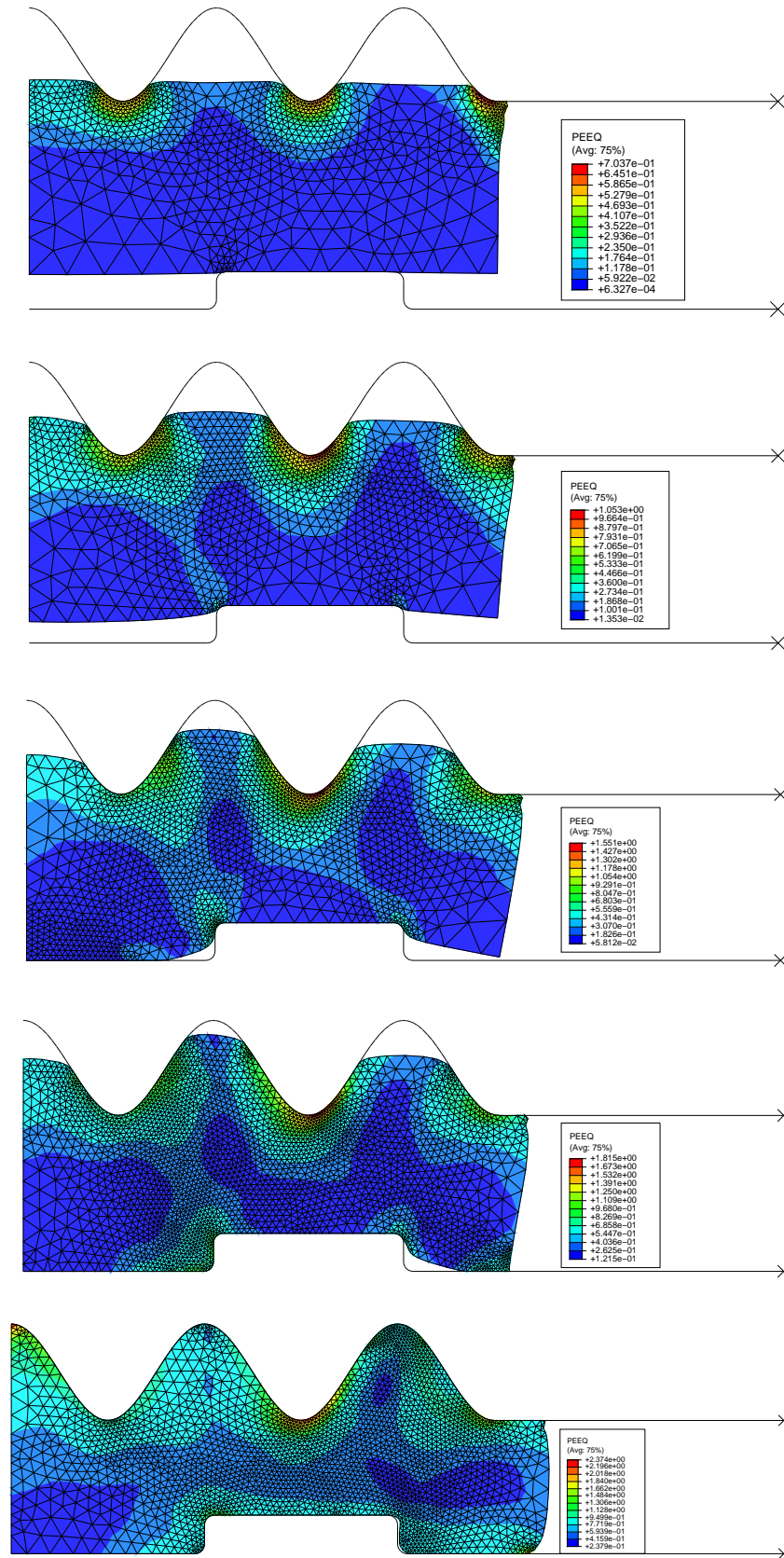


Figure 4.30: Adaptive remeshing for cold forging simulation.

4.6.4 Rolling simulation

Rolling is a manufacturing process used to transform material into a form by rotating rollers. In this example, rolling of a thick plate is simulated. Due to the symmetry of the model, a half model is considered for plane strain analysis. The geometry and boundary conditions are shown in Figure 4.31.

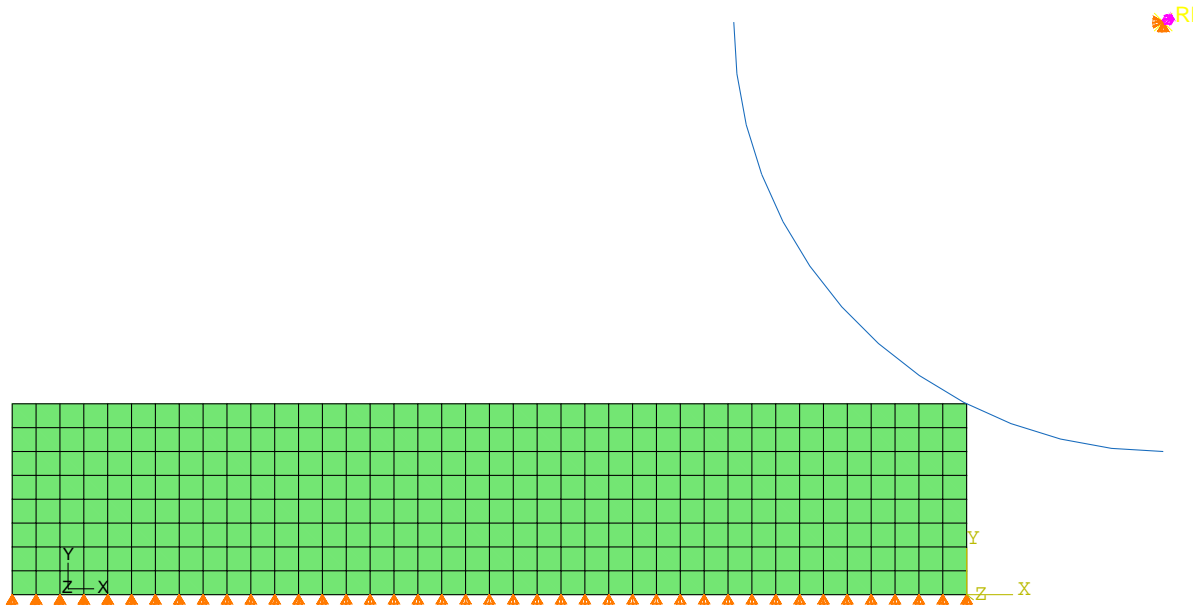


Figure 4.31: The initial mesh and boundary conditions for the rolling simulation.

The material behavior is assumed to be linear isotropic hardening. The roller is rotated counterclockwise. Coulomb friction is assumed between the roller and the plate. The plate is imposed by an initial velocity in the x -direction. Then it will be pulled through the roll stand, by means of friction only.

The EIS error estimator is employed to analyze the discretization error and calculate the optimal mesh density for a prescribed accuracy. In the adaptive simulation, the maximum element size $h_{max} = 8$ mm and the minimum element size $h_{min} = 0.2$ mm are imposed. The adapted meshes are shown in Figure 4.32. Here, the left column shows the distribution of incremental strain and the right column shows the distribution of the mesh density. By comparing the distribution of incremental strain and the adapted mesh, we note that the EIS error estimator is very effective in catching the error in the incremental strain.

The number of elements, used during the adaptive simulation is shown in Figure 4.33. The discretization errors in the simulation are shown in Figure 4.34. It can be seen that the discretization error is drastically decreased while the total number of elements is increased at early stages.

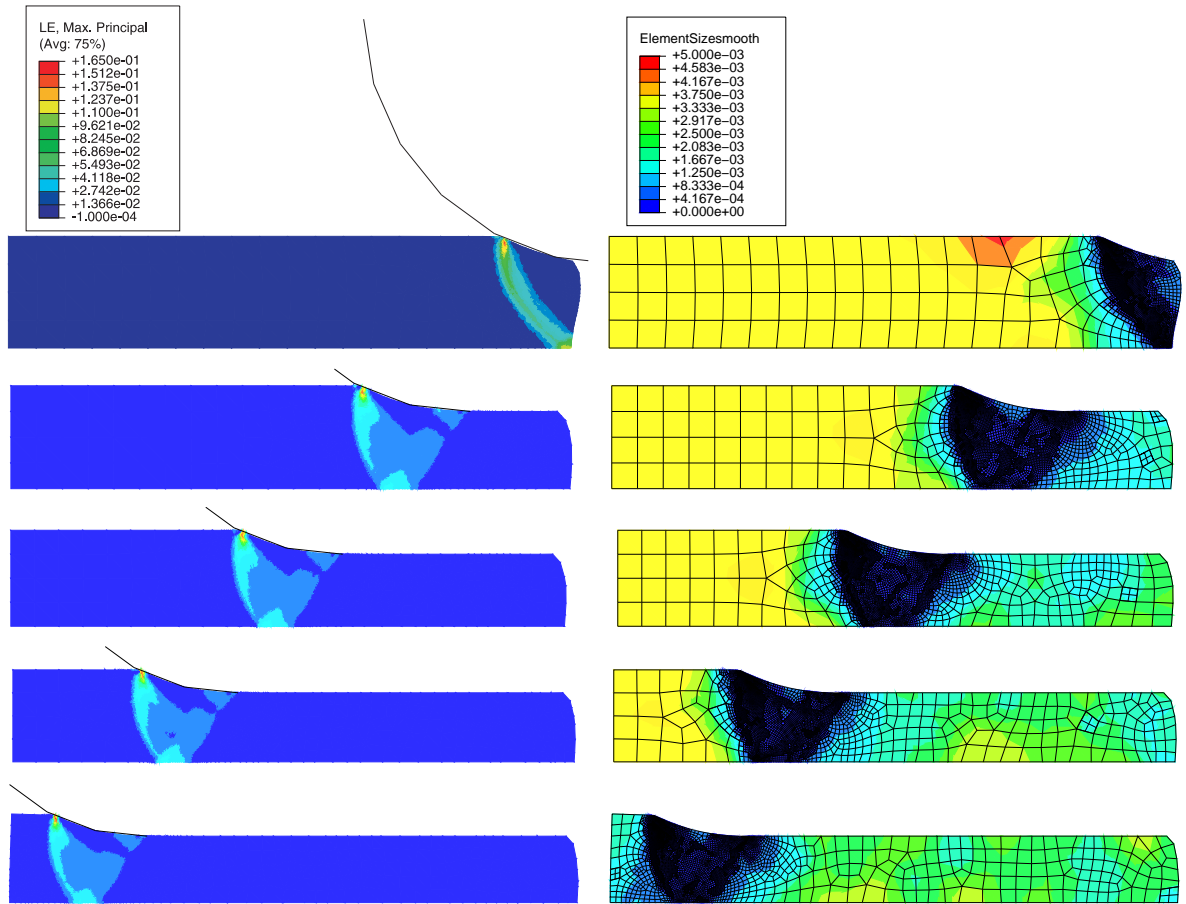


Figure 4.32: Adaptive remeshing for rolling simulation.

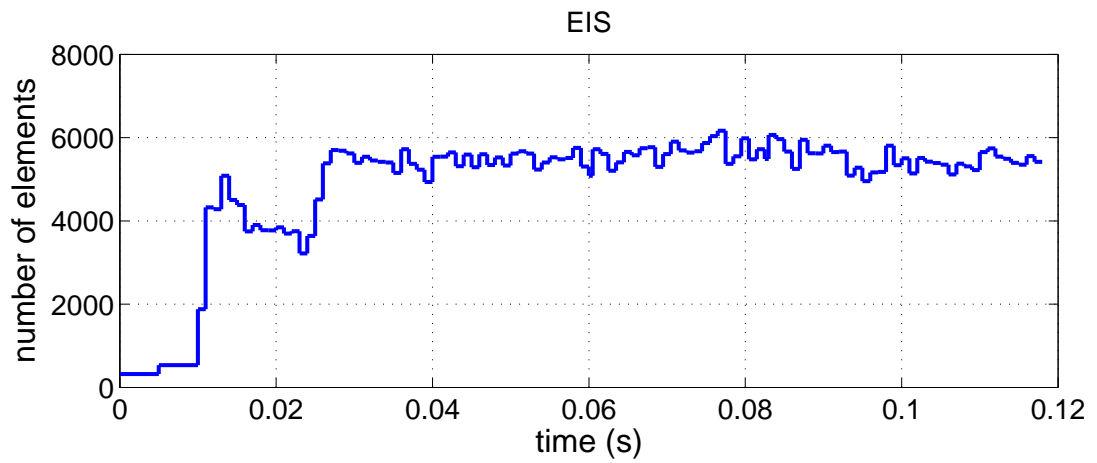


Figure 4.33: Number of elements during the adaptive analysis.

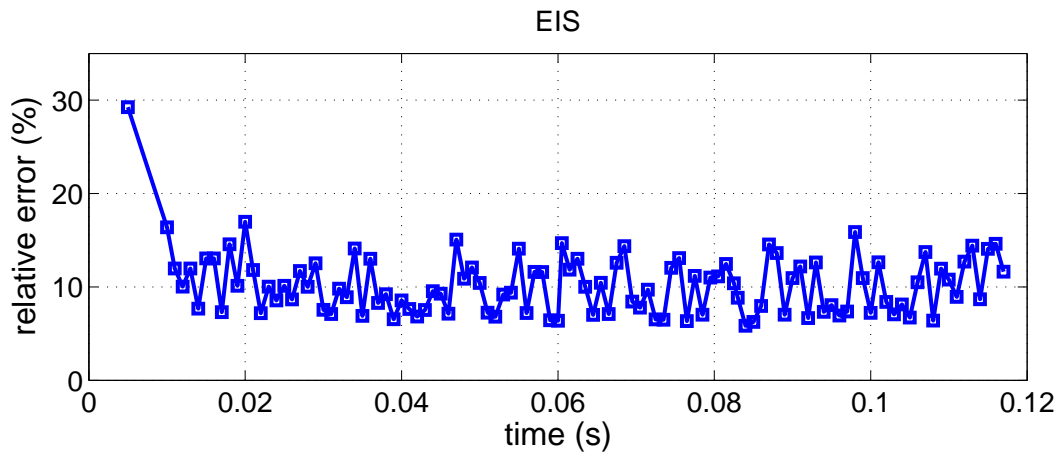


Figure 4.34: Error histories during the adaptive analysis.

4.7 Adaptive remeshing for large deformation problem with damage

As discussed in §4.6.2, when material failure takes place, element elimination techniques can be employed to remove the failure elements. In this section, we discuss the shear failure criteria and an element elimination scheme. An example of a uniaxial tensile test is presented to demonstrate the performance of the adaptive remeshing with the additional element elimination procedure.

4.7.1 Shear failure model

The shear failure model (ABAQUS-Manual) is based on the equivalent plastic strain at integration points. When the equivalent plastic strain exceeds the strain at failure $\bar{\varepsilon}_f^{pl}$, the damage parameter ω exceeds 1 and material failure occurs. The corresponding stress components are set to zero and the material point has no contribution to the elementary stiffness matrix. If all the material points at an element fail, the element is eliminated from the mesh. The damage parameter, ω , is defined as:

$$\omega = \frac{\sum \Delta \bar{\varepsilon}^{pl}}{\bar{\varepsilon}_f^{pl}}, \quad (4.25)$$

where $\Delta \bar{\varepsilon}^{pl}$ is an increment of the equivalent plastic strain and $\bar{\varepsilon}_f^{pl}$ is the strain at failure. The increments of the equivalent plastic strain are summarized over the whole analysis.

4.7.2 Damaged element elimination procedure

If failure criteria are met, the damaged elements have to be eliminated in order to define the new geometry before remeshing takes place. The procedure includes the following steps:

- 1) Delete the damaged element connectivity;
- 2) Delete the nodes not connected to the remaining elements;
- 3) Renumber the nodes and elements and renew the element connectivity.

4.7.3 Tensile test

In this example, a rectangular specimen under plane strain condition is considered. The bottom of the specimen is fixed and on the top of the specimen a displacement is imposed. Two different mesh generation schemes are employed to renew the mesh for this example. The results for the simulation with only refining are shown in Figure 4.35 and the results for a complete remeshing are shown in 4.36. It can be seen that the damage localizes inside two diagonal shear bands, then the crack propagates along one of the shear bands until the specimen is broken up. Note that the orientations of crack propagation in Figure 4.35 and 4.36 are different due to mesh dependence.

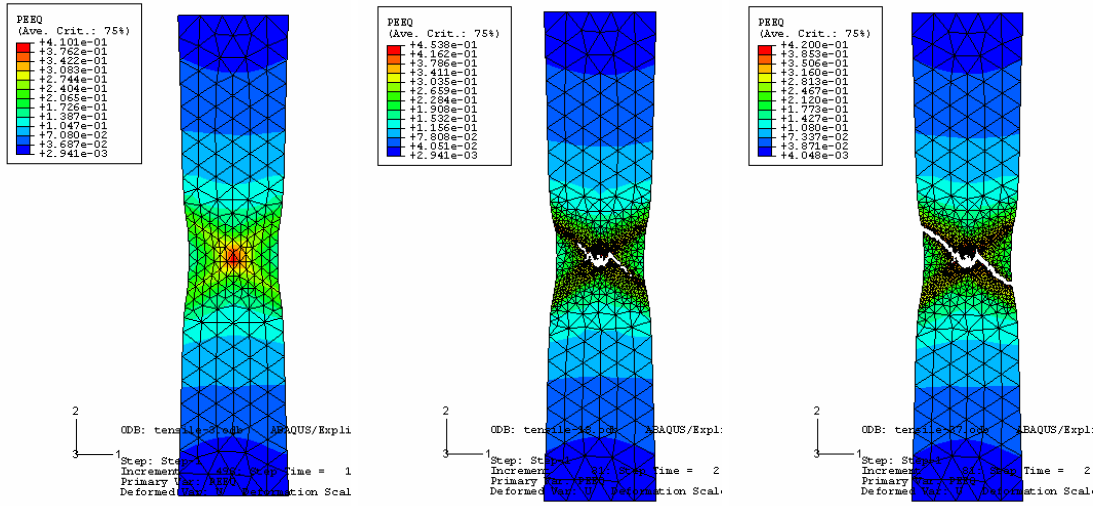


Figure 4.35: Uniaxial tensile test with adaptive refining (no mesh coarsening takes place).

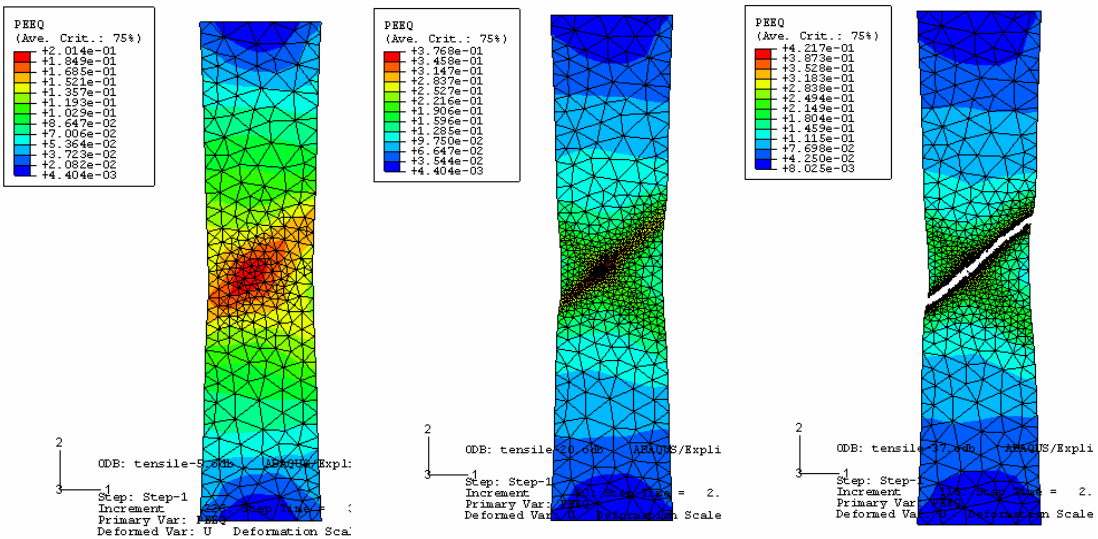


Figure 4.36: Uniaxial tensile test with adaptive remeshing (refinement and coarsening applied).

4.8 Conclusions

An adaptive remeshing strategy for metal forming simulation has been presented in this chapter. Each of the ingredients including error estimator, mapping algorithm, remeshing technique and element type in adaptive metal forming simulations have been discussed and evaluated. The simulations of four types of manufacturing processes such as extrusion, cutting, forging and rolling have been carried out to validate the proposed adaptive remeshing procedure.

In the applications, bilinear quadrilateral elements seem to be more efficient and robust than linear triangular elements. In the adaptive simulation of metal cutting, numerical comparison shows that the mapping algorithm based on local extrapolation technique (BF) transfers state variables with the least numerical diffusion. Mesh coarsening included in the adaptive remeshing procedure is shown to be able to reduce computational costs without decreasing the solution accuracy. For large deformation problems with damage, the adaptive remeshing, including a damaged element elimination procedure, is shown to be efficient.

References

ABAQUS-Manual, v6.7.

- Aiffa, M., Flaherty, J., A geometrical approach to mesh smoothing, *Comput. Methods Appl. Mech. Engrg.*, Volume 192, pp. 4497–4514, 2003.
- Ainsworth, M., Demkowicz, L., Kim, C.-W., Analysis of the equilibrated residual method for a posteriori error estimation on meshes with hanging nodes, *Comput. Methods Appl. Mech. Engrg.*, Volume 196, pp. 3493–3507, 2007.
- Ainsworth, M., Oden, J. T., A unified approach to a-posteriori error estimation using element residual methods, *Numer. Math*, Volume 65, pp. 23–50, 1993.
- Ainsworth, M., Oden, J. T., A posteriori error estimation in finite element analysis, *Comput. Methods Appl. Mech. Engrg.*, Volume 142, pp. 1–88, 1997.
- Amenta, N., Bern, M., Eppstein, D., Optimal point placement for mesh smoothing, *Journal of Algorithms*, Volume 30, pp. 302–322, 1999.
- Araujo, T. D. d., Roehl, D., Martha, L., An adaptive strategy for elastic-plastic two-dimensional finite element analysis, in *European Congress on Computational Methods in Applied Sciences and Engineering*, Barcelona, 2000.
- Babuska, I., Rheinboldt, W., A posteriori error estimates for the finite element method, *Int. J. Numer. Meth. Engng*, Volume 12, pp. 1597–1615, 1978.
- Babuska, I., Strouboulis, T., Gangaraj, S., Upadhyay, C., Pollution error in the h-version of the finite element method and the local quality of the recovered derivatives, *Comput. Methods Appl. Mech. Engrg.*, Volume 140, pp. 1–37, 1997a.
- Babuska, I., Strouboulis, T., Gangargj, S., A posteriori estimation of the error in the recovered derivatives of the finite element solution, *Comput. Methods Appl. Mech. Engrg.*, Volume 150, pp. 369–396, 1997b.
- Babuska, I., Strouboulis, T., Mathur, A., Upadhyay, C., Pollution-error in the h-version of the finite-element method and the local quality of a-posteriori error estimators, *Finite Elements in Analysis and Design*, Volume 17, pp. 273–321, 1994a.
- Babuska, I., Strouboulis, T., Upadhyay, C., A model study of the quality of a posteriori error estimators for linear elliptic problems, *Comput. Methods Appl. Mech. Engrg.*, Volume 114, pp. 307–378, 1994b.
- Babuska, I., Strouboulis, T., Upadhyay, C., Validation of a posteriori error estimators by numerical approach, *Int. J. Numer. Meth. Engng*, Volume 37, pp. 1073–1123, 1994c.
- Babuska, I., Strouboulis, T., Upadhyay, C., A model study of the quality of a posteriori error estimators for finite element solutions of linear elliptic problems, with particular reference to the behavior near the boundary, *Int. J. Numer. Meth. Engng*, Volume 40, pp. 2521–2577, 1997c.
- Babuska, I., Strouboulis, T., Upadhyay, C., Gangaraj, S., A posteriori estimation and adaptive control of pollution error in the h-version of the finite element method, *Int. J. Numer. Meth.*

- Engng, Volume 38, pp. 4207–4235, 1995.
- Babuska, I., Strouboulis, T., Upadhyay, C., Gangargj, S., Computer-based proof of the existence of superconvergence points in the finite element method; superconvergence of the derivatives in finite element solutions of laplace's, poisson's, and the elasticity equations, *Numer Methods Partial Differential Eq*, Volume 12, pp. 347–392, 1996.
- Baeker, M., Roesler, J., Siemers, C., A finite element model of high speed metal cutting with adiabatic shearing, *Computers and Structures*, Volume 2002, pp. 495–513, 2002.
- Balendran, B., A direct smoothing method for surface meshes, in *Proceedings of the Eighth International Meshing Roundtable*, 189–193, South Lake Tahoe, CA, U.S.A., 1999.
- Bank, R. E., Smith, R. K., Mesh smoothing using a posteriori error estimates, *SIAM J. NUMER. ANAL.*, Volume 34, pp. 979–997, 1997.
- Barlow, J., Optimal stress location in finite element models, *Int. J. Numer. Meth. Engng*, Volume 10, pp. 243–251, 1976.
- Barlow, J., More on optimal stress points-reduced integration, element distortions and error estimation, *Int. J. Numer. Meth. Engng*, Volume 28, pp. 1487–1504, 1989.
- Benedetti, A., Miranda, S. d., Ubertini, F., A posteriori error estimation based on the superconvergent Recovery by Compatibility in Patches, *Int. J. Numer. Meth. Engng*, Volume 67, pp. 108–131, 2006.
- Blacker, T., Belytschko, T., Superconvergent patch recovery with equilibrium and conjoint interpolant enhancements, *Int. J. Numer. Meth. Engng*, Volume 37, pp. 517–536, 1994.
- Blacker, T. D., Stephenson, M. B., Paving: a new approach to automated quadrilateral mesh generation, *Int. J. Numer. Meth. Engng*, Volume 32, pp. 811–847, 1991.
- Boroomand, B., Ghaffarian, M., Zienkiewicz, O., On application of two superconvergent recovery procedures to plate problems, *Int. J. Numer. Meth. Engng*, Volume 61, pp. 1644–1673, 2004.
- Boroomand, B., Mossaiby, F., Generalization of robustness test procedure for error estimators. Part II: test results for error estimators using SPR and REP, *Int. J. Numer. Meth. Engng*, Volume 64, pp. 461–502, 2005a.
- Boroomand, B., Mossaiby, F., Generalization of robustness test procedure for error estimators. Part I: formulation for patches near kinked boundaries, *Int. J. Numer. Meth. Engng*, Volume 64, pp. 427–460, 2005b.
- Boroomand, B., Zienkiewicz, O., An improved REP recovery and the effectivity robustness test, *Int. J. Numer. Meth. Engng*, Volume 40, pp. 3247–3277, 1997a.
- Boroomand, B., Zienkiewicz, O., Recovery by equilibrium in patches(REP), *Int. J. Numer. Meth. Engng*, Volume 40, pp. 137–164, 1997b.
- Boroomand, B., Zienkiewicz, O., Recovery procedures in error estimation and adaptivity. Part II: Adaptivity in nonlinear problems of elasto-plasticity behaviour, *Comput. Methods Appl. Mech. Engrg.*, Volume 176, pp. 127–146, 1999.

- Borouchaki, H., Frey, P. J., Adaptive triangular-quadrilateral mesh generation, *Int. J. Numer. Meth. Engng*, Volume 41, pp. 915–934, 1998.
- Borouchaki, H., Laug, P., Cherouat, A., Saanouni, K., Adaptive remeshing in large plastic strain with damage, *Int. J. Numer. Meth. Engng*, Volume 63, pp. 1–36, 2005.
- Bottasso, C., Anisotropic mesh adaption by metric-driven optimization, *Int. J. Numer. Meth. Engng*, Volume 60, pp. 597–639, 2004.
- Bouchard, P., Bay, F., Chastel, Y., Numerical modelling of crack propagation: automatic remeshing and comparison of different criteria, *Comput. Methods Appl. Mech. Engrg.*, Volume 192, pp. 3887–3908, 2003.
- Bouchard, P., Bay, F., Chastel, Y., Tovenà, I., Crack propagation modelling using an advanced remeshing technique, *Comput. Methods Appl. Mech. Engrg.*, Volume 189, pp. 723–742, 2000.
- Bouiliard, P., Allard, J.-F., Warzee, G., Superconvergent patch recovery technique for the finite element method in acoustics, *Commun. Numer. Meth. Engng*, Volume 12, pp. 581–594, 1996.
- Boussetta, R., Coupez, T., Fourment, L., Adaptive remeshing based on a posteriori error estimation for forging simulation, *Comput. Methods Appl. Mech. Engrg.*, Volume 195, pp. 6626–6645, 2006.
- Brackbill, J., Saltzman, J., Adaptive zoning for singular problems in two dimensions, *Journal of Computational Physics*, Volume 46, pp. 342–368, 1982.
- Branets, L., Carey, G., Smoothing and adaptive redistribution for grids with irregular valence and hanging nodes, in *Proceedings of the 13th International Meshing Roundtable*, Virginia, USA, 2004.
- Bugeda, G., A comparison between new adaptive remeshing strategies based on point wise stress error estimation and energy norm error estimation, *Commun. Numer. Meth. Engng*, 469–482, 2002.
- Bugeda, G., Onate, E., A general methodology for structural shape optimization problems using automatic adaptive remeshing, *Int. J. Numer. Meth. Engng*, Volume 36, pp. 3161–3185, 1993.
- Bugeda, G., Rodenas, J., Onate, E., An integration of a low cost adaptive remeshing strategy in the solution of structural shape optimization problems using evolutionary methods, *Computers and Structures*, Volume in Press, 2007.
- Burke, J. V., Lewis, A. S., Overton, M. L., A Robust Gradient Sampling Algorithm for Nonsmooth, Nonconvex Optimization, *SIAM Journal on Optimization*, Volume 15, pp. 751–779, 2005.
- Calvo, N., Idelsohn, S., All-hexahedral mesh smoothing with a node-based measure of quality, *Int. J. Numer. Meth. Engng*, Volume 50, pp. 1957–1967, 2001.
- Canann, S. A., Stephenson, M. B., Blacker, T., Optismoothing: An optimization-driven approach to mesh smoothing, *Finite Elements in Analysis and Design*, Volume 13, pp. 185–190, 1993.

- Canann, S. A., Tristano, J. R., Staten, M. L., An approach to combined laplacian and optimization-based smoothing for triangular quadrilateral, and quad-dominant meshes, in Proceedings of the seventh International Meshing Roundtable, 479–494, Sandia National Labs, 1998.
- Carey, G., Sharma, M., Wang, K., A class of data structures for 2-D and 3-D adaptive mesh refinement, *Int. J. Numer. Meth. Engng*, Volume 26, pp. 2607–2622, 1988.
- Cecot, W., Adaptive FEM analysis of selected elastic-visco-plastic problems, *Comput. Methods Appl. Mech. Engrg.*, Volume 196, pp. 3859–3870, 2007a.
- Cecot, W., Adaptive FEM analysis of selected elastic-visco-plastic problems, *Comput. Methods Appl. Mech. Engrg.*, Volume 2007, pp. 3859–3870, 2007b.
- Chen, Z., Tristano, J. R., Kwok, W., Combined Laplacian and optimization-based smoothing for quadratic mixed surface meshes, in Proceedings of the twelfth International Meshing Roundtable, 201–213, Sandia National Laboratories, 2003.
- Cirak, F., Ramm, E., A posteriori error estimation and adaptivity for elastoplasticity using the reciprocal theorem, *Int. J. Numer. Meth. Engng*, Volume 47, pp. 379–393, 2000.
- Coorevits, P., Bellenger, E., Alternative mesh optimality criteria for h-adaptive finite element method, *Finite Elements in Analysis and Design*, Volume 40, pp. 1195–1215, 2004.
- Dey, S., Datta, D., Shirron, J., Shephard, M., p-Version FEM for structural acoustics with a posteriori error estimation, *Comput. Methods Appl. Mech. Engrg.*, Volume 195, pp. 1946–1957, 2006.
- Diaz, A. M., Nicieza, C. G., Vigil, A. A., Improvement of quadrilateral meshes for discretization of tunnels, *Computers and Geotechnics*, Volume 31, pp. 47–56, 2004.
- Diaz, A. M., Nicieza, C. G., Vigil, A. A., Hexahedral mesh smoothing using a direct method, *Computers and Geotechnics*, Volume 31, pp. 453–463, 2005.
- Diez, P., Arroyo, M., Huerta, A., Adaptivity based on error estimation for viscoplastic softening materials, *Mech. Cohes.-Frict. Mater.*, Volume 5, pp. 87–112, 2000.
- Diez, P., Egozcue, J. J., Huerta, A., A posteriori error estimation for standard finite element analysis, *Comput. Methods Appl. Mech. Engrg.*, Volume 163, pp. 141–157, 1998.
- Diez, P., Huerta, A., A unified approach to remeshing strategies for finite element h-adaptivity, *Comput. Methods Appl. Mech. Engrg.*, Volume 176, pp. 215–229, 1999.
- Diez, P., Rodenas, J. J., Zienkiewicz, O., Equilibrated patch recovery error estimates: simple and accurate upper bounds of the error, *Int. J. Numer. Meth. Engng*, Volume 69, pp. 2075–2098, 2007.
- Escobar, J., Montenegro, R., Montero, G., Rodriguez, E., Gonzalez-Yuste, J., Smoothing and local refinement techniques for improving tetrahedral mesh quality, *Computers and Structures*, Volume 83, pp. 2423–2430, 2005.
- Escobar, J., Montero, G., Montenegro, R., Rodriguez, E., An algebraic method for smoothing surface triangulations on a local parametric space, *Int. J. Numer. Meth. Engng*, Volume 66,

- pp. 740–760, 2006.
- Escobar, J., Rodriguez, E., Montenegro, R., Montero, G., Gonzalez-Yuste, J., Simultaneous untangling and smoothing of tetrahedral meshes, *Comput. Methods Appl. Mech. Engrg.*, Volume 192, pp. 2775–2787, 2003.
- Espinosa, H. D., Zavattieri, P. D., Emore, G. L., Adaptive FEM computation of geometric and material nonlinearities with application to brittle failure, *Mechanics of Materials*, Volume 29, pp. 275–305, 1998.
- Estep, D., Holst, M., Mikulencak, D., Accounting for stability: a posteriori error estimates based on residuals and variational analysis, *Commun. Numer. Meth. Engrg*, Volume 18, pp. 15–30, 2002.
- Fernandes, J., Martins, P., All-hexahedral remeshing for the finite element analysis of metal forming processes, *Finite Elements in Analysis and Design*, Volume 43, pp. 666–679, 2007.
- Field, D. A., Laplacian smoothing and delaunay triangulations, *Commun. Numer. Meth. Engrg*, Volume 4, pp. 709–712, 1988.
- Fischer, A., Bar-Yoseph, P., Adaptive mesh generation based on multi-resolution quadtree representation, *Int. J. Numer. Meth. Engrg*, Volume 48, pp. 1571–1582, 2000.
- Fish, J., Markolefas, S., Adaptive global-local refinement strategy based on the interior error estimates of the h-method, *Int. J. Numer. Meth. Engrg*, Volume 37, pp. 827–838, 1994.
- Freitag, L. A., An efficient parallel algorithm for mesh smoothing, in *Proceedings of the Fourth International Meshing Roundtable*, 47–58, Sandia National Laboratories, 1995.
- Freitag, L. A., On combining Laplacian and optimization-based smoothing techniques, *Trends in Unstructured Mesh Generation*, ASME, Volume 220, pp. 37–44, 1997.
- Freitag, L. A., Local optimization-based untangling algorithms for quadrilateral meshes, in *Proceedings of the Tenth International Meshing Roundtable*, 397–406, Sandia National Laboratories, 2001.
- Freitag, L. A., Knupp, P. M., Tetrahedral mesh improvement via optimization of the element condition number, *Int. J. Numer. Meth. Engrg*, Volume 53, pp. 1377–1391, 2002.
- Freitag, L. A., Plassmann, P., Local optimization-based simplicial mesh untangling and improvement, *Int. J. Numer. Meth. Engrg*, Volume 49, pp. 109–125, 2000.
- Frey, W. H., Selective refinement: a new strategy for automatic node placement in graded triangular meshes, *Int. J. Numer. Meth. Engrg*, Volume 24, pp. 2183–2200, 1987.
- Fuenmayor, F., Oliver, J., Criteria to achieve nearly optimal meshes in the h-adaptive finite element method, *Int. J. Numer. Meth. Engrg*, Volume 39, pp. 4039–4061, 1996.
- Fuenmayor, F., Oliver, J., Rodenas, J., Extension of the zienkiewicz-zhu error estimator to shape sensitivity analysis, *Int. J. Numer. Meth. Engrg*, Volume 40, pp. 1413–1433, 1997.
- Gallimard, L., Ladeveze, P., Pelle, J., Error estimation and adaptivity in elastoplasticity, *Int. J. Numer. Meth. Engrg*, Volume 39, pp. 189–217, 1996.

- Garimella, R. V., Shashkov, M. J., Knupp, P. M., Triangular and quadrilateral surface mesh quality optimization using local parametrization, *Comput. Methods Appl. Mech. Engrg.*, Volume 2004, pp. 913–928, 2004.
- Gautham, B., Goyal, S., Gandhe, A., Boundary controlled automatic remeshing for 2D simulation of metal forming, *Journal of Materials Processing Technology*, Volume 134, pp. 108–114, 2003.
- Giuliani, S., An algorithm for continuous rezoning of the hydrodynamic grid in arbitrary Lagrangian-Eulerian computer codes, *Nuclear Engineering and Design*, Volume 72, pp. 205–212, 1982.
- Graetsch, T., Bathe, K.-J., A posteriori error estimation techniques in practical finite element analysis, *Computers and Structures*, Volume 83, pp. 235–265, 2005.
- Greaves, D., Borthwick, A., Hierarchical tree-based finite element mesh generation, *Int. J. Numer. Meth. Engng*, Volume 45, pp. 447–471, 1999.
- Gu, H., Zong, Z., Hung, K., A modified superconvergent patch recovery method and its application to large deformation problems, *Finite Elements in Analysis and Design*, Volume 40, pp. 665–687, 2004.
- Hager, P., Wiberg, N., Adaptive eigenfrequency analysis by superconvergent patch recovery, *Comput. Methods Appl. Mech. Engrg.*, Volume 176, pp. 441–462, 1999.
- Hamide, M., Massoni, E., Bellet, M., Adaptive mesh technique for thermal-metallurgical numerical simulation of arc welding processes, *Int. J. Numer. Meth. Engng*, Volume 73, pp. 624–641, 2008.
- Herrmann, L. R., ASCE, M., Laplacian-Isoparametric grid generation scheme, *Journal of the Engineering Mechanics Division*, Volume 102, pp. 749–756, 1976.
- Hinton, E., Campbell, J., Local and global smoothing of discontinuous finite element functions using a least squares method, *Int. J. Numer. Meth. Engng*, Volume 8, pp. 461–480, 1974.
- Hortig, C., Svendsen, B., Adaptive mesh refinement in the context of shear banding and high speed cutting, in preparation, 2008.
- Huerta, A., Diez, P., Error estimation including pollution assessment for nonlinear finite element analysis, *Comput. Methods Appl. Mech. Engrg.*, Volume 181, pp. 21–41, 2000.
- Huerta, A., Rodriguez-Ferran, A., Diez, P., Error estimation and adaptivity for nonlinear FE analysis, *Int. J. Appl. Math. Comput. Sci.*, Volume 12, pp. 59–70, 2002.
- Huerta, A., Rodriguez-Ferran, A., Diez, P., Sarrate, J., Adaptive finite element strategies based on error assessment, *Int. J. Numer. Meth. Engng*, Volume 46, pp. 1803–1818, 1999.
- Hugger, J., A theory for local, a posteriori, pointwise, residual-based estimation of the finite element error, *Journal of Computation and Applied Mathematics*, Volume 135, pp. 241–292, 2001.
- Hyun, S., Lindgren, L.-E., Smoothing and adaptive remeshing schemes for graded element, *Commun. Numer. Meth. Engng*, Volume 17, pp. 1–17, 2001.

- Hyun, S., Lindgren, L.-E., Simulating a chain of manufacturing processes using a geometry-based finite element code with adaptive meshing, *Finite Elements in Analysis and Design*, Volume 40, pp. 511–528, 2004.
- Jones, R., A self-organizing mesh generation program, *Journal of Pressure Vessel Technology*, Volume 96, pp. 193–199, 1974.
- Joun, M., Lee, M., Quadrilateral finite-element generation and mesh quality control for metal forming simulation, *Int. J. Numer. Meth. Engng*, Volume 40, pp. 4059–4075, 1997.
- Jr., M. V., Owen, D., Aspects of ductile fracture and adaptive mesh refinement in damaged elasto-plastic materials, *Int. J. Numer. Meth. Engng*, Volume 50, pp. 29–54, 2001.
- Kalhari, V., Modelling and simulation of mechanical cutting, Ph.D. thesis, Lulea Tekniska University, 2001.
- Kanchi, H., Masud, A., A 3D adaptive mesh moving scheme, *Int. J. Numer. Meth. Fluids*, Volume 54, pp. 923–944, 2007.
- Khoei, A., Azadi, H., Moslemi, H., Modeling of crack propagation via an automatic adaptive mesh refinement based on modified superconvergent patch recovery technique, *Engineering Fracture Mechanics*, Volume 75, pp. 2921–2945, 2008.
- Khoei, A., Gharehbaghi, S., Tabarraie, A., Riahi, A., Error estimation, adaptivity and data transfer in enriched plasticity continua to analysis of shear band localization, *Applied Mathematical Modelling*, Volume 31, pp. 983–1000, 2007.
- Khoei, A., Lewis, R. W., H-adaptive finite element analysis for localization phenomena with reference to metal powder forming, *Finite Elements in Analysis and Design*, Volume 38, pp. 503–519, 2002.
- Khoei, A., Tabarraie, A., Gharehbaghi, S., H-adaptive mesh refinement for shear band localization in elasto-plasticity Cosserat continuum, *Communications in Nonlinear Science and Numerical Simulation*, Volume 10, pp. 253–286, 2005.
- Khoei, A. R., Lewis, R. W., Adaptive finite element remeshing in a large deformation analysis of metal powder forming, *Int. J. Numer. Meth. Engng*, Volume 45, pp. 801–820, 1999.
- Knupp, P. M., Achieving finite element mesh quality via optimization of the Jacobian matrix norm and associated quantities. Part I: a framework for surface mesh optimization, *Int. J. Numer. Meth. Engng*, Volume 48, pp. 401–420, 2000a.
- Knupp, P. M., Achieving finite element mesh quality via optimization of the Jacobian matrix norm and associated quantities. Part II: A framework for volume mesh optimization and the condition number of the Jacobian matrix, *Int. J. Numer. Meth. Engng*, Volume 48, pp. 1165–1185, 2000b.
- Knupp, P. M., A framework for variational grid generation: conditioning the Jacobian matrix with matrix norms, *SIAM J. SCI. COMPUT*, Volume 21, pp. 2029–2047, 2000c.
- Knupp, P. M., Hexahedral and tetrahedral mesh untangling, *Engineering with Computers*, Volume 17, pp. 261–268, 2001.

- Knupp, P. M., Algebraic mesh quality metrics for unstructured initial meshes, *Finite Elements in Analysis and Design*, Volume 39, pp. 217–241, 2003a.
- Knupp, P. M., A method for hexahedral mesh shape optimization, *Int. J. Numer. Meth. Engng*, Volume 58, pp. 319–332, 2003b.
- Krishnamoorthy, C. S., Raphael, B., Mukherjee, S., Meshing by successive superelement decomposition (MSD) - A new approach to quadrilateral mesh generation, *Finite Elements in Analysis and Design*, Volume 20, pp. 1–37, 1995.
- Kubli, W., Reissner, J., Optimization of sheet-metal forming processes using the special-purpose program AUTOFORM, *Journal of Materials Processing Technology*, Volume 50, pp. 292–305, 1995.
- Kvamsdal, T., Okstad, K. M., Error estimation based on superconvergent patch recovery using statically admissible stress fields, *Int. J. Numer. Meth. Engng*, Volume 42, pp. 443–472, 1998.
- Kwak, D.-Y., Cheon, J.-S., Im, Y.-T., Remeshing for metal forming simulations—Part I: Two-dimensional quadrilateral remeshing, *Int. J. Numer. Meth. Engng*, Volume 53, pp. 2463–2500, 2002.
- Kwak, D.-Y., Im, Y.-T., Remeshing for metal forming simulations—Part II: Three-dimensional hexahedral mesh generation, *Int. J. Numer. Meth. Engng*, Volume 53, pp. 2501–2528, 2002.
- Labbe, P., Garon, A., A robust implementation of Ziekiewicz and Zhu's local patch recovery method, *Commun. Numer. Meth. Engng*, Volume 11, pp. 427–434, 1995.
- Lakhany, A., Marek, I., Whiteman, J., Superconvergence results on mildly structured triangulations, *Comput. Methods Appl. Mech. Engrg.*, Volume 189, pp. 1–75, 2000.
- Lakhany, A., Whiteman, J., Superconvergent recovery based error estimators, *Mathematics and Computers in Simulation*, Volume 50, pp. 97–114, 1999.
- Lee, C., Lo, S., A new scheme for the generation of a graded quadrilateral mesh, *Computers and Structures*, Volume 52, pp. 847–857, 1994.
- Lee, M., Joun, M., Lee, J., Adaptive tetrahedral element generation and refinement to improve the quality of bulk metal forming simulation, *Finite Elements in Analysis and Design*, Volume 43, pp. 788–802, 2007.
- Lee, N.-S., Bathe, K.-J., Error indicators and adaptive remeshing in large deformation finite element analysis, *Finite Elements in Analysis and Design*, Volume 16, pp. 99–139, 1994.
- Lee, T., Park, H. C., Lee, S. W., A superconvergent stress recovery technique with equilibrium constraint, *Int. J. Numer. Meth. Engng*, Volume 40, pp. 1139–1160, 1997.
- Levine, N., Superconvergent recovery of the gradient from piecewise linear finite-element approximations, *IMA Journal of numerical analysis*, Volume 5, pp. 407–427, 1985.
- Lewis, R., Khoei, A., Numerical analysis of strain localization in metal powder-forming processes, *Int. J. Numer. Meth. Engng*, Volume 52, pp. 489–501, 2001.
- Li, B., Zhang, Z., Analysis of a class of superconvergence patch recovery techniques for linear

- and bilinear finite elements, *Numer Methods Partial Differential Eq*, Volume 15, pp. 151–167, 1999.
- Li, L.-y., Bettess, P., Notes on mesh optimal criteria in adaptive finite element computations, *Commun. Numer. Meth. Engng*, Volume 11, pp. 911–915, 1995.
- Li, L.-Y., Bettess, P., Error Estimation and adaptive remeshing techniques in elasto-plasticity, *Commun. Numer. Meth. Engng*, Volume 13, pp. 285–299, 1997.
- Li, L.-y., Bettess, P., Bull, J., Theoretical formulations for adaptive finite element computations, *Commun. Numer. Meth. Engng*, Volume 11, pp. 857–868, 1995.
- Li, L.-y., Bettess, P., Bull, J. W., Bond, T. J., Adaptive finite element analysis of stiffened shells, *Advances in Engineering Software*, Volume 28, pp. 501–507, 1997.
- Li, M., Moshfegh, R., Nilsson, L., Two-mesh refinement indicators and adaptivity in non-linear explicit finite element analysis of shell using LS-DYNA, *Commun. Numer. Meth. Engng*, Volume 16, pp. 785–800, 2000.
- Li, X., Wiberg, N.-E., A posteriori error estimate by element patch post-processing, adaptive analysis in energy and L2 norms, *Computers and Structures*, Volume 53, pp. 907–919, 1994.
- Liew, K., Rajendran, S., New superconvergent points of the 8-node serendipity plane element for patch recovery, *Int. J. Numer. Meth. Engng*, Volume 54, pp. 1103–1130, 2002.
- Lin, R., Zhang, Z., Natural superconvergent points of triangular finite elements, *Numer Methods Partial Differential Eq*, Volume 20, pp. 864–906, 2004.
- Lohner, R., Yang, C., Improved ALE mesh velocities for moving bodies, *Commun. Numer. Meth. Engng*, Volume 12, pp. 599–608, 1996.
- Mackinnon, R., Carey, G., Superconvergent derivatives: a Taylor series analysis, *Int. J. Numer. Meth. Engng*, Volume 28, pp. 489–509, 1989.
- Maisano, G., Micheletti, S., Perotto, S., Bottasso, C., On some new recovery-based a posteriori error estimators, *Comput. Methods Appl. Mech. Engrg.*, Volume 195, pp. 4794–4815, 2006.
- Mathisen, K. M., Hopperstad, O. S., Okstad, K. M., Berstad, T., Error estimation and adaptivity in explicit nonlinear finite element simulation of quasi-static problems, *Computers and Structures*, Volume 72, pp. 627–644, 1999.
- McDill, J., Goldak, J., Oddy, A., Bibby, M., Isoparametric quadrilaterals and hexahedrons for mesh-grading algorithms, *Commun. Numer. Meth. Engng*, Volume 3, pp. 155–163, 1987.
- Mediavilla, J., Peerlings, R., Geers, M., A robust and consistent remeshing-transfer operator for ductile fracture simulations, *Computers and Structures*, Volume 84, pp. 604–623, 2006.
- Miehe, C., Gurses, E., A robust algorithm for configurational-force-driven brittle crack propagation with R-adaptive mesh alignment, *Int. J. Numer. Meth. Engng*, Volume 72, pp. 127–155, 2007.
- Mukherjee, S., Krishnamoorthy, C. S., A pollution controlled hybrid interior error estimator for linear elastostatics, *Int. J. Numer. Meth. Engng*, Volume 43, pp. 507–532, 1998a.

- Mukherjee, S., Krishnamoorthy, C. S., A weighted element patch based superconvergent stress extraction strategy, *Commun. Numer. Meth. Engng*, Volume 14, pp. 731–749, 1998b.
- Murthy, K., Mukhopadhyay, M., Adaptive finite element analysis of mixed-mode crack problems with automatic mesh generator, *Int. J. Numer. Meth. Engng*, Volume 49, pp. 1087–1100, 2000.
- Naga, A., Zhang, Z., A posteriori error estimates based on the polynomial preserving recovery, *SIAM J. NUMER. ANAL.*, Volume 42, pp. 1780–1800, 2004.
- Nordlund, P., Giannakopoulos, A., Haeggblad, B., Adaptive mesh-updating methods for nonlinear finite element analysis of shells, *Int. J. Numer. Meth. Engng*, Volume 43, pp. 1523–1544, 1998.
- Oddy, A., Goldak, J., McDill, M., Bibby, M., A distortion metric for iso-parametric finite elements, *CSME*, Volume 12, pp. 213–217, 1988.
- Oden, J., Prudhomme, S., Hammerand, D. C., Kuczma, M. S., Modeling error and adaptivity in nonlinear continuum mechanics, *Comput. Methods Appl. Mech. Engrg.*, Volume 190, pp. 6663–6684, 2001.
- Oden, J., Strouboulis, T., Devloo, P., Adaptive finite element methods for the analysis of inviscid compressible flow: Part I. Fast refinement/unrefinement and moving mesh methods for unstructured meshes, *Comput. Methods Appl. Mech. Engrg.*, Volume 59, pp. 327–362, 1986.
- Oden, J. T., Brauchli, H., On the calculation of consistent stress distributions in finite element approximations, *Int. J. Numer. Meth. Engng*, Volume 3, pp. 317–325, 1971.
- Oden, J. T., Reddy, J., Note on an approximate method for computing consistent conjugate stresses in elastic finite elements, *Int. J. Numer. Meth. Engng*, Volume 6, pp. 55–61, 1973.
- Oh, H., Lim, J., Modified h-method with directional error estimate for finite element stress analysis, *Computers and Structures*, Volume 65, pp. 191–204, 1997.
- Oh, H.-S., Batra, R., Locations of optimal stress points in higher-order elements, *Commun. Numer. Meth. Engng*, Volume 15, pp. 127–136, 1999.
- Okstad, K. M., Kvamsdal, T., Mathisen, K. M., Superconvergent patch recovery for plate problems using statically admissible stress resultant fields, *Int. J. Numer. Meth. Engng*, Volume 44, pp. 697–727, 1999.
- Owen, D., Jr., M. V., Computational techniques applied to high-speed machining under adiabatic strain localization conditions, *Comput. Methods Appl. Mech. Engrg.*, Volume 171, pp. 445–461, 1999.
- Park, C.-H., Yang, D.-Y., Adaptive refinement of all-hexahedral elements for three-dimensional metal forming analysis, *Finite Elements in Analysis and Design*, Volume 43, pp. 22–35, 2006.
- Park, H. C., Shin, S.-H., Lee, S. W., A superconvergent stress recovery technique for accurate boundary stress extraction, *Int. J. Numer. Meth. Engng*, Volume 45, pp. 1227–1242, 1999.
- Patra, A., Gupta, A., A systematic strategy for simultaneous adaptive hp finite element mesh modification using nonlinear programming, 2001.

- PavanaChand, C., KrishnaKumar, R., Remeshing issues in the finite element analysis of metal forming problems, *Journal of Materials Processing Technology*, Volume 75, pp. 63–74, 1998.
- Pebay, P., Planar quadrlateral quality measures, *Engineering and Computers*, Volume 20, pp. 157–175, 2004.
- Pebay, P., Baker, T. J., Analysis of triangle quality measures, *MATHEMATICS OF COMPUTATION*, Volume 72, pp. 1817–1839, 2003.
- Peric, D., Hochard, C., Dutko, M., Owen, D., Transfer operators for evolving meshes in small strain elasto-plasticity, *Comput. Methods Appl. Mech. Engrg.*, Volume 137, pp. 331–344, 1996.
- Peric, D., Jr., M. V., Owen, D., On adaptive strategies for large deformations of elasto-plastic solids at finite strains: computational issues and industrial applications, *Comput. Methods Appl. Mech. Engrg.*, Volume 176, pp. 279–312, 1999.
- Peric, D., Yu, J., Owen, D., On error estimates and adaptivity in elastoplastic solids: application to the numerical simulation of strain localization in classical and Cosserat continua, *Int. J. Numer. Meth. Engng*, Volume 37, pp. 1351–1379, 1994.
- Petersen, S., Rodrigues, J., Martins, P., Automatic generation of quadrilateral meshes for the finite element analysis of metal forming processes, *Finite Elements in Analysis and Design*, Volume 35, pp. 157–168, 2000.
- Picasso, M., Numerical study of the effectivity index for an anisotropic error indicator based on Zienkiewicz-Zhu error estimator, *Commun. Numer. Meth. Engng*, Volume 19, pp. 13–23, 2003.
- Pires, F. A., Neto, E. d. S., Owen, D., On the finite element prediction of damage growth and fracture initiation in finitely deforming ductile materials, *Comput. Methods Appl. Mech. Engrg.*, Volume 193, pp. 5223–5256, 2004.
- Prasad, N. S., Hari, B. S., Ganti, S. P., An adaptive mesh generation scheme for finite element analysis, *Computers and Structures*, Volume 50, pp. 1–9, 1994.
- Prasad, N. S., Rajagopal, C., Effect of node placement algorithm on adaptive mesh generation, *Computers and Structures*, Volume 62, pp. 909–917, 1997.
- Prathap, G., Barlow points and gauss points and the aliasing and best fit paradigms, *Computers and Structures*, Volume 58, pp. 321–325, 1996.
- Rajendran, S., Liew, K., Optimal stress sampling points of plane triangular elements for patch recovery of nodal stresses, *Int. J. Numer. Meth. Engng*, Volume 58, pp. 579–607, 2003.
- Ravindranath, M., Kumar, R. K., Simulation of cold forging using contact and practical adaptive meshing algorithms, *Journal of Materials Processing Technology*, Volume 104, pp. 110–126, 2000.
- Riccus, J., Schweizerhof, K., Baumann, M., Combination of adaptivity and mesh smoothing for the finite element analysis of shells with intersections, *Int. J. Numer. Meth. Engng*, Volume 40, pp. 2459–2474, 1997.

- Rieger, A., Wriggers, P., Adaptive methods for thermomechanical coupled contact problems, *Int. J. Numer. Meth. Engng*, Volume 59, pp. 871–894, 2004.
- Robinson, J., Some new distortion measures for quadrilaterals, *Finite Elements in Analysis and Design*, Volume 3, pp. 183–197, 1987.
- Rodenas, J., Tur, M., Fuenmayor, F., Vercher, A., Improvement of the superconvergent patch recovery technique by the use of constraint equations: the SPR-C technique, *Int. J. Numer. Meth. Engng*, Volume 70, pp. 705–727, 2006.
- Rodriguez-Ferran, A., Huerta, A., Error estimation and adaptivity for nonlocal damage models, *International Journal of Solids and Structures*, Volume 37, pp. 7501–7528, 2000.
- Rodriguez-Ferran, A., Morata, I., Huerta, A., Efficient and reliable nonlocal damage models, *Comput. Methods Appl. Mech. Engrg.*, Volume 193, pp. 3431–3455, 2004.
- Sarrate, J., Huerta, A., Efficient unstructured quadrilateral mesh generation, *Int. J. Numer. Meth. Engng*, Volume 49, pp. 1327–1350, 2000.
- Sarrate, J., Hueta, A., An improved algorithm to smooth graded quadrilateral meshes preserving the prescribed element size, *Commun. Numer. Meth. Engng*, Volume 17, pp. 89–99, 2001.
- Secchi, S., Simoni, L., An improved procedure for 2D unstructured Delaunay mesh generation, *Advances in Engineering Software*, Volume 34, pp. 217–234, 2003.
- Secchi, S., Simoni, L., Schrefler, B. A., Mesh adaptation and transfer schemes for discrete fracture propagation in porous materials, *Int. J. Numer. Anal. Meth. Geomech.*, Volume 31, pp. 331–345, 2007.
- Selman, A., Hinton, E., Bicanic, N., Adaptive mesh refinement for localised phenomena, *Computers and Structures*, Volume 63, pp. 475–495, 1997.
- Sheng, Z., Jirathearanat, S., Altan, T., Adaptive FEM simulation for prediction of variable blank holder force in conical cup drawing, *International Journal of Machine Tools and Manufacture*, Volume 44, pp. 487–494, 2004.
- Solin, P., Cervený, J., Doležel, I., Arbitrary-level hanging nodes and automatic adaptivity in the hp-FEM, *Mathematics and Computers in Simulation*, Volume 77, pp. 117–132, 2008.
- Subbaraj, K., Dokainish, M., Side-node transition quadrilateral finite elements for mesh-grading, *Computers and Structures*, Volume 5, pp. 1175–1183, 1988.
- Tabarraei, A., Sukumar, N., Adaptive computations on conforming quadtree meshes, *Finite Elements in Analysis and Design*, Volume 41, pp. 686–702, 2005.
- Talbert, J. A., Development of an automatic two-dimensional finite element mesh generator using quadrilateral elements and bezier curve boundary definition, *Int. J. Numer. Meth. Engng*, Volume 29, pp. 1551–1567, 1990.
- Tan, Z., Huang, Y., An alternating Crank-Nicolson method for the numerical solution of the phase-field equations using adaptive moving meshes, *Int. J. Numer. Meth. Fluids*, Volume 56, pp. 1673–1693, 2008.

- Tang, X., Sato, T., Adaptive mesh refinement and error estimate for 3-D seismic analysis of liquefiable soil considering large deformation, *Journal of Natural Disaster Science*, Volume 26, pp. 37–48, 2004.
- Ubertini, F., Patch recovery based on complementary energy, *Int. J. Numer. Meth. Engng*, Volume 59, pp. 1501–1538, 2004.
- Vallet, M.-G., Manole, C.-M., Dompierre, J., Dufour, S., Guibault, F., Numerical comparison of some Hessian recovery techniques, *Int. J. Numer. Meth. Engng*, Volume 72, pp. 987–1007.
- Verfuerth, R., A review of a posteriori error estimation techniques for elasticity problems, *Comput. Methods Appl. Mech. Engrg.*, Volume 176, pp. 419–440, 1999.
- Wiberg, N.-E., Superconvergent Patch Recovery - a key to quality assessed FE solutions, *Advances in Engineering Software*, Volume 28, pp. 85–95, 1997.
- Wiberg, N.-E., Abdulwahab, F., Patch recovery based on superconvergent derivatives and equilibrium, *Int. J. Numer. Meth. Engng*, Volume 36, pp. 2703–2724, 1993.
- Wiberg, N.-E., Abdulwahab, F., Error estimation with postprocessed finite element solutions, *Computers and Structures*, Volume 64, pp. 113–137, 1997.
- Wiberg, N.-E., Abdulwahab, F., Ziukas, A., Enhanced superconvergent patch recovery incorporating equilibrium and boundary conditions, *Int. J. Numer. Meth. Engng*, Volume 37, pp. 3417–3440, 1994.
- Wiberg, N.-E., Abdulwahab, F., Ziukas, S., Improved element stresses for node and element patches using superconvergent patch recovery, *Commun. Numer. Meth. Engng*, Volume 11, pp. 619–627, 1995.
- Wiberg, N.-E., Li, X., Adaptive finite element procedures for linear and non-linear dynamics, *Int. J. Numer. Meth. Engng*, Volume 46, pp. 1781–1802, 1999.
- Wiberg, N.-E., Li, X. D., Superconvergent patch recovery of finite-element solution and a posteriori L2 norm error estimate, *Commun. Numer. Meth. Engng*, Volume 10, pp. 313–320, 1994.
- Xie, L., Estimation of two-dimension tool wear based on finite element method, Ph.D. thesis, Karlsruhe University, 2004.
- Xing, H., Wang, S., Makinouchi, A., An adaptive mesh h-refinement algorithm for the finite-element modeling of sheet forming, *Journal of Materials Processing Technology*, Volume 91, pp. 183–190, 1999.
- Xu, H., Newman, T. S., An angle-base optimization approach for 2D finite element mesh smoothing, *Finite Elements in Analysis and Design*, Volume 42, pp. 1150–1164, 2006.
- Yazdani, A., Gakwaya, A., Dhatt, G., A posteriori error estimation based on the second derivative of the displacement field for two-dimensional elastic problems, *Computers and Structures*, Volume 62, pp. 317–338, 1997.
- Yazdani, A., Gakwaya, A., Dhatt, G., An improved superconvergent patch recovery technique for the axisymmetrical problems, *Computers and Structures*, Volume 66, pp. 799–821, 1998.

- Yerry, M. A., Shephard, M. S., A modified quadtree approach to finite element mesh generation, *IEEE Computer Graphics and Applications*, Volume 3, pp. 39–46, 1983.
- Yue, Z., Jr, D. R., Adaptive superposition of finite element meshes in elastodynamic problems, *Int. J. Numer. Meth. Engng*, Volume 63, pp. 1604–1635, 2005.
- Yue, Z., Jr, D. R., Rank deficiency in superconvergent patch recovery techniques with 4-node quadrilateral elements, *Commun. Numer. Meth. Engng*, Volume 23, pp. 1–10, 2006.
- Zhang, Z., Harold Dean Victory, J., Mathematical analysis of Zienkiewicz-Zhu's derivative patch recovery technique, *Numer Methods Partial Differential Eq*, Volume 12, pp. 507–524, 1996.
- Zhang, Z., Naga, A., Validation of the a posteriori error estimator based on polynomial preserving recovery for linear elements, *Int. J. Numer. Meth. Engng*, Volume 61, pp. 1860–1893, 2004.
- Zhang, Z., Naga, A., A new finite element gradient recovery method: superconvergence property, *SIAM J. Sci. Comput.*, Volume 26, pp. 1192–1213, 2005.
- Zhang, Z., Zhu, J., Analysis of the superconvergent patch recovery technique and a posteriori error estimator in the finite element method (II), *Comput. Methods Appl. Mech. Engrg.*, Volume 163, pp. 159–170, 1998.
- Zhang, Z., Zhu, J. Z., Analysis of the superconvergent patch recovery technique and a posteriori error estimator in the finite element method (I), *Comput. Methods Appl. Mech. Engrg.*, Volume 123, pp. 173–187, 1995.
- Zhao, C., Hobbs, B. E., Mhlhaus, H. B., Ord, A., A consistent point-searching algorithm for solution interpolation in unstructured meshes consisting of 4-node bilinear quadrilateral elements, *Int. J. Numer. Meth. Engng*, Volume 45, pp. 1509–1526, 1999.
- Zhu, J., Zienkiewicz, O., A posteriori error estimation and three-dimensional automatic mesh generation, *Finite Elements in Analysis and Design*, Volume 25, pp. 167–184, 1997.
- Zhu, J. Z., Zienkiewicz, O., Hinton, E., Wu, J., A new approach to the development of automatic quadrilateral mesh generation, *Int. J. Numer. Meth. Engng*, Volume 32, pp. 849–866, 1991.
- Zienkiewicz, O., Boroomand, B., Zhu, J., Recovery procedures in error estimation and adaptivity Part I: Adaptivity in linear problems, *Comput. Methods Appl. Mech. Engrg.*, Volume 176, pp. 111–125, 1999.
- Zienkiewicz, O., Liu, Y., Huang, G., Error estimation and adaptivity in flow formulation for forming problems, *Int. J. Numer. Meth. Engng*, Volume 25, pp. 23–42, 1988.
- Zienkiewicz, O., Taylor, R., The finite element patch test revisited A computer test for convergence, validation and error estimates, *Comput. Methods Appl. Mech. Engrg.*, Volume 149, pp. 223–254, 1997.
- Zienkiewicz, O., Zhu, J., A simple error estimator and adaptive procedure for practical engineering analysis, *Int. J. Numer. Meth. Engng*, Volume 24, pp. 337–357, 1987.
- Zienkiewicz, O., Zhu, J., The superconvergence patch recovery and a posteriori error estimates.

- Part 2: Error estimates and adaptivity, *Int. J. Numer. Meth. Engng*, Volume 33, pp. 1365–1382, 1992a.
- Zienkiewicz, O., Zhu, J., The superconvergent patch recovery and a posteriori error estimates. Part 1: The recovery technique, *Int. J. Numer. Meth. Engng*, Volume 33, pp. 1331–1364, 1992b.
- Zienkiewicz, O., Zhu, J., The superconvergent patch recovery (SPR) and adaptive finite element refinement, *Comput. Methods Appl. Mech. Engrg.*, Volume 1992, pp. 207–224, 1992c.
- Zienkiewicz, O., Zhu, J., Superconvergence and the superconvergent patch recovery, *Finite Elements in Analysis and Design*, Volume 19, pp. 11–23, 1995.
- Zienkiewicz, O., Zhu, J., Wu, J., Superconvergent patch recovery techniques - some further tests, *Commun. Numer. Meth. Engng*, Volume 9, pp. 251–258, 1993.

Acknowledgements

The research work presented in this dissertation was started at the Chair of Mechanics, Dortmund University of Technology in October 2004. I would like to thank all those who have helped me along the road to the completion of this dissertation.

Firstly, I would like to express my deepest gratitude to my supervisor Professor Bob Svendsen. Without his constant support and academic guidance throughout the course of this research, this dissertation could not have been completed. I also wish to thank our senior engineer Mr. Christian Hortig. Christian has been working together with me on this project and made invaluable assistance to enhance this dissertation.

I thank Dr. Clemens Barthel for friendly chats and his assistance in my German learning. I wish to thank Mr. Farhad Parvizia for many helpful discussions on my work. Thanks to my officemates Miss Yuliana Stepanova and Mr. Svyatoslav Gladkov for their support and friendship. I would also like to thank Mr. Tobias Kayser and Mr. Jan Truckenbrodt for their maintenance of the hardware and software. Thanks to Miss Daria Walencyk and Miss Christine Vu for their careful language correction of this dissertation. I especially thank Mrs. Kerstin Walter for her kind help throughout my work.

Especially, I would like to thank Professor Klaus Thermann, Professor Andreas Menzel and Professor Heribert Blum for serving on my dissertation committee. I appreciate Mr. Vadim Palnau, Mr. Weiya Xiang and all my colleagues' merits for providing a very pleasant working environment. I am also grateful to my former colleagues Dr. Jian Wang, Dr. Jaan Unger, Dr. Vladislav Levkovitch and Dr. Frederik Reusch for their encouragement and support.

Finally, I wish to express my special gratitude to my wife Ping Xu and my parents, for their love, support and dedication.

Dortmund, November 2008 *Xin Gu*

Curriculum Vitae

Personal

Name: Gu, Xin
Date of Birth: September 26, 1979
Place of Birth: Jiangsu, China
Nationality: Chinese

Education

1986-1997 Primary and middle schools, Jiangsu, China
1997-2001 B.Sc. study, Department of Engineering Mechanics and Technology, Tongji University, Shanghai, China
2001-2004 M.Sc. study, Department of Engineering Mechanics and Technology, Tongji University, Shanghai, China
2004-2008 Graduate Student, Chair of Mechanics, Department of Mechanical Engineering, Dortmund University of Technology, Germany